EUROPEAN MECHANICAL SCIENCE

2022
VOLUME: 6
ISSUE: 4

E-ISSN: 2587-1110

EDITOR IN CHIEF
PROF. DR. MUSTAFA ÖZCANLI

Editor in Chief

Editors

Layout Editor

Secretary

Indexed / Abstracted in:

TR-Dizin, CrossRef, Index Copernicus, Journal Factor, Rootindexing, ResearchBip, JournalFactor, JIFACTOR, Google Scholar, I2OR, Cosmos Impact Factor, International Innovative Journal Impact Factor (IIJIF), Scientific Indexing Services, InfoBase Index, Scientific Journal Impact Factor

Aims and Scopes

European Mechanical Science (EMS) is an international, peer reviewed journal which publishes full length original research papers, reviews related to all areas of Mechanical Engineering such as: Solid Mechanics, Materials Engineering, Automotive Engineering, Fluid Mechanics, Thermal Engineering, Engine and Power Engineering, Dynamics & Control, Robotics & Mechatronics, Transportation Engineering, Computational Mechanics, Design, Systems, Manufacturing, Bio-Medical Engineering; Process Engineering, Aerospace Engineering. No charges are required from the Authors to publish the articles.EMS is a quarterly published journal operating an online submission and peer review system. It allows authors to submit articles online and track their progress via its web interface.

https://dergipark.org.tr/ems

Contents

– *Research Articles*

EUROPEAN MECHANICAL SCIENCE
e-ISSN: 2587-1110

An autonomous hydrogen production system design based on the solid chemical hydride

Feride Cansu İskenderoğlu[1], Mustafa Kaan Baltacıoğlu[2*], Çağlar Conker[2], Hasan Hüseyin Bilgiç[2]

[1]İskenderun Technical University, Faculty of Engineering and Natural Science, Mechanical Engineering Department, Hatay, 31200, Turkey
[2]İskenderun Technical University, Faculty of Engineering and Natural Science, Mechatronics Engineering Department, Hatay, 31200, Turkey

Orcid: F.C. İskenderoğlu (0000-0003-4083-677X), M.K. Baltacıoğlu (0000-0002-4082-902X), Ç. Conker (0000-0002-1923-9092), H.H. Bilgiç (0000-0001-6006-8056)

Abstract: This paper develops a hydrogen generator prototype that is for fuel cell systems used in portable applications. This generator is designed based on the use of solid-state hydrides with high hydrogen storage capacity in the catalytic hydrolysis reaction. Some using problems such as unstable hydrogen production, one-off service life, heavy or large-volume storage system, and short duty time can be avoided in moveable applications when the use of the produced prototype. In addition, A simulation model and an autonomous control algorithm, which evaluates the hydrogen generation and temperature responses of the prototype, are developed. The results confirm that the performance of a portable and autonomous prototype with 4 parts and 1-hour hydrogen production capacity is enough for small fuel cell applications. As a result; the tightness and performance tests of the prototype were investigated using different catalyst samples for 1 hour, and the results were investigated in depth. The average flow rate of this 4-part autonomous generator is approximately 3.00 L/min.gcatalyst during 1 h. In the working cycle, the soft ripples have spied on the hydrogen-produced amount from time to time.

Keywords: Sodium Borohydride, Hydrogen Production, Autonomous System, Power Generator, Portable Application.

1. Introduction

Conventional fossil fuel sources, such as coal, oil, and natural gas, which meet most of the world's energy demand, are being consumed rapidly. Additionally, their combustion products are causing global problems, such as the greenhouse effect and pollution. Therefore, many countries have published their strategic plans to achieve net zero-emissions targets by 2050. Thus, there is a movement towards renewable energy sources, which are environmentally friendly, more efficient power production, zero emissions, over the world. Renewable energy technologies such as solar, wind, hydropower, and heat pumps are widely preferred for increasing energy demand [1]Co, Bi, CoBi, and CoBi/CNT catalysts are prepared via co-precipitation method and sodium borohydride (NaBH4. Today, battery technologies have been more popular to be used in applications that have a large share of carbon emissions such as portable applications and transportation applications. However, the batteries fail to satisfy the energy required for developing technologies, their weights increase the energy consumption of the systems and create transport problems. One of the developed systems, which is based on renewable energy sources, to supply the required energy is the fuel cells. The fuel cells have the potential of achieving much higher specific energy densities than any advanced battery system. Fuel cells, which can operate in light, quiet and grid-independent environments, have high energy conversion efficiency, high power density, and zero pollutant emission, providing an alternative way to obtain the energy required by portable applications [2]. At this point, alternative energy sources appear as a solution. Hydrogen is an excellent alternative to meet the growing demand for efficient and clean energy sources [3]. As an energy carrier, hydrogen is expected to play an important role in future energy systems. As the lightest element, hydrogen has many advantages such as environmental friendliness and the highest energy capacity per unit weight [4]in industry, working, cleaning, transportation and commuting from one place to another. The majority of energy being used is obtained from fossil fuels, which are not renewable resources and require a longer time to recharge or return to its original capacity. Energy from fossil fuels is cheaper but it faces some challenges compared to renewable energy resources. Thus, one of the most potential candidates to fulfill the energy requirements are renewable resources and the

---

[*] Corresponding author.
Email: mkaan.baltacioglu@iste.edu.tr

European Mechanical Science (2022), 6(4): 213-220
https://doi.org/10.26701/ems.1056942
Received: January 12, 2022 — Accepted: March 04, 2022

most environmentally friendly fuel is hydrogen (H2.

Besides, hydrogen is a very difficult gas to store. The most common method of hydrogen storage is to obtain compression and storage of hydrogen gas in high-quality tanks (at least 200 bar), but this method increases costs and causes high energy consumption. In addition to cost, hydrogen is a volatile and flammable gas, which creates disadvantages in terms of safety [5]. Nowadays, research is being done to use hydrogen stored in different chemical compounds to reduce these disadvantages. For example, various hydrides such as Lithium Hydride (LiH), Calcium Hydride (CaH_2), Magnesium Hydride (MgH_2), Lithium Borohydride ($LiBH_4$), Lithium Aluminum Hydride ($LiAlH_4$), Sodium Borohydride ($NaBH_4$), Ammonia Borane (NH_3BH_3) are used sources of hydrogen [6]. Among the borohydrides defined as reducing substances and used in the formation of many hydrolysis reactions, $NaHB_4$ is the most known. $NaHB_4$ is a strong reductant and can react with many organic and inorganic compounds. $NaBH_4$ is considered a potential candidate for hydrogen storage due to its high hydrogen storage density and controllable hydrogen release through hydrolysis at room temperature. As a result of the reaction of $NaBH_4$ with water, hydrogen is released and $NaBH_4$ can be synthesized again from Sodium Metaborate ($NaBO_2$), which is a by-product. In this case, it reveals that $NaBH_4$ is a renewable product. The reaction of $NaBH_4$ with water (Eqn.1) progresses very slowly under room conditions. A catalyst needs to be used to accelerate this reaction and increase the yield [7]. In hydrolysis reactions, when $NaBH_4$ is used in high concentrations, it can cause the by-product ($NaBO_2$) to crystallize and change the structure of the catalyst that used in the reaction [8]. In the hydrolysis reactions of $NaBH_4$, conventional catalysts containing noble metals such as Ru and Pt [9,10]simple, convenient, and safe chemical process generates high purity hydrogen gas on demand from stable, aqueous solutions of sodium borohydride, NaBH4, and ruthenium-based (Ru are replaced by Co or Co-B [11] supported, lower-cost catalysts.

$$NaBH_4 + 2H_2O \rightarrow NaBO_2 + 4H_2 \tag{1}$$

The average hydrogen flow rate required for a 500 W PEMFC is about 5 standard liters per minute (SLPM) [12]. However, 1.2 kW output can be obtained from the system with the highest hydrogen production rate of 16 SLPM that using at 3 kW PEMFC [13]. Therefore, the increase in the amount of NaBH4 concentration causes an increase in the hydrogen flow rate. In the results of the experiments conducted in the literature, an increase in the hydrogen production rate was observed as the concentration increased. The maximum hydrogen flow rate was measured as 120/16/2.4 SLPM in reactions using 15/10/5 wt% solutions, respectively [8].

In the literature, there are studies on PEMFC supported by NaBH4. Of those; Murooka et al. proposed a nickel-catalyzed solution as a catalyst for a 100 W PEMFC fed with NaBH4 [14]. At the Toyota Research Lab, Kojima et al. developed a NaBH4 assisted hydrogen production system with a hydrogen production rate of 120 SLPM to produce the hydrogen required for a 10 kW PEMFC [15].

In a hydrogen production system study by Kim et al., the system produced hydrogen at a rate of 6.5 SLPM for 120 minutes [16]. They have integrated this hydrogen generation system with a 400 W PEMFC. Sprayed Co-B catalyst was preferred as a catalyst in the system. In the microreactor study pioneered by Kim and Lee, a micro-reactor with an average hydrogen production rate of 5.6 ml/min was developed for Micro-PEMFC applications using Co-B catalyst [17]. Kim used Co-P-B catalyst, which has a higher efficiency than Co-B, as a catalyst in his last micro-reactor study [18]. He integrated the micro-reactor system he developed into a micro fuel cell with a maximum power output of 157 mW at a current of 0.5 A.

Li and Wang, developed a hydrogen generation system that hydrolyses NaBH4 with a conversion rate of over 90%, which can continuously supply hydrogen to power a 3 kW PEMFC. NaBH4 concentration of 15% by weight was used in the system. In addition, the system is controlled by a microcontroller [19].

In this study by Kim, solid-state NaBH4 particles were used. NaHCO3 solution with a concentration of 8.8% by weight at 25 °C was used as a catalytic solution. As a result of the study, a 100 W fuel cell system can be operated with the hydrogen produced from the developed system [20].

Avrahami et all, developed a hydrogen generation system powered by solid-state NaBH4 with a hydrogen density of 4.5% by weight and a hydrogen flow of about 400 mL/min, and an energy density of 1400 Wh/kg for long and short-run times [21]. In the hydrogen generator system experiments conducted by Zakhvatkin et al., they recorded that 110 L of hydrogen was produced for 6.3 hours with an average flow rate of 290 mL/min and fuel conversion efficiency of 98%. The energy density obtained from the system components is 1300 Wh/kg for the fuel, 540 Wh/kg for the generator, and 377 Wh/kg for the fuel cell with a power capacity of 30 W, respectively [22].

In this study, a new design of the hydrogen generator prototype, which has been developed for fuel cell systems used in portable applications, is focused on. The base of this prototype is designed as an autonomous hydrogen generator, that is using solid chemical hydrides for hydrogen/fuel cells applications. This design provides high energy density, inexpensive design, low cost, high applicability, and fast use, refilling, or cleaning. As a result of the study, a small prototype design was built, examined, and characterized, details about the operating system and performance of a portable and autonomous prototype with 4 parts and 1-hour hydrogen production capacity are given.

2. Materials and Experimental Methods

2.1. Materials

The Cobalt (Co) Micron powder was supplied from the Nanografi company. The Cobalt (Co) Micron Powder is 99.99% pure and has a size of 1 µm. $NaBH_4$ chemical powder was supplied from the Tekkim company. $NaBH_4$ is 98.5% pure and contains 0.05% Si and 0.005% Fe.

2.2. Experimental Setup/ Test Rig

Firstly, the catalytic activity performances of the Co Nanopowder were investigated on a reaction model which includes the hydrogen gas generation from the catalytic hydrolysis is being carried out in a 250 mL four-necked round-bottom reaction vessel. The precisely weighed solid $NaBH_4$ and the catalyst samples are loaded from one of the four necks. The water is being contacted with the solid powder in the reaction vessel using a dropping funnel. Then, the working performance of the hydrogen generator is tried with Co Nanopowders. The water + catalyst mixture was be added with the help of a pump to on the $NaBH_4$ particles that are in the fuel reservoir. The reaction is expected to occur rapidly at room temperature. The reaction temperature is measured with a thermocouple integrated from the second neck and connected with the microprocessor in both experiments. The hydrogen gas is passed through a dehumidifier to remove water vapor. The produced hydrogen gas volume was measured and recorded by a high-precision Alicat Flowmeter. Simultaneously measured data was transferred to the microprocessor and recorded in the host computer. The hydrogen gas produced as a result of the hydrolysis reaction taking place in the reactor was transferred through the humidifier to the flow meter. The pressure, temperature, and production amounts are taken from the flow meter collected by the microcontroller were being monitored and were be realized with an automatic control system for sustainable electricity generation.

The developed reactor is intended to be made of plexiglass material. All connections of the generator were pasted with chloroform adhesive to prevent possible hydrogen leakage, providing a high sealing environment. The fuels will be discharged from their respective chambers into the reservoir where the reaction takes place. The 20 ml water + catalyst mixture will be added with the help of a pump to on the $NaBH_4$ particles that are in the fuel reservoir. The reaction is expected to occur rapidly at room temperature. The hydrogen gas produced as a result of the hydrolysis reaction taking place in the reactor was transferred through the humidifier to the flow meter. The pressure, temperature, and production amounts are taken from the flow meter collected by the microcontroller will be monitored and will be realized with an automatic control system for sustainable electricity generation. The test rig of the hydrogen generator system is shown in Figure 1. The algorithm of the autonomous control system will be designed depending on the changes in reactor pressure. A test station will be installed in this way; the system tests such as pressure, temperature, and the performance of hydrogen production are planned in this system. The electronic operating performance of systems and autonomous systems requirements of the system will also be evaluated. After optimal results were obtained from these experimental tests, a prototype of the size that will be integrated into a stack of the fuel cell was prepared.

3. Prototype Design

In this study, a four-chamber generator was designed. The design of each of the rooms; consists of 4 sections, namely the control unit, the water reservoir, the auxiliary equipment section, and the $NaBH_4$ reservoir. The control unit is positioned above these 4 reaction chambers. The water reservoir consists of a chamber with a conical structure as a mixture of catalyst powder and water. It is aimed to provide the necessary water pressure for the water pump due to the shrinking structure of gravity and the conical structure. The water pump, sensors, and other auxiliary equipment are kept away from water and moisture contact in the auxiliary equipment section. Water and catalyst solu-

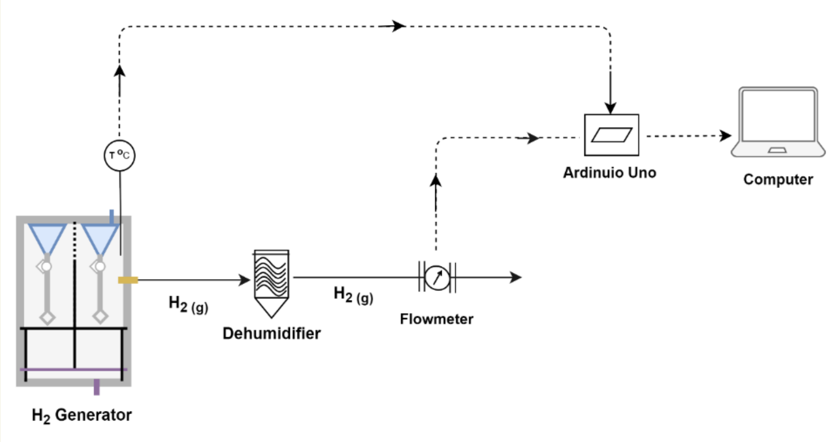

Figure 1. The test rig of the hydrogen generator system

tion, which is the flow of it controlled by a water pump, will be sprayed on the $NaBH_4$ powder with the help of nozzles, and a homogeneous distribution is achieved. The fuels are discharged from their respective chambers into the reservoir where the reaction takes place. The hydrogen generator prototype 3D design is shown in Figure 2. The hydrogen generator, whose size and volume, was determined, was manufactured using plexiglass material. All connections of the generator were pasted with chloroform adhesive to prevent possible hydrogen leakage, providing a high sealing environment.

Autonomous Control Card Design and Writing Control System Algorithms:

The basis of this project is to ensure the continuity of the energy source required for the duty period of the system, depending on the decrease in the gas level in the system. The gas sensor placed in the prototype of the gas sensor measures the hydrogen gas level, activates the water pump when the gas level starts to decrease depending on the situation and enables the reaction in the second reaction vessel to start. The autonomous control system flowchart and equipment connection of the hydrogen generator prototype is shown in Figure 3.

A temperature and humidity sensor has been added to the prototype to take into account other environmental conditions that may affect the operating performance of the system. With this sensor, it works independently of the system's autonomous control, but they are programmed to shut down the system when high values are measured. A reference value has been entered for the operation of the system. When the value measured by the gas sensor falls below this reference value, the next water pump will be activated and the reaction will be activated. According to the data coming from the gas sensor, a system mechanism that works automatically by triggering the 220 V water pump with DC 5V has been established.

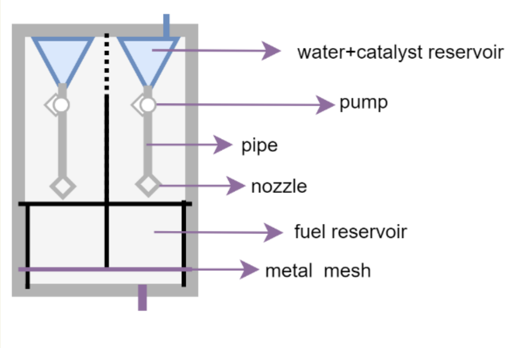

Figure 2. The design of the hydrogen generator system

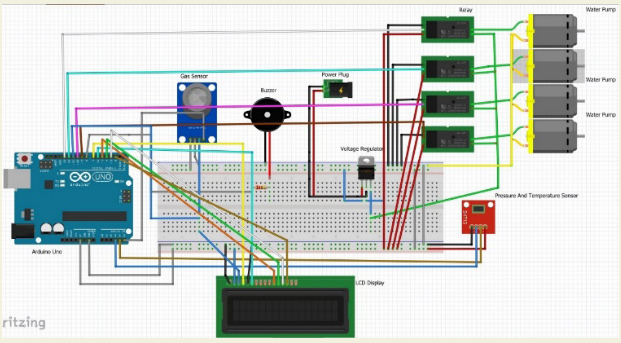

Figure 3. The design of the autonomous control system

The sensors are connected to the analog input of the Arduino. When the gas level drops according to the values between 0 and 255 read from our sensors, it activates the relay and controls the water flow. Since the water pump works with 12 volts (it can work a minimum of 6 volts), it is controlled with the help of a relay. The purpose of the relay is to prevent the Arduino used in the system from being burned due to the current. Since this process has a unidirectional working principle, a transistor can also be preferred. Values and important information read from the sensors can be read from the LCD screen.

Control System Algorithms:

The working algorithm written for the simultaneous monitoring of the autonomous operation and working parameters of the hydrogen generator is implemented using the Arduino board. The system is programmed using the 1.6.3 version of the Arduino software and the ATmega328 programming language. Figure 4 shows part of the Arduino software that contains the program's instructions.

For the required energy needed during the first operation, since the Arduino should be fed with at least 6 volts and the valves should be working at around a minimum of 6 volts, Lithium-Polymer batteries with a capacity of 7.4 V and 2-cell were preferred.

4. Results

Firstly, manual experiments have been carried out to record hydrogen production and reaction conditions such as hydrogen flow, generator' temperature, generator' pressure, and to evaluate the prototype's feasibility, sealing, efficiency and performance. The sealing and the performing experiments were made using Co nanopowder. After then, the Co-BFSs catalyst samples [23], that are synthesized in our previous study, were used in autonomous experiments of this prototype.

4.1. Manual performance experiments

The manual experiments of the prototype were carried out using 2 g of $NaBH_4$, 20 ml of distilled water, and, Co nanopowder as a catalyst that was used in 2 different amounts as 0.2 g and 0.5 g. A series of experiments were carried out until the sealing of the prototype was optimized. That is, the sealing of the prototype was increased until the amount of hydrogen gas produced by the Co nanopowder in the glass reactor vessel and the amount of hydrogen gas produced in the prototype were approximately the same.

In the experiments with 0.2 g and 0.5 g of Co nanopowder, the total hydrogen productions that are given in Figure 5, are approximately 340 L and 360 L, respectively. The total hydrogen amounts of the 0.2 g and 0.5 g Co powders are very close to each other, but the reaction using 0.5g of Co powder ends 2 times faster, can be shown. As can be seen in Figure 6, the reaction time shortened with the increase in the amount of catalyst, however, the hydrogen production rate decreased. Also, the hydrogen production average flow rates are approximately 80.95 and 55.38 L/min.$g_{catalyst}$, respectively. The hydrogen production rate of the hydrolysis reaction at 25 °C using 1 wt % $NaBH_4$ and Co powder is 0.13 L/min.$g_{catlayst}$ [24]. In this study, it is 500 times higher using 10 wt% $NaBH_4$ at 50 °C. Figure 6 is showing relatively constant hydrogen flow (of about 17.5 L/min) along 20 min. As a result, when the amount of Co catalyst sample was increased, the reaction times were shortened, but the high amount of hydrogen production observed in the use of different amounts of catalyst in the literature did not decrease. In the literature studies, it is stated that the reason is due to the maximum saturation of the reaction [23,25]. The reduction in this study is negligible. Manual experiments of the 4-segment prototype were performed in both catalyst amounts. As can be seen in Figure 7 and Figure 8, the next system segment was activated when the hydrogen flow rate for 0.5 g was about 3 L/min.$g_{catalyst}$, while in the experiment using 0.2 g catalyst, it was manually activated when the hydrogen flow rate was about 2.40 L/min.$g_{catalyst}$. In the hydrolysis reactions of the Co nanopowder end, it is difficult to produce stable hydrogen because the Co nanopowder hydrolysis reaction ends suddenly. Therefore, using Co nanopowder was not efficient in manual 4-segment experiments. Depending

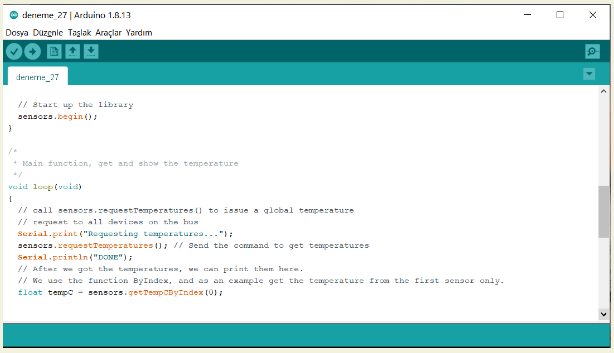

```
  // Start up the library
  sensors.begin();
}

/*
 * Main function, get and show the temperature
 */
void loop(void)
{
  // call sensors.requestTemperatures() to issue a global temperature
  // request to all devices on the bus
  Serial.print("Requesting temperatures...");
  sensors.requestTemperatures(); // Send the command to get temperatures
  Serial.println("DONE");
  // After we got the temperatures, we can print them here.
  // We use the function ByIndex, and as an example get the temperature from the first sensor only.
  float tempC = sensors.getTempCByIndex(0);
```

Figure 4. A part of the autonomous control system working algorithm

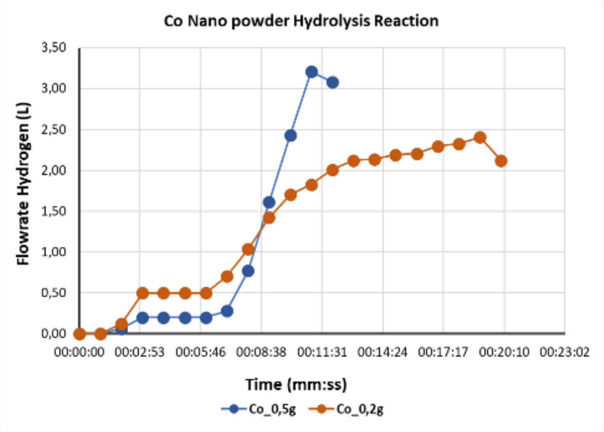

Figure 6. The flowrate hydrogen production of the Co nanopowder catalyst sample that is different amounts

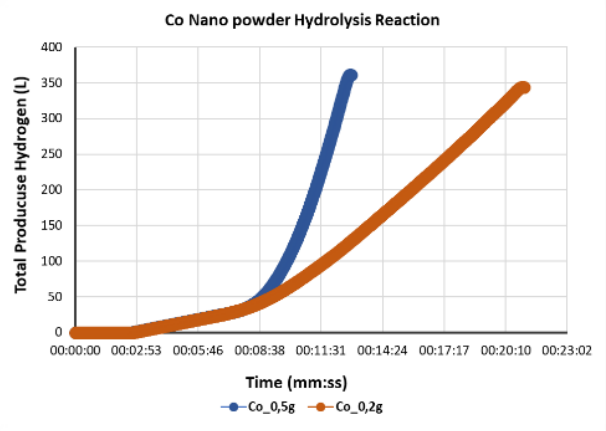

Figure 5. The total hydrogen production of the Co nanopowder catalyst sample that is different amounts

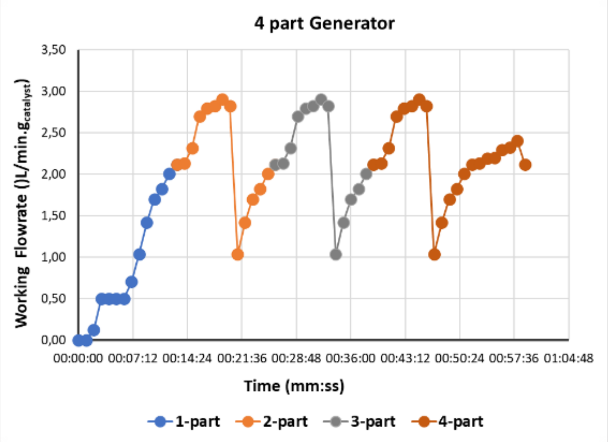

Figure 7. The performance of Manuel Hydrogen Generator Prototype with 0.2 g Co nanopowder catalyst for 1-hour

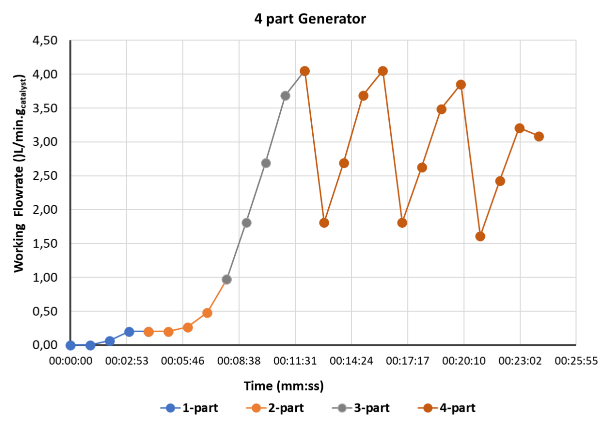

Figure 8. The performance of Manuel Hydrogen Generator Prototype with 0.5 g Co nanopowder catalyst for 24-min

on the decrease in hydrogen gas in the system, it may be considered to change the algorithm to be used for activating the next segment for some special cases. This working cycle is designed to have a maximum instantaneous hydrogen production of 3 L / min.gcatalyst continuously for 1 hour. In this working cycle, the amount of hydrogen produced instantaneously decreases to 1 L / min.g$_{catalyst}$ from time to time. This situation can be adjusted by increasing the amount of NaBH$_4$ used according to the instantaneous hydrogen requirement of the system to which the generator will be connected.

4.2. Autonomous performance experiments

The autonomous experiments of a prototype were carried out using 2 g of NaBH$_4$, 20 ml of distilled water, and 0.5 g Co-BFS$^+$ catalyst powders were used. Hydrogen production performance and flowrates graphs of Co-BFS$^+$ catalyst powders are given in Figure 9 and Figure 10. In the experiment where 0.2 g Co-BFS$^+$ (%20, %30, %40, and %50) catalysts were used, the reaction times were 22, 24.41, 25.20, and 25.45 minutes, the maximum flow rate of the reaction were 1.93, 1.95, 1.86, and 1.92 L/min. g$_{catalyst}$, the instantaneous flow rates of the reaction were 12.30, 12.28, 13.27 and 13.03 L/min, and the total flow rates were 270.8, 307, 331.82, and 388.45 L, respectively. A series of experiments were carried out until the autonomous controlling and performance of the prototype were optimized. The results of the experiments were shown in Figure 11. Each part of the 4-segment generator was started when the rate of the previous segment's hydrolysis reaction decreased. A working time is designed to have a maximum instantaneous hydrogen production of 2.5 L / min. g$_{catalyst}$ continuously for 1 hour. In this working cycle, the amount of hydrogen produced instantaneously decreases to 1 L / min.g$_{catalyst}$ from time to time. This situation can be adjusted by increasing the amount of NaBH$_4$ used according to the instantaneous hydrogen requirement of the system to which the generator will be connected.

The result of this study, since it has an autonomous control and a segmented structure, hydrogen production can be done according to the needs of the system. This innovative hydrogen production method from directly solid chemical hydride has improved the reliability, and durability of the hydrogen generator system. Hydrogen gas produces sufficient amounts when needed, not compressed, and liquefied in the system. Thus, the use of excessive chemicals in the system is prevented and its safety is increased. Hydrogen gas can also be produced via a catalytic reaction from the liquid chemical hydride, but, this method supplies production that is lower than the solid chemical hydride. Also, the NaBO$_2$ chemical powder, which is released as a by-product as a result of the reaction, causes a decrease in the performance of the system, unstable hydrogen production, and low reliability. By-products released in the prototype system produced can be discharged from the system through the drainage channel. In addition, it does not need cartridge replacement and cleaning as in other hydrogen generators using solid chemical hydride.

5. Conclusions

As a result, this study was focused on a hydrogen generator prototype that can be used efficiently in hydrogen/fuel cells portable applications. The energy required for applications was provided from hydrogen gas which is produced with the use of hydrides that have high hydrogen

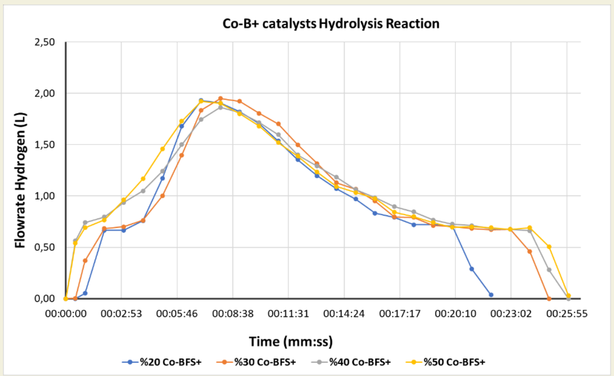

Figure 10. The flowrate hydrogen production of the Co-BFS+ catalyst sample that are different amounts of Co

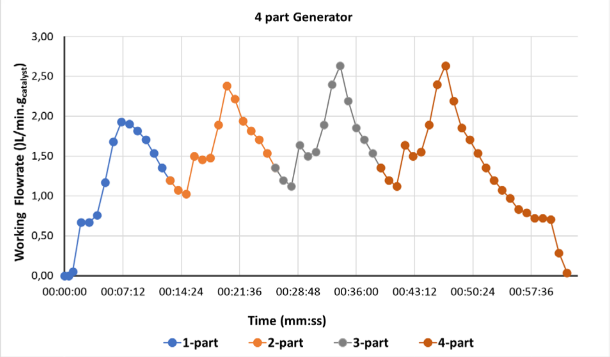

Figure 11. The performance of Autonomous Hydrogen Generator Prototype with %20 Co-BFS catalyst for 1-hour

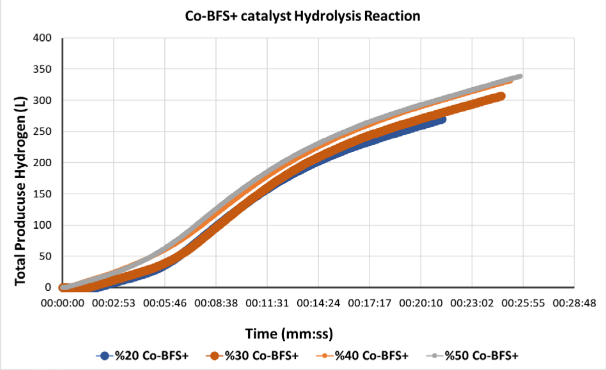

Figure 9. Hydrogen production performance graphs of Co-BFS+ catalyst powders

storage capacity in the catalytic hydrolysis reaction which occurs between water, the sodium borohydride, and the catalyst. According to the findings obtained from other studies in the literature, a new prototype was designed. This design provides high energy density, inexpensive design, low cost, high applicability, and fast use, refilling, or cleaning. However, this study shows the hydrolysis performance of pure Co nanopowder that is satisfactory fuel conversion and high hydrogen production rate at ambient temperature. With this study, it is aimed to close the gap related to the use of solid-state NaBH4 hydride in studies where hydrogen generator design and the use of pure Co powder as a catalyst in experiments in the literature. A new field of research has been opened regarding the use of by-products with high metal content and different pure nanopowders. The average flow rate results of the %40 Co-B-BFS(+) catalyst performance in the 4-part autonomous generator were almost 2.33 L/min.gcatalyst continuously for 1 hour.The maximum instantaneous hydrogen production flowrate the Co nano powder performance in the 4-part autonomous generator were almost 3 L/min.gcatalyst during 1 hour. Each part of the 4-part generator was started when the rate of the previous segment's hydrolysis reaction to decrease. In these working cycles, the soft ripples are spied on the hydrogen produced quantity from time to time. These ripple situations can be adjusted by increasing the quantity of NaBH4 used according to the instantaneous hydrogen requirement of the system to which the generator will be connected. So, new studies can be done to provide more stable hydrogen production by using different parameters.

In addition to these results, the energy needed by portable systems used in defence technologies is supply by traditional energy storage technologies, which are large in volume and heavy in mass. For these systems, it is of great importance to develop lighter and more efficient alternative applications such as hydrogen generators instead of heavy energy storage technologies. With the outputs obtained as a result of the prototype work, the problems in the insufficient energy capacity of the batteries used as the traditional method have been solved. The weight and volume of the systems have been reduced, thus increasing their duty times. Given the requirements in military or civilian life worldwide, it is important both academically and commercially to lead the development and manufacture of these systems, which are of high strategic importance due to the large gaps that exist in this market.

6. Acknowledgements

This research was supported by Prof. Dr. Ertuğrul Baltacıoğlu.

7. References

[1] Hansu, T.A., Caglar, A., Sahin, O., Kivrak, H., (2020). Hydrolysis and electrooxidation of sodium borohydride on novel CNT supported CoBi fuel cell catalyst. Materials Chemistry and Physics. doi: 10.1016/j.matchemphys.2019.122031.

[2] Barbir, F., (2005). PEM Fuel Cells.

[3] Sahiner, N., Demirci, S., (2017). Very fast H2 production from the methanolysis of NaBH4 by metal-free poly(ethylene imine) microgel catalysts. International Journal of Energy Research. doi: 10.1002/er.3679.

[4] Abdalla, A.M., Hossain, S., Nisfindy, O.B., Azad, A.T., Dawood, M., Azad, A.K., (2018). Hydrogen production, storage, transportation and key challenges with applications: A review. Energy Conversion and Management. doi: 10.1016/j.enconman.2018.03.088.

[5] Rivarolo, M., Improta, O., Magistri, L., Panizza, M., Barbucci, A., (2018). Thermo-economic analysis of a hydrogen production system by sodium borohydride (NaBH4). International Journal of Hydrogen Energy. doi: 10.1016/j.ijhydene.2017.11.079.

[6] Balbay, A., Saka, C., (2018). Effect of phosphoric acid addition on the hydrogen production from hydrolysis of NaBH4 with Cu based catalyst. Energy Sources, Part A: Recovery, Utilization and Environmental Effects. doi: 10.1080/15567036.2018.1463311.

[7] Schlesinger, H.I., Brown, H.C., Finholt, A.E., Gilbreath, J.R., Hoekstra, H.R., Hyde, E.K., (1953). Sodium Borohydride, Its Hydrolysis and its Use as a Reducing Agent and in the Generation of Hydrogen. Journal of the American Chemical Society. doi: 10.1021/ja01097a057.

[8] Zhang, J., Zheng, Y., Gore, J.P., Fisher, T.S., (2007). 1 kWe sodium borohydride hydrogen generation system. Part I: Experimental study. Journal of Power Sources. doi: 10.1016/j.jpowsour.2006.12.055.

[9] Amendola, S.C., Sharp-Goldman, S.L., Saleem Janjua, M., Kelly, M.T., Petillo, P.J., Binder, M., (2000). An ultrasafe hydrogen generator: Aqueous, alkaline borohydride solutions and Ru catalyst. Journal of Power Sources. doi: 10.1016/S0378-7753(99)00301-8.

[10] Kojima, Y., Suzuki, K.I., Fukumoto, K., Sasaki, M., Yamamoto, T., Kawai, Y., et al., (2002). Hydrogen generation using sodium borohydride solution and metal catalyst coated on metal oxide. International Journal of Hydrogen Energy. doi: 10.1016/S0360-3199(02)00014-9.

[11] Arzac, G.M., Hufschmidt, D., Jiménez De Haro, M.C., Fernández, A., Sarmiento, B., Jiménez, M.A., et al., (2012). Deactivation, reactivation and memory effect on Co-B catalyst for sodium borohydride hydrolysis operating in high conversion conditions. International Journal of Hydrogen Energy. doi: 10.1016/j.ijhydene.2012.06.117.

[12] Wang, F.C., Chiang, Y.S., (2012). Design and control of a PEMFC powered electric wheelchair. International Journal of Hydrogen Energy. doi: 10.1016/j.ijhydene.2012.04.156.

[13] Guo, Y.F., Chen, H.C., Wang, F.C., (2015). The development of a hybrid PEMFC power system. International Journal of Hydrogen Energy. doi: 10.1016/j.ijhydene.2015.01.169.

[14] Murooka, S., Tomoda, K., Hoshi, N., Haruna, J., Cao, M., Yoshizaki, A., et al., (2012). Consideration on fundamental characteristic of hydrogen generator system fueled by NaBH 4 for fuel cell hybrid electric vehicle. 2012 IEEE International Electric Vehicle Conference, IEVC 2012,.

[15] Kojima, Y., Suzuki, K.I., Fukumoto, K., Kawai, Y., Kimbara, M., Nakanishi, H., et al., (2004). Development of 10 kW-scale hy-

drogen generator using chemical hydride. Journal of Power Sources. doi: 10.1016/S0378-7753(03)00827-9.

[16] Kim, J.H., Lee, H., Han, S.C., Kim, H.S., Song, M.S., Lee, J.Y., (2004). Production of hydrogen from sodium borohydride in alkaline solution: Development of catalyst with high performance. International Journal of Hydrogen Energy. doi: 10.1016/S0360-3199(03)00128-9.

[17] Kim, T., Lee, J., (2011). A complete power source of micro PEM fuel cell with NABH4 microreactor. Proceedings of the IEEE International Conference on Micro Electro Mechanical Systems (MEMS),.

[18] Kim, T., (2011). Hydrogen generation from sodium borohydride using microreactor for micro fuel cells. International Journal of Hydrogen Energy. 36(2): 1404–10. doi: 10.1016/j.ijhydene.2010.10.079.

[19] Li, S.C., Wang, F.C., (2016). The development of a sodium borohydride hydrogen generation system for proton exchange membrane fuel cell. International Journal of Hydrogen Energy. doi: 10.1016/j.ijhydene.2015.12.019.

[20] Sim, J.H., Lee, C.J., Kim, T., (2014). Hydrogen generation from solid-state NaBH4 particles using NaHCO3 agents for PEM fuel cell systems. Energy Procedia,.

[21] Avrahami, I., Shvalb, N., Sasson, M., Nagar, Y., Dahan, O., Dayee, I., et al., (2020). Hydrogen production on-demand by hydride salt and water two-phase generator. International Journal of Hydrogen Energy. doi: 10.1016/j.ijhydene.2020.03.203.

[22] Zakhvatkin, L., Zolotih, M., Maurice, Y., Schechter, A., Avrahami, I., (2021). Hydrogen Production on Demand by a Pump Controlled Hydrolysis of Granulated Sodium Borohydride. Energy and Fuels. doi: 10.1021/acs.energyfuels.1c00367.

[23] İskenderoğlu, F.C., Baltacıoğlu, M.K., (2021). Effects of blast furnace slag (BFS) and cobalt-boron (Co-B) on hydrogen production from sodium boron hydride. International Journal of Hydrogen Energy. doi: 10.1016/j.ijhydene.2020.12.219.

[24] Liu, B.H., Li, Q., (2008). A highly active Co-B catalyst for hydrogen generation from sodium borohydride hydrolysis. International Journal of Hydrogen Energy. doi: 10.1016/j.ijhydene.2008.09.055.

[25] Kılınç, D., Şahin, Ö., (2019). Effective TiO2 supported Cu-Complex catalyst in NaBH4 hydrolysis reaction to hydrogen generation. International Journal of Hydrogen Energy. doi: 10.1016/j.ijhydene.2018.12.225.

EUROPEAN MECHANICAL SCIENCE
e-ISSN: 2587-1110

RESEARCH ARTICLE

Drying of mushroom slices in a new type solar drying system and under open sun: Experimental and mathematical investigation

Kamil Neyfel Çerçi[1], **Doğan Burak Saydam**[2,3], **Ertaç Hürdoğan**[2,3*]

[1]Department of Mechanical Engineering, Engineering Faculty, Tarsus University, Tarsus, Türkiye.
[2]Department of Energy Systems Engineering, Engineering Faculty, Osmaniye Korkut Ata University, Osmaniye, Türkiye
[3] Energy Education-Etude Application and Research Center, Osmaniye Korkut Ata University, Osmaniye, Türkiye.

Orcid: K.N. Çerçi (0000-0002-3126-707X), D.B. Saydam (0000-0001-8453-2917), E. Hürdoğan (0000-0003-1054-9964)

Abstract: Drying is among the beneficial food preservation strategies and this method ensures food products last before they reach consumers. The most used drying method is direct drying under the sun. However, in this method, the negative effects of the external environment damage food products. Recently, solar drying systems have been the main subject of much research as they have been protecting food from the negative effects of the external environment. In this study, a solar drying system (SD), which have a drying chamber with different structure, was used for drying mushroom. At the same time, mushroom slices were dried under open sun (OSD) for observing the performance of drying system. Drying rate (DR) and moisture ratio (MR) values were determined from the experiments. In addition, the MR values obtained from the experiments were estimated by 6 different mathematical models and 6 different machine learning algorithms. According to the results of the experiments, the drying time of the mushroom slices using SD was approximately 12.4 hours less than the drying time under open sun. The best convergence in the results gathered from the mathematical models is Sripinyowanich and Noomhorn and Hii et al. models for SD and OSD, respectively. The best estimation for MR values was realized by the Multilayer Perception algorithm for both drying methods.

Keywords: Drying, Solar Energy, Open Sun, Machine Learning Algorithm, Thin-Layer Mathematical Modeling, Mushroom

1. Introduction

Drying is a popular food preservation method that decreases the moisture content of the product to an ideal level to avoid several types of deterioration, such as enzymatic and microbiological growth [1]. It is a heat and mass transfer process performed to extend the shelf life of fruits or vegetables that cannot be consumed during the drying season and to prevent product losses. Therefore, drying is an important activity in the food production chain [2]. In drying, the moisture content of the products is reduced, and thus, the product is protected. There are many methods such as direct sun drying, drying with solar energy assisted systems, heat pump drying, and microwave drying for drying foods [3-6]. Solar-assisted energy technology is an economical and clean energy source, and its usage is very popular in drying applications [7]. Solar dryers have two different modes of operation, passive (natural convection) and active (forced convection) [8]. In addition, solar drying systems can be used frequently in drying applications, as the product is protected against rain, dust, insects and animals during drying [9]. Turkey, located between 36°N and 42°N latitude, has a suitable geographical location for solar energy. Turkey has an average yearly total sunlight length of 2640 hours (a daily total of 7.2 hours) and an average total irradiation of 1311 kWh/m^2-year (a daily total of 3.6 kWh/m^2) [10]. In this case, it increases the use of solar energy in many different applications, including drying applications [11-14]. Sun drying is the most prevalent way of preserving agricultural goods in most nations, including Turkey. However, this process is weather dependent and has issues with contamination with dust, dirt, and sand particles, drying time, time loss, and product loss [15]. Solar energy systems can be used easily in drying processes by having simple technology, low installation, and operating costs [16].

In the literature, there are many experimental and theoretical studies about solar energy-assisted drying systems. Aktas et al. [17] examined the drying of bay leaf in a closed-circuit heat-pump dryer. The researchers used ANN for modeling experimental data. Then, they evaluated the performance of the ANN model using indexes like the correlation coefficient (R^2), the root means square error (RMSE), and the mean absolute percentage error

---

[*] Corresponding author.
Email: ehurdogan@osmaniye.edu.tr

European Mechanical Science (2022), 6(4): 221-232
https://doi.org/10.26701/ems.1144456
Received: June 16, 2022 — Accepted: October 10, 2022

(MAPE). The authors concluded that the predicted results were consistent with the experimental results. Doymaz [18] studied the influence of blanching and drying temperature on the drying kinetics and rehydration ratio of sweet potatoes and used several mathematical models to simulate the experimental data. It was shown that the logarithmic model has the best fit for experimental drying data. Kooli et al. [19] investigated the drying of red pepper under the sun and in the greenhouse and determined the drying time and moisture content of the products. The authors have developed a drying model to verify the drying pattern for MR. It was seen that the results obtained from the drying models were in good agreement with the experimental data. Chokphoemphun [20] conducted a numerical and experimental study on paddy drying in a rectangular fluid-bed dryer by applying the principle of swirling flow. In the experimental study, the author investigated the drying process for two different air inlet temperatures and two different air speeds in a drying time of 5 hours. The researcher calculated the predictive results of the experimental study as R^2= 0,99556, MSE= 1.988E-4 and MAE=0.00127. Süfer et al. [21] studied the drying of onions under different conditions. Authors examined the experimental data with 13 thin-layer drying models to select the model that best describes the relevant parameter. As a result of the study, the authors determined that the most suitable model among the drying models was the Sigmoid model. The Sigmoid model was followed by Cubic and Midilli models with respect to R^2, RMSE, and χ^2. As a result of the study, the authors determined that the diffusion coefficients ranged from 1.962x10^{-9} to 1.372x10^{-8} m^2/s for convective, 9.757x10^{-9} and 1.723x10^{-8} m^2/s for vacuum, and 3.19310^{-8} to 9.139x10^{-7} m^2/s for microwave drying.

In this study, the mushroom slices were dried with the open sun drying (OSD) method and solar dryer (SD) with a new type drying chamber in Osmaniye climatic conditions to obtain the of drying characteristics and to make a system comparison. Experimentally obtained MR values of dried mushroom slices were also estimated using 6 different thin-layer drying models and 6 different machine learning algorithms.

2. Materials and Methods

2.1. Experimental Setup

Representative scheme of the system [22,23] at the Osmaniye Korkut Ata University/Karacaoğlan Campus is appeared in Figure 1. The two basic pieces of equipment in the system are the drying chamber and the solar air collector. The system also includes a control panel, fan, and air duct for the circulation of the drying air. The ambient air (state 1) firstly enters the collector and then is transferred to the air inlet tunnel via a fan. Drying air whose temperature has increased inside the collector (state 2) removes the moisture from the products in drying chamber and is discharged into the outdoor environment (state 3). The drying chamber with an inclined structure was used to obtain homogeneous temperature distribution and to increase the drying performance. More detailed information about the drying channel and the system can be found in the other studies of the authors [22-24].

A glass wool insulating material was placed on the lower and side sides of the system's 195x95x12 cm (1.70 m^2) plexiglass-cased air solar collector to help reduce the heat. A speed-controlled radial blower with a maximum flow rate of 650 m^3/hr and a power output of 70W was employed to circulate the air. Silicon was used to seal all the connecting points and areas where air flows through in order to prevent air leaks. Additionally, a layer of glass wool

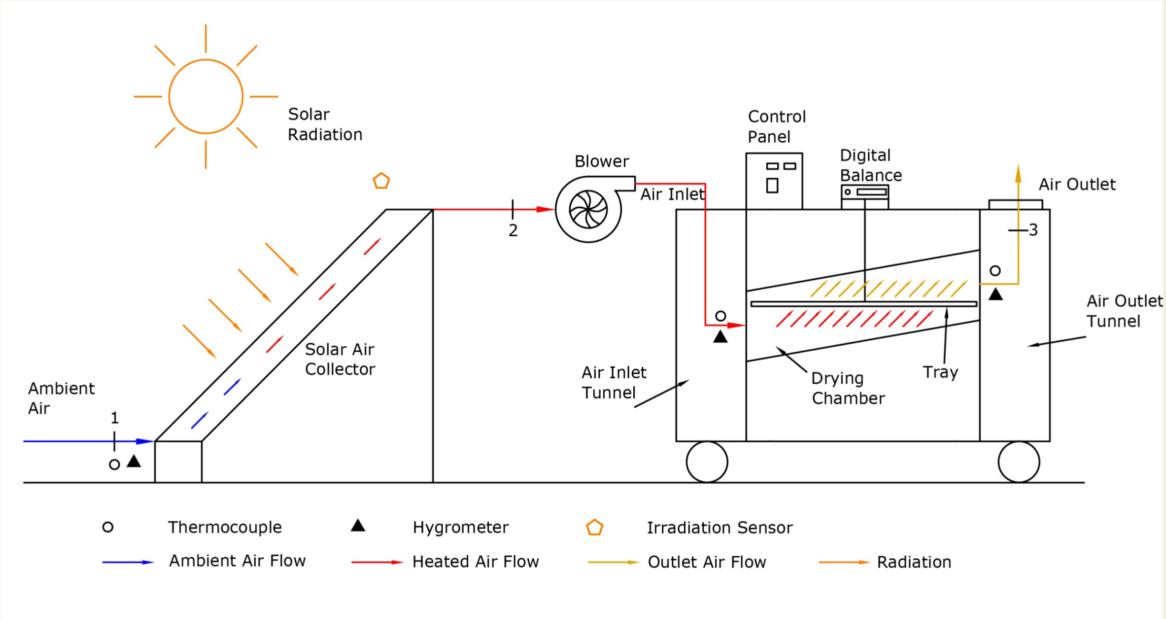

Figure 1. Solar drying system [22-24]

with an aluminum coating was placed atop the drying chamber to stop any potential heat losses. A transparent plastic sight glass is also included in the chamber for the purpose of monitoring the articles that need to be dried. Using a tray, the products that were to be dried were put inside drying chamber. To allow for air flow, a tray of roughly 0.5 m^2 was built of aluminium perforated wire. Following the product intake and introduction into the drying chamber, the tray is linked to the electronic scale by the chamber's hanger treatment (Figure 1-b).

2.2. Measurements and assessments of uncertainty

Measurements were taken at various stages (states 1-3) on the system (Figure 1) to assess the system's performance and the drying properties of the items to be dried. The temperature, relative humidity, and solar radiation were all measured by thermocouples, humidity transmitters, and irradiation sensors, in that order. The temperature measurements in the experiments were made with K type thermocouples. The air velocity measurement was carried out using an anemometer for defining the air mass flow rate. A computer-assisted data acquisition system was used to record the data within specified intervals. In the study, these measurement time intervals were determined as 15 minutes. The measurement equipment used for observing the performance of the experimental system is presented in Table 1. The most critical aspect influencing accuracy is mistakes that may occur throughout the trials for various reasons. The approach provided by Holman [25] was used for uncertainty (error) analysis. Uncertainty values of calculated parameter MR and DR are 2.30% and 2.60%, respectively.

Table 1. Measurement and analysis equipment

Device	Measurement parameters	Accuracy
TESTO 435 (Air Speed Probe)	Air velocity	0.1 m/s
COLE PARMER Thermocouple	Temperatures	0.1 °C
DİKOMSAN Electronic Balance	Product weight	0.1 g
EPLUSE Humidity Transmitter	Relative humidity	2-3 %
FRONIUS Irradiation sensor	Radiation	±5%
IOTECH PD3001 Data Logger	Data recording	16 bit

2.3. Thin-Layer Mathematical Modeling for Estimating MR

The quantity of moisture in food products is referred to as the product's water weight, and it is the most essential metric in drying procedures. Drying rate (DR, g_w / g_{dm}) and moisture ratio (MR) are used to determine drying behavior. DR is given in Equation 1 [26].

$$\mathrm{DR} = \left(\frac{\mathrm{M_{t+dt} - M_t}}{\mathrm{dt}}\right) \tag{1}$$

MR is calculated using Equation 2 [22,24].

$$\mathrm{MR} = \frac{\mathrm{M_t - M_e}}{\mathrm{M_0 - M_e}} \tag{2}$$

Here, $\mathrm{M_t}$ is defined as the amount of moisture at any time, $\mathrm{M_0}$ is the amount of moisture at the beginning of drying, and $\mathrm{M_e}$ is called the equilibrium moisture amount of the product. The $\mathrm{M_e}$ value is too small for $\mathrm{M_t}$ and $\mathrm{M_0}$. To simplify the computation of MR, $\mathrm{M_t}/\mathrm{M_0}$ is used instead of Equation 2 [26,27].

Mathematical, statistical, and numerical techniques are mostly used in drying processes to define the relationship among the different parameters of the system in the literature. In this study, the MR values gathered from the trials were estimated by different mathematical models. There are 6 mathematical models formed according to thin-layer drying used for modeling of MR and these models are presented in Table 2. Nonlinear regression analyses required to reveal the best model for defining the drying curve of the mushroom were carried out using the OriginPro 2017 software. The coefficient of correlation (R), the root mean squared error (RMSE) values were calculated to determine the convergence between MR obtained from experiments and from these equations.

The model with the highest R value and the lowest RMSE values obtained between the predicted results and experimental data was chosen as the best predicting model of MR values. The statistical values are calculated using the formula [21,26].

$$R = \frac{\sum_{i=1}^{n}(T_i - \bar{T})(P_i - \bar{P})}{\sum_{i=1}^{n}(T_i - \bar{T})^2 \sum_{i=1}^{n}(P_i - \bar{P})^2} \tag{3}$$

$$RMSE = [\frac{1}{N}\sum_{i=1}^{N}(MR_{pre,i} - MR_{exp,i})^2]^{\frac{1}{2}} \tag{4}$$

Ti and Pi are the neural network's target and predicted

Table 2. Methods used in modeling of MR

Model No	Model Constants	Formula	References
1	Hii et al.	y = a*exp (-k0*x^n) +b*exp (-k1*x^n)	[27]
2	Sigmoid	y = a + (b/(1+ exp(k*(x-c))))	[28]
3	Mod Midilli II	y = exp (-k*x) + b*x	[29]
4	Sripinyowanich and Noomhorn	y = exp (-k*x^n) + b*x + c	[30]
5	Noomhorn and Verma	y = a*exp (-k0*x) +b*exp (-k1*x) + c	[31]
6	Approximation of diffusion	y=(a*exp(-k*x))+((1-a)*exp(-k*b*x))	[32]

values; T and P are the neural network's average target and forecasted values; and n is total amount of input data. $MR_{exp,i}$ refers to the MR value obtained from the experimental observation, $MR_{pre,i}$ refers to the predicted MR value, N refers to the number of data obtained from observation, and n refers to the constants [21,26,33].

2.4. Machine Learning Algorithm for Estimating MR

Machine learning algorithms are divided into two classes as Unsupervised and Supervised Learning. The main element in supervised learning is the existence of a set of observations and the teaching of this training set to the system by a supervisor. As a result of this learning, it is necessary to make a prediction for a sample that has never been introduced before. As a consequence, the outcomes from the known data are used to develop the model for the solution. In this method, depending on the model developed, it is hoped to predict the results of data sets that lack label information. Most commonly used supervised learning algorithms can be listed as Multilayer Perceptron (MLP), Support Vector Machine (SVM) and M5P Tree (M5P), Random Forest (RF) [34].

In this study, MLP, SVM, RF and M5P algorithms were used to estimate the MR values obtained from the experiments carried out for drying of mushroom slices in SD and OSD. Input and output parameters used in machine learning algorithms for the predictive models are given in Table 3. These analyses were performed with Waikato Environment for Knowledge Analysis (WEKA) Version 3.8.3 software.

2.4.1. Support Vector Machine (SVM)

Support Vector Machines (SVM) is a classification method using structural risk minimization. The SVM was developed in 1995 by Cortesi and Vapnik for overcoming problems and increase the awareness of the unknown. The foundations of SVM originate from the theory of statistical learning, which is called as Vapnik-Chervonenkis (VC) theory [35]. The general structure of SVM is displayed in Figure 2 [36].

SVM method, called Support Vector Regression (SVR), was created for estimating functions [37, 38]. SVR has the ability to capture a nonlinear relationship in property space. Therefore, it is accepted as an effective solution method for regression applications. [39]. In this study, PolyKernel (SVM_{Poly}) and NormalizedPolyKernel (SVM_{NPoly}) are used. The equations expressing SVM_{Poly} and SVM_{NPoly} kernel functions are given in Eq. 5 and Eq. 6, respectively [40].

$$K(x_i, y_i) = ({x_i}^T x_i + 1)^p \tag{5}$$

$$K(x_i, y_i) = \frac{({x_i}^T x_i + 1)^p}{\sqrt{({x_i}^T x)({x_j}^T x_j)}} \tag{6}$$

2.4.2. M5P Tree

Quinlan [41], developed a new tree species, M5, to predict continuous variables. There is an important difference between the classification and regression tree (CART) and the M5 tree. The leaves of the regression trees created by CART have values. However, leaves of trees created by

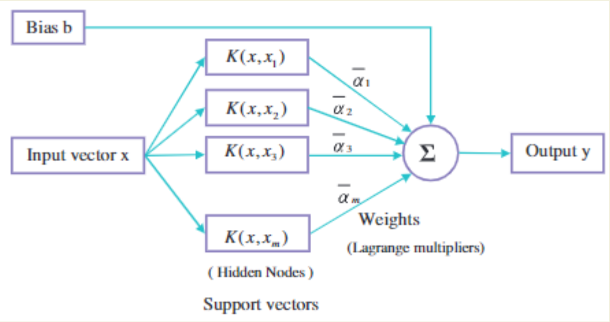

Figure 2. SVM's general structure [35]

Table 3. Input and output parameters

Input				
Method	Parameter	Unit	Min	Max
SD	Drying Time [t]	Second	0	59400
	Radiation [I]	W/m²	0	795.27
	Ambient Temperature [T]	°C	16.43	28.65
	Ambient Relative Humidity [Rh]	%	21.75	51.81
OSD	Drying Time [t]	Second	0	103500
	Radiation [I]	W/m²	0	798.38
	Ambient Temperature [T]	°C	14.01	28.65
	Ambient Relative Humidity [Rh]	%	21.75	59.15
		Output		
Method	Parameter	Unit	Min	Max
SD	Moisture Ratio [MR]	-	0	1
OSD	Moisture Ratio [MR]	-	0	1

M5 have multivariate linear patterns. This feature offers the possibility of estimating the difference more flexibly. The M5 tree has three main steps. These include building trees, pruning trees, and smoothing trees. Standard deviation reduction (SDR), a parameter that the M5 tree seeks to maximize [42]. The equation of the SDR is presented below:

$$SDR = sd(T) = \sum_{i} \frac{|T_i|}{|T|} x sd(T_i) \tag{7}$$

here T is the set of states, Ti is the ith subset of states obtained via tree splitting using a set of variables, sd(T) is T's standard deviation, and sd (Ti) is Ti's standard deviation.

An expanded variant of the M5 algorithm is the M5P algorithm [43]. One of primary benefits of model trees is their ability to efficiently analyze huge quantities of datasets with many features and high dimensions. Also, they are able to overcome the missing data problems [44] powerfully. The SDR value defined in the M5P algorithm has been changed to take into account the missing values as follows [42]:

$$SDR = \frac{m}{|T|} x \beta_i x \left[sd(T) - \sum_{j \in \{L,R\}} \frac{|T_j|}{|T|} x sd(T_j) \right] \tag{8}$$

where T is the set of training examples for a node, β(i) is the correction factor for enumerated features, T_L and T_R are the split subsets, and m is the number of training cases with no missing values for an attribute.

2.4.3. Random Forest (RF)

Random Forest (RF) is a machine learning technique that is based on decision trees and was developed by Leo Breiman. A decision forest is formed by combining multiple decision trees and the estimation results obtained from each decision tree are combined to make a final estimate. Therefore, RF is a community learning method [34].

For each node in the work of Amit and Geman, Breiman combined the Bagging and the Random Subspace method, influenced by the output that the best distinction was determined by a random selection. First, the bootstrap technique forms a sample independent of the inputs. Then Random Subspace method selects a randomly selected number of variables from all variables and the best branching of each node [45].

2.4.4. Multilayer Perception (MLP)

The artificial neural network (ANN) is a modeling and estimation method that offers an alternative way of addressing complex problems and has a large-scale acceptance rate. Multilayer Perception (MLP) network feed forward is a type of neural network. The MLP networks are composed of an input layer, one or more hidden and output layers. Each layer has a number of units called neurons. These units are fully connected to the unit in the next layer with the weight relations. Therefore, the general expression of this network is as follows [45].

$$y = f_2\left(\sum_{j=1}^{N} w_j f_1\left(\sum_{i=1}^{n} h_{ij} X_i + b_j\right) + b_0\right) \tag{9}$$

Here, y is predicted output, h_{ij}, b_j and f_1 are the weight matrix of the hidden layer, the bias factor of the hidden layer and the activation function of the hidden layer, respectively. w_j, b_0 and f_2 are the weight matrix of the output layer, the bias factor of the output layer and the activation function of the output layer, respectively [46].

Three layers make up the MLP model used in this investigation. Four neurons make up the input layer of the first layer. Eight neurons make up the second layer, sometimes known as the buried layer. The third layer, the output layer, is made up of one neuron. The hidden layer's activation function was determined to be the Sigmoid function. The learning rate was assumed to be 0.3. Figure 3 depicts the network structure.

3. Results and Discussions

In this study, through two days of experiments conducted in the Osmaniye climatic conditions, the drying properties of the mushroom slices were compared between open sun drying (OSD) and a solar collector-assisted drying system (SD). Before the experiment, contaminants such as dust and soil on the mushrooms were cleaned and products were cut into thin slices of almost the same size. The sliced products are arranged in a single row in trays to be used in the drying chamber and under the sun. The weight of the products placed on the tray was set to be approximately the same (1410 g). The drying process continued until the products reached equilibrium moisture. During the drying process, the measured parameters are incident radiation, product weight, temperature and relative humidity, respectively. As mentioned earlier, these measurements were performed at 15-minute intervals and

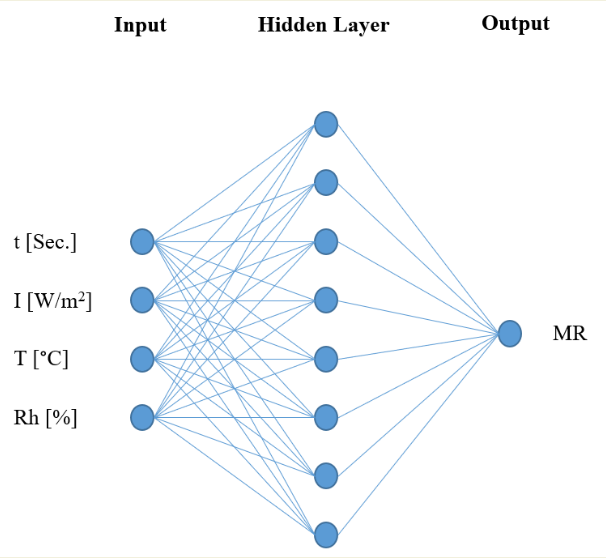

Figure 3. MLP structure used in MR estimation

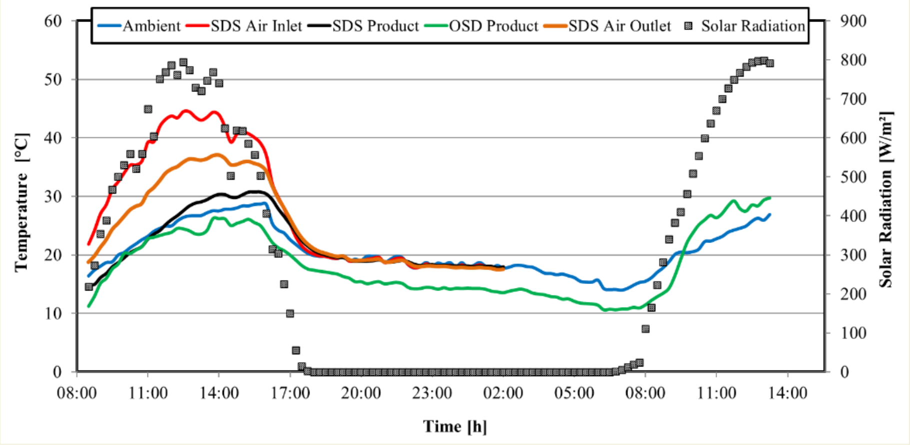

Figure 4. Variations of temperature and radiation during the drying of mushroom

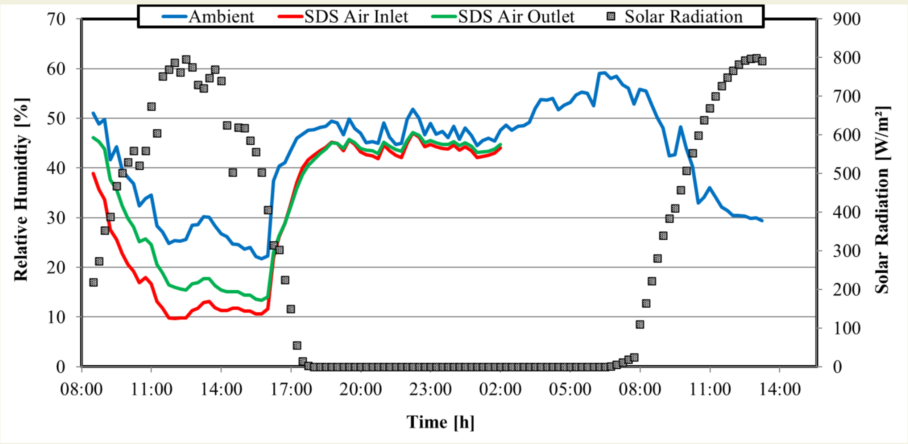

Figure 5. Variations of relative humidity and radiation during the drying of mushroom

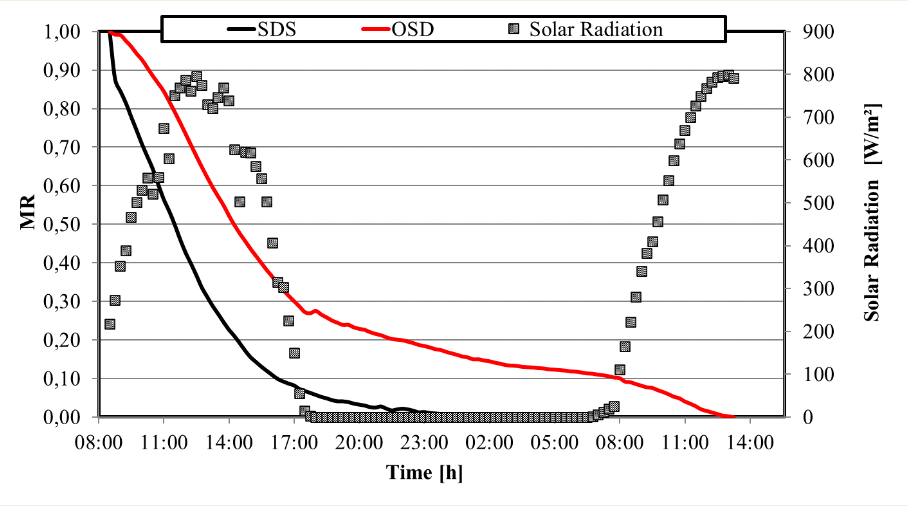

Figure 6. MR values of the dried mushrooms and solar radiation according to drying time in SD and OSD.

recorded.

Figure 4 represents the fluctuation in temperature and solar radiation recorded in the two drying procedures over the two-day continuous experiment with drying time. It was seen that the temperature values of different points varied depending on the radiation. Air at the inlet of the system (State 1-Ambient) gets warmed up in the collector (State 2-SD Air Inlet) and leaves the drying chamber (State 3-SD Air Outlet) at a temperature above the ambient temperature by taking the moisture from the product. During the drying process, the maximum temperatures within the drying chamber and outside were measured to be 44.48°C and 28.65°C, respectively, at sun radiation of 798.38 W/m^2. The temperature of the drying air and the ambient air increased until noon, and the temperature values decreased with zero radiation in the evening during the drying process. The maximum temperature values of the products in the open sun drying and the drying chamber were recorded as 30.77°C and 29.67°C, respectively. The results were shown that the dried products in SD were at higher temperatures throughout the drying process than the dried products in OSD. Especially due to the adverse weather conditions during the night, the product dried with OSD has decreased to low-temperature values compared with product dried with SD. Figure 5 shows the variation in relative humidity and radiation over the course of the two-day experiment as measured at various sites on the system. It was noticed that the highest results were found for the relative humidity values at the solar collector and the chamber inlet at 59% and 44%, respectively.

Figure 6 shows variation of the MR values obtained for SD and OSD and the radiation with drying time. The moisture loss in the product during the daylight hours was higher than during the evening hours because of the radiation effect for both SD and OSD. While the drying process was completed on the first day in SD, the drying process was completed at the end of the second day in OSD. It was observed that the varies in the MR of the product for OSD were affected more by the weather conditions especially during the night. In addition, considering the drying time, the drying process with SD has been determined to reach the equilibrium moisture content before drying with OSD (almost 12 hours early). This instance demonstrates the benefit of the SD system over the OSD approach. For SD and OSD, Figure 7 represents the change in drying rates (DR) of the mushroom with respect to MR through the drying process. In both plots, the first day drying rate was seen to be at its maximum value. It was presented that the DR curve of dried products in SD (Figure 7-a) showed a more regular change compared to the DR curve of the dried products in OSD (Figure 7-b). Figure 8 shows the picture of mushroom samples before and after drying in the SD. It is seen that the mushrooms dry and shrink through the drying process.

In this study, the experimentally obtained MR value for mushroom dried by both SD and OSD was estimated by 6 different thin-layer drying models and 6 different machine learning models. 6 thin-layer drying model constants, R, RMSE values are presented in Table 4 for MR experimentally obtained by SD. The best prediction among the nonlinear mathematical models was obtained by the Sripinyowanich and Noomhorn (Model No: 4) mathematical model since the model has the highest R (0.9998) and lowest RMSE (0.0051) rather than others.

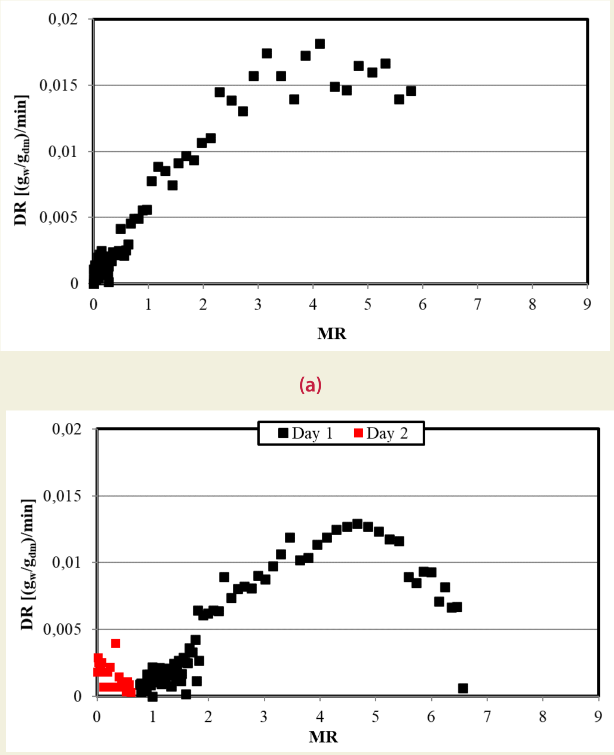

(a)

(b)

Figure 7. Variation of DR with MR values of mushroom dried with (a) SD and (b) OSD

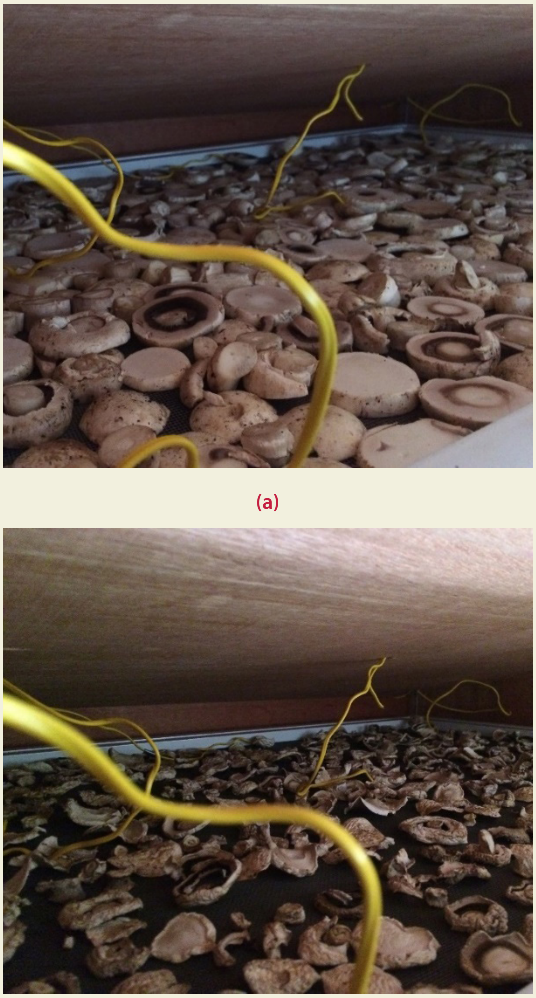

(a)

(b)

Figure 8. Picture of the mushroom slices before (a) and after (b) drying in the SD.

Table 4. Results from model studies for experimental MR obtained by drying mushrooms in SD

Model No	Model Constants	R	RMSE
1	a= 0.8967, k0= 2.463E-06, n= 1.337, b= 0.1033, k1= 0.08	0.9997	0.0061
2	a= -0.00886, b= 3.915, c= -1.25E+04, k= 8.455E-05	0.9996	0.0067
3	k= 7.3E-05, b=-2.955E-07	0.9967	0.0220
4	k=8.015E-06, n=1.216, b=1.064E-06, c=-0.05533	0.9998	0.0051
5	a=1.087, b= -0.07321, k0=7.634E-05, k1= 0.08, c=-0.01356	0.9992	0.0105
6	a=0.4896, b=1.001, k= 7.608E-5	0.9953	0.0265

Table 5. Statistical error rates obtained by estimating experimental MR values in mushroom drying with SD by different machine learning methods

Machine Learning Model	R	RMSE
MR_{M5P}	0.9864	0.0485
MR_{RF}	0.9899	0.0431
MR_{RT}	0.9898	0.0397
MR_{SVM}	0.9791	0.0569
MR_{SVM-II}	0.9781	0.0603
MR_{MLP}	0.9959	0.0252

The R and RMSE values were calculated by estimating the MR values of the mushrooms dried by SD with 6 different machine learning algorithms and predictive results of these models were presented in Table 5. The best estimate of the different machine learning was obtained with the Multilayer Perception (R=0.9959, RMSE = 0.0252).

In Table 6, 6 thin-layer drying model constants, R and RMSE values are given for OSD. The best prediction among the nonlinear mathematical models was obtained by the Hii et al. (Model No: 1) mathematical model since the model has the highest R (0.9975) and lowest RMSE (0.0197) rather than others. Table 7 shows R and RMSE results found by estimation of MR values of mushrooms dried by OSD with 6 different machine learning algorithms. The best estimate of the different machine learning was obtained with the Multilayer Perception Model (R=0,9998, RMSE=0.0122).

In Figures 9 and 10, the MR values are estimated by (a) MR_{M5P}, (b) MR_{MLP}, (c) $MR_{SVM-Poly}$, (d) $MR_{SVM-NPoly}$, (e) MR_{RT} and (f) MR_{RF} models were compared with experimental MR values for SD and OSD methods, respectively. It was observed that the estimates obtained with the Random Forest Model were almost the same with the experimental data. This shows that the method that best predicts MR values is the Random Forest method (MR_{RF}). Since the MR parameter in the OSD shows more fluctuation, the MR parameter obtained in the OSD is more difficult to predict via regression models. In addition, it was seen that the performance parameters obtained from the mathematical models developed for SD gave better results than the performance parameters of the mathematical models developed for OSD. However, the MR parameter obtained in OSD was estimated with higher accuracy by machine learning algorithms compared to the MR parameter obtained in SD. The drying process with OSD was completed later than the drying process with SD (approximately 12 hours). Therefore, the number of experimental data obtained for MR in OSD is greater than the number of data obtained for MR in SD. The more data in machine learning models, the more accurate predictions are performed. This explains why the performance parameters of the machine learning models obtained for MR in OSD are higher than the machine learning models obtained for MR in SD.

4. Conclusions

The drying behaviours of the mushroom were investigated during two days of tests in the province of Osmaniye's environment using solar aided drying systems (SD) and open sun drying (OSD). Additionally, six distinct mathematical models and six different computer methods were applied for evaluating the moisture ratio for the dried mushrooms. The remarkable results are as follows.

Table 6. Results from model studies for experimental MR obtained by drying mushrooms in OSD

Model No	Model Constants	R	RMSE
1	a=0.6878, k0=1.344E-07, n=1.596, b= 0.302, k1=1.786E-08	0.9975	0.0197
2	a=0.06871, b=2.257, c=-4099, k=5.653E-05	0.9937	0.0314
3	k=3.337E-05, b=1.484E-07	0.9889	0.0414
4	k=8.2000E-06, n= 1.3500, b= 1.0400e-06, c= -0.0800	0.9941	0.0302
5	a=1.081, b=-0.1272, k0=4.144E-05, k1=0.07, c= 0.04598	0.9939	0.0311
6	a=0.9931, b= -0.2303, k= 3.35E-05	0.9889	0.0415

- The total drying time obtained with SD was significantly reduced compared to the drying time obtained with OSD.
- The change in the MR values obtained with SD showed a smoother trend compared to the MR values obtained with OSD. The Sripinyowanich & Noomhorn model and Hii et al. model proved to become the best estimated non-linear mathematical models for the MR values obtained with SD and ODS, respectively.
- Among the machine learning algorithms, MR values of mushroom slices dried with SD and OSD were the best converging model of the Multilayer Perception (MLP) algorithm.
- In both drying methods, it was concluded that the MR found by the machine learning algorithms is

Table 7. Statistical error rates obtained by estimating experimental MR values in mushroom drying with OSD by different machine learning Methods

Machine Learning Model	R	RMSE
MR_{MSP}	0.9939	0.0364
MR_{RF}	0.9985	0.0191
MR_{RT}	0.9982	0.0194
MR_{SVM}	0.9894	0.0447
MR_{SVM-II}	0.9848	0.0502
MR_{MLP}	0.9998	0.0122

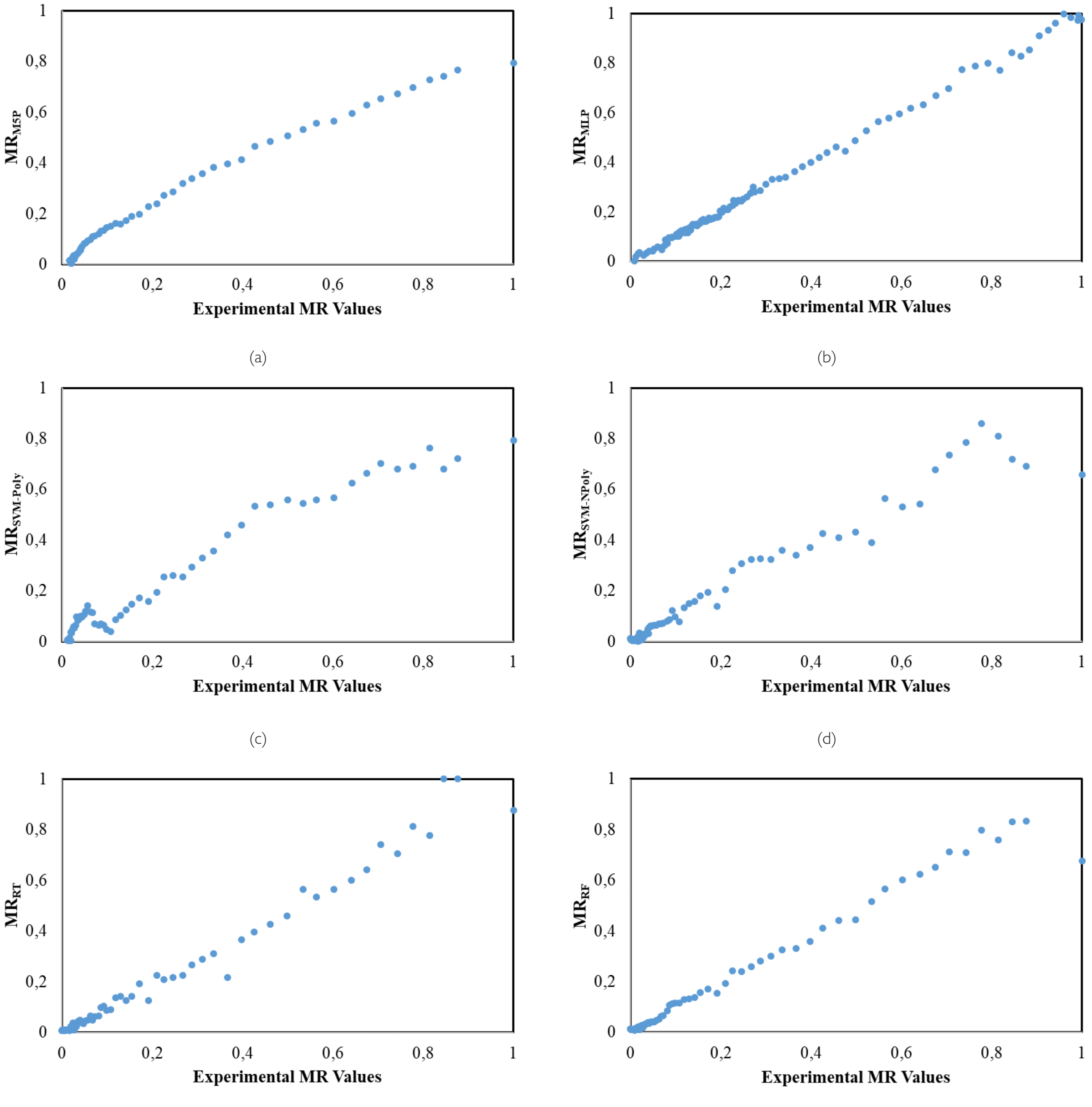

(a) (b) (c) (d) (e) (f)

Figure 9. Comparison of (a) MR_{MSP}, (b) MR_{MLP}, (c) $MR_{SVM-Poly}$, (d) $MR_{SVM-NPoly}$, (e) MR_{RT} and (f) MR_{RF} with experimental data obtained in SD.

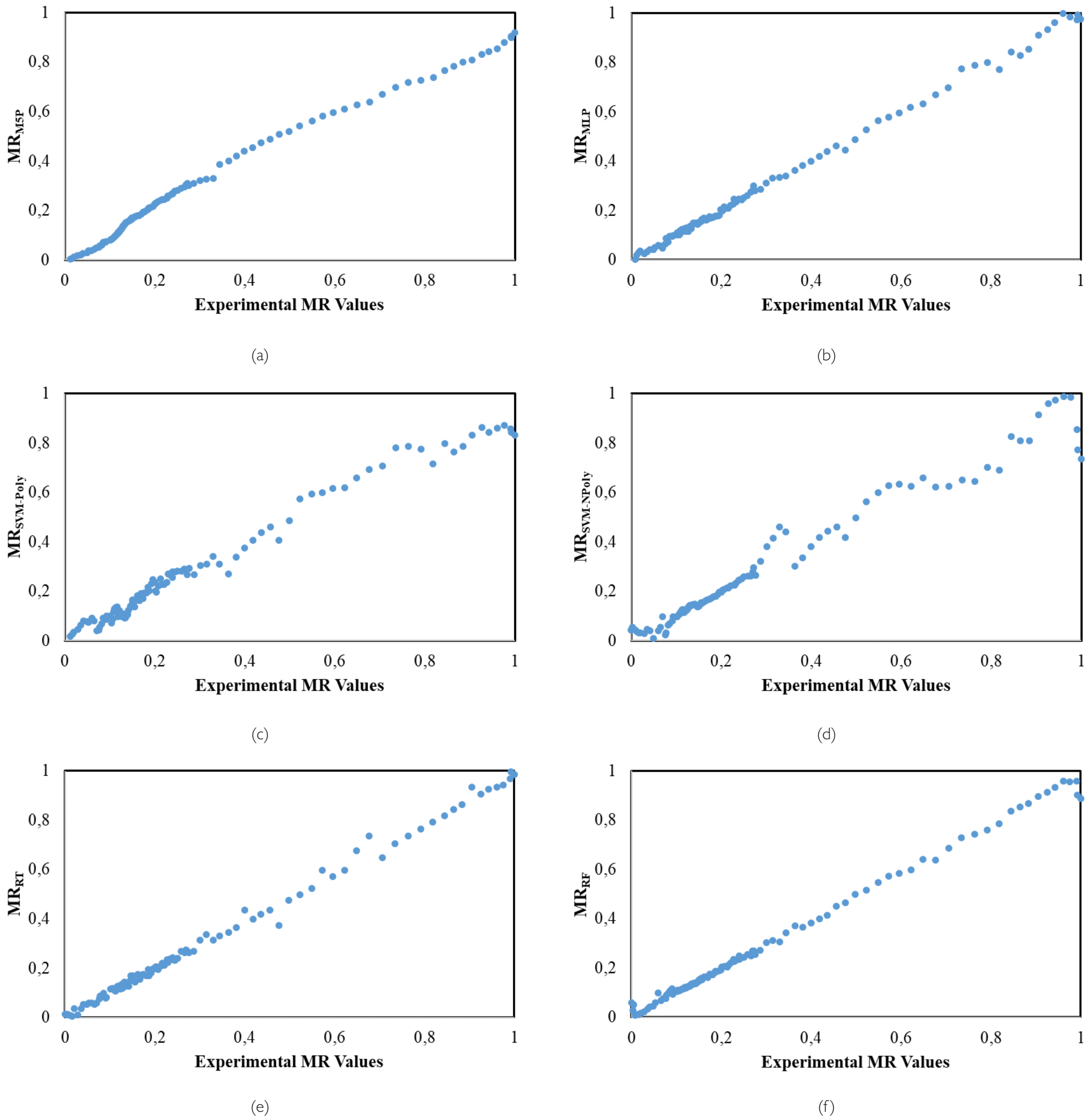

(a) (b) (c) (d) (e) (f)

Figure 10. Comparison of (a) MR$_{M5P}$, (b) MR$_{MLP}$, (c) MR$_{SVM-Poly}$, (d) MR$_{SVM-NPoly}$, (e) MR$_{RT}$ and (f) MR$_{RF}$ with experimental data obtained in OSD.

better matched with the actual data according to the mathematically obtained MR values.

- It has been stated that using machine learning algorithms for more accurate modeling of MR in drying applications will yield better results.

5. Acknowledgements

The Osmaniye Korkut Ata University's Scientific Research Projects Unit (OKUBAP) provided funding for this work under the terms of project OKUBAP-2014-PT3-032. We would like to thank OKÜBAP for their support.

6. References

[1] Argyropoulos, D., Heindl, A., Müller, J. (2011). Assessment of convection, hot-air combined with micro-wavevacuum and freeze-drying methods for mushrooms with regard to product quality. International Journal of Food Science and Technology, 333–342, https://doi.org/10.1111/j.1365-2621.2010.02500.x.

[2] Boroze, T., Desmorieux, H., Méot, J. M., Marouzé, C., Azouma, Y., Napo, K. (2014). Inventory and comparative characteristics of dryers used in the sub-Saharan zone: Criteria influencing dryer choice. Renewable and Sustainable Energy Reviews, 40, 1240-1259, https://doi.org/10.1016/j.rser.2014.07.058.

[3] Moses, J., Norton, T., Alagusundaram, K., Tiwari, B. (2014). Novel Drying Techniques for the Food Industry. Food Enginering Review, 43-55, DOI 10.1007/s12393-014-9078-7.

[4] Hnin, K. K., Zhang, M., Mujumdar, A. S., Zhu, Y. (2018). Emerging food drying technologies with energy-saving characteristics: A review. Drying Technology, 1465-1480,

https://doi.org/10.1080/07373937.2018.1510417.

[5] Uthpala, T. G. G., Navaratne, S. B., Thibbotuwawa, A. (2020). Review on low-temperature heat pump drying applications in food industry: Cooling with dehumidification drying method. Journal of Food Process Engineering, 43(10), e13502, https://doi.org/10.1111/jfpe.13502.

[6] Duan, X., Yang, X., Ren, G., Pang, Y., Liu, L., Liu, Y. (2016). Technical aspects in freeze-drying of foods. Drying Technology, 34(11), 1271-1285, https://doi.org/10.1080/07373937.2015.1099545.

[7] Mustayen, A., Mekhilef, S., Saidur, R. (2014). Performance studyofdifferentsolardryers:A review. Renewable and Sustainable Energy Reviews , 463–470, https://doi.org/10.1016/j.rser.2014.03.020.

[8] Tiwari, S., & Tiwari, G. N. (2016). Exergoeconomic analysis of photovoltaic-thermal (PVT) mixed mode greenhouse solar dryer. Energy, 114, 155-164, https://doi.org/10.1016/j.energy.2016.07.132.

[9] VijayaVenkataRaman, S., Iniyan, S., & Goic, R. (2012). A review of solar drying technologies. Renewable and sustainable energy reviews, 16(5), 2652-2670, https://doi.org/10.1016/j.rser.2012.01.007.

[10] Stritih, U., Osterman, E., Evliya, H., Butala, V., Paksoy, H. (2013). Exploiting solar energy potential through thermal energy storage in Slovenia and Turkey. Renewable and Sustainable Energy Reviews, 442–461, https://doi.org/10.1016/j.rser.2013.04.020.

[11] Mugi, V. R., Das, P., Balijepalli, R., & Chandramohan, V. P. (2022). A review of natural energy storage materials used in solar dryers for food drying applications. Journal of Energy Storage, 49, 104198, https://doi.org/10.1016/j.est.2022.104198.

[12] Olmuş, U., Güzelel, Y. E., Pınar, E., Özbek, A., Büyükalaca, O. (2022). Performance assessment of a desiccant air-conditioning system combined with dew-point indirect evaporative cooler and PV/T. Solar Energy, 231, 566-577, https://doi.org/10.1016/j.solener.2021.12.004.

[13] Kutlu, C., Erdinc, M. T., Li, J., Wang, Y., Su, Y. (2019). A study on heat storage sizing and flow control for a domestic scale solar-powered organic Rankine cycle-vapour compression refrigeration system. Renewable Energy, 143, 301-312, https://doi.org/10.1016/j.renene.2019.05.017.

[14] Srinivasan, G., Muthukumar, P. (2021). A review on solar greenhouse dryer: Design, thermal modelling, energy, economic and environmental aspects. Solar Energy, 229, 3-21, https://doi.org/10.1016/j.solener.2021.04.058.

[15] Wang, H., Zhang, M., Mujumdar, A. S. (2014). Comparison of Three New Drying Methods for Drying Characteristics and Quality of Shiitake Mushroom (Lentinus edodes). Drying Technology, 1791–1802, https://doi.org/10.1080/07373937.2014.947426.

[16] Fudholi, A., Sopian, K. (2019). A review of solar air flat plate collector for drying application. Renewable and Sustainable Energy Reviews , 333–345, https://doi.org/10.1016/j.rser.2018.12.032.

[17] Aktaş, M., Şevik, S., Özdemir, M. B., Gönen, E., (2015). Performance analysis and modeling of a closed-loop heat pump dryer for bay leaves using artificial neural network. Applied Thermal Engineering, 87, 714-723. http://dx.doi.org/ 10.1016/j.applthermaleng.2015.05.049.

[18] Doymaz, İ. (2011). Thin-layer drying characteristics of sweet potato slices and mathematical modelling. Heat Mass Transfer, 47, 277–285. http://dx.doi.org/ 10.1007/s00231-010-0722-3.

[19] Kooli. S., Fadhel. A., Farhat. A., Belghith. A. (2007). Drying of red pepper in open sun and greenhouse conditions Mathematical modeling and experimental validation. Journal of Food Engineering 79 (2007) 1094–1103, https://doi.org/10.1016/j.jfoodeng.2006.03.025.

[20] Chokphoemphuna, S., Chokphoemphunb A. (2018). Moisture content prediction of paddy drying in a fluidized-bed drier with a vortex flow generator using an artificial neural network. Applied Thermal Engineering, 145, 630–636. http://dx.doi.org/ 10.1016/j.applthermaleng.2018.09.087.

[21] Süfer, Ö., Sezer, S., Demir, H. (2017). Thin layer mathematical modeling of convective, vacuum and microwave drying of intact and brined onion slices. Journal Of Food Processıng and Preservatıon, 41, 1-13. http://dx.doi.org/ 10.1111/jfpp.13239.

[22] Çerçi, K., N., Süfer, Ö., Söyler , M., Hürdoğan , E., Özalp , C. (2018). Thın Layer Dryıng of Zucchını In Solar Dryer Located In Osmanıye Regıon, Tehnıčkı Glasnık, 12, 79-85, http://dx.doi.org/ 10.31803/tg-20180126094515.

[23] Akman, H. (2017). Thermodynamic Analysis of a Solar Energy Assisted Drying System, MSc Thesis (in Turkish) , Osmaniye Korkut Ata University, Osmaniye.

[24] Hürdoğan, E., Çerçi, K. N., Saydam, D. B., Ozalp, C. (2022). Experimental and modeling study of peanut drying in a solar dryer with a novel type of a drying chamber. Energy Sources, Part A: Recovery, Utilization, and Environmental Effects, 44(2), 5586-5609, https://doi.org/10.1080/15567036.2021.1974126.

[25] Holman JP. (2001). Experimental methods for engineers. 8th ed. McGraw Hill.

[26] Kavak Akpinar, E., Toraman, S., (2016). Determination of drying kinetics and convective heat transfer coefficients of ginger slices. Heat Mass Transfer, 52, 2271–2281. http://dx.doi.org/ 10.1007/s00231-015-1729-6.

[27] Hii, C. L., Law, C. L., Cloke, W. (2009). Modeling using a new thin layer drying model and product quality of cocoa. Journal of Food Engineering, 90, 191-198. https://doi.org/10.1016/j.jfoodeng.2008.06.022.

[28] Figiel, A. (2009). Drying kinetics and quality of vacuum-microwave dehydrated garlic cloves and slices. Journal of Food Engineering, 94, 98-104. https://doi.org/10.1016/j.jfoodeng.2009.03.007.

[29] Erbay, Z. Icier, F., (2010). A review of thin-layer drying of foods: theory, modeling, and experimental results. Critical Reviews in Food Science and Nutrition, 50, 441-464. https://doi.org/10.1080/10408390802437063.

[30] Sripinyowanich, J. Noomhorm, A. (2011). A new model and quality of unfrozen and frozen cooked rice dried in a microwave vibro-fluidized bed dryer. Drying Technology, 29, 735-748. https://doi.org/10.1080/07373937.2010.535399.

[31] Noomhorn, A. Verma, L. R. (1986). Generalized single-layer rice drying models. Transactions of the ASAE, 29, 587-591. https://doi.org/10.13031/2013.30194.

[32] Yaldız, O., Ertekin, C., (2001). Thin layer solar drying of some vegetables. Drying Technology, 19, 583–596. http://dx.doi.org/ 10.1081/DRT-100103936.

[33] Sun, Y., Zhang, M., Mujumdar, A. S., & Yu, D. (2021). Pulse-spouted microwave freeze drying of raspberry: Control of moisture using ANN model aided by LF-NMR. Journal of Food Engineering, 292, 110354, https://doi.org/10.1016/j.jfoodeng.2020.110354.

[34] Şanlitürk, E. (2018). Prediction of Defective Product with Machine Learning Algorithms, MSc Thesis (in Turkish) Istanbul: Istanbul Teknik University.

[35] Ayhan, S., Erdoğmuş, Ş. (2014). Kernel Function Selection for the Solution of Classification Problems via Support Vector Machines. Eskişehir Osmangazi University Journal of Economics and Administrative Sciences, 9(1), 175-201.

[36] Deka, P. C. (2014). Support vector machine applications in the field of hydrology: a review. Applied soft computing, 19, 372-386, https://doi.org/10.1016/j.asoc.2014.02.002.

[37] Henderson, S. M. Pabis, S. (1961). Grain drying theory I: temperature effect on drying coefficient. Journal of Agricultural Engineering Research, 6, 169-74.

[38] Karimipour, A., Bagherzadeh, S., A., Taghipour, A., Abdollahi, A., Safae, M., R. (2019). A novel nonlinear regression model of SVR as a substitute for ANN to predict conductivity of MWCNT-CuO/water hybrid nanofluid based on empirical data. Physica A, 521, 89-97. https://doi.org/10.1016/j.physa.2019.01.055.

[39] Das, M., Akpinar, E., K. (2018). Investigation of Pear Drying Performance by Different Methods and Regression of Convective Heat Transfer Coefficient with Support Vector Machine. Applied Science, 8, 215. doi:10.3390/app8020215.

[40] Sattari, M. T., Feizi, H., Colak, M. S., Ozturk, A., Apaydin, H., Ozturk, F. (2020). Estimation of sodium adsorption ratio in a river with kernel-based and decision-tree models. Environmental Monitoring and Assessment, 192(9), 1-13, https://doi.org/10.1007/s10661-020-08506-9.

[41] Quinlan, J. R. (2014). C4. 5: programs for machine learning. Elsevier.

[42] Zhan, C., Gan, A., Hadi, M. (2011). Prediction of lane clearance time of freeway incidents using the M5P tree algorithm. IEEE Transactions on Intelligent Transportation Systems, 12(4), 1549-1557, Doi: 10.1109/TITS.2011.2161634.

[43] Güzelel, Y. E., Olmuş, U., Çerçi, K. N., Büyükalaca, O. (2021). Comprehensive modelling of rotary desiccant wheel with different multiple regression and machine learning methods for balanced flow. Applied Thermal Engineering, 199, 117544, https://doi.org/10.1016/j.applthermaleng.2021.117544.

[44] Behnood, A., Behnood, V., Gharehveran, M. M., Alyamac, K. E. (2017). Prediction of the compressive strength of normal and high-performance concretes using M5P model tree algorithm. Construction and Building Materials, 142, 199-207, https://doi.org/10.1016/j.conbuildmat.2017.03.061.

[45] Akman, M. (2010). An overview of data mining techniques and analysis of Random Forests method: An application on medical field, MSc Thesis (in Turkish), Ankara University, Ankara.

[46] Messikha,N., Bousbaa, S., Bougdaha N. (2017). The use of a multilayer perceptron (MLP) for modelling the phenol removal by emulsion liquid membrane. Journal of Environmental Chemical Engineering. 5, 3483–3489. http://dx.doi.org/10.1016/j.jece.2017.06.053.

EUROPEAN MECHANICAL SCIENCE
e-ISSN: 2587-1110

Investigation of weld defects and mechanical properties of dissimilar friction stir spot welded dual phase (DP600) steel and aluminum alloy (AA 7075-T6) plates

Ahmet Cakan[1], **Mustafa Ugurlu**[2*]

[1] Dept. of Mechanical Engineering, Mersin University, Mersin 33343, Turkey
[2] Adana Organized Industrial Zone Vocational School of Technical Sciences, Cukurova University, Adana, Turkey

Orcid: A. Cakan (0000-0002-7394-1499), M. Ugurlu (0000-0002-1194-7772)

Abstract: DP600 steel and AA7075-T6 aluminium alloy plates were joined using the friction stir spot welding process. The effects of different tool rotational speeds on the mechanical properties, intermetallic compound formation and interface microstructure of welded joints were investigated. The highest lap shear tensile load was obtained from the samples joined at a rotational speed of 1040 rpm (6.5 kN). It was determined that the tensile load of the welded joint decreased with increasing tool rotational speed. XRD analysis performed on broken surfaces, the intermetallic phase was determined to be $Al_{13}Fe_4$. As a result of Vickers microhardness tests, the samples joined at 1320 rpm and 1500 rpm, in the structure of which intermetallic compounds were determined by XRD analysis, displayed higher hardness values. In addition, when scanning electron microscope images were examined, it was determined that the cracks observed in the samples and the porosity both increased with increasing tool rotational speed.

Keywords: Dissimilar welding, Intermetallic compounds, Mechanical properties, DP600, AA7075-T6.

1. Introduction

Improving passenger safety, reducing fuel consumption, and decreasing carbon emissions are issues of priority for the automotive industry. Although weight reduction is possible by using light materials such as Al alloys, joining different types of materials has come to the fore as a method to provide sufficient strength values. For this reason, the joining of high-strength steel and light aluminium materials became a critical subject for the automotive industry [1,2]. The dissimilar welding of Al and steel materials comes to the fore due to the combination of lightness and high strength properties. However, the application of the traditional resistance spot welding (RSW) process, which is used extensively in the industry [3], is not efficient in dissimilar Al-steel joining. As a result of its very different physical and metallurgical properties, it is prone to the formation of brittle intermetallic compounds. In addition the fusion welded joints of dissimilar materials have welding defects like cavities, porosities, and cracks [4]. Therefore, solid-state welding methods are preferred in joining different types of Materials [5-7]. Friction stir welding (FSW), developed by The Welding Institute (TWI) in 1991, is a solid-state welding method with low distortion, fewer welding defects, and good mechanical properties, as it is a process that takes place below the melting temperature [8-18]. Using this process, it is possible to successfully join materials with very different properties [19-21]. An application of FSW process to one-point joint is known as friction stir spot welding (FSSW) [22,23]. The FSSW technique, which is a joining method that consists of three stages, was derived from FSW process. After a rotary tool is immersed in overlapping plates at a certain depth, it is allowed to dwell for the specified time and then retracted without horizontal movement [24-26]. FSSW is now recognized as one of the most successful methods for joining of dissimilar metals [27,28]. In addition, due to the advantages of the FSSW method such as low energy requirement and low cost, the FSSW technique has been replacing RSW in the automotive industry [29].

In the FSSW process, despite the relatively low heat input The presence of various intermetallic phases was observed at the weld interface [30]. Hsieh et al. [31] determined that Fe_2Al_5 and $Fe4Al_{13}$ intermetallic compounds were formed at the interface in the joining of SS400 steel and AA6061 aluminum alloy. Although the parameters of

---

[*] Corresponding author.
Email: mugurlu@cu.edu.tr

European Mechanical Science (2022), 6(4): 233-240
https://doi.org/10.26701/ems.1161862
Received: August 14, 2022 — Accepted: October 10, 2022

pin and shoulder design, tool rotational speed and dwell time are considered as basic FSSW parameters, the plunge depth of the tool is also considered as an important welding parameter. Haghshenas et al. [32], by plunging the tool into the steel material below, determined that a lower intermetallic layer was formed and the bonding was better. However, materials such as carbides or cubic boron nitride, which are more durable than steel, should be used as tool materials for this method. On the other hand joining can be performed by diffusion without plunging materials into the plate at the bottom [28]. Also the diffusion joint is mostly preferred due to the limited plunging in thin sheets. The method of joining by diffusion has come to the fore as tools require lower strength with the contact of the tool to the softer material at the top, and, as a result, tools produced with less costly material can be used. Fereudini et al. [33] investigated the technique of diffusion bonding using a 2.8-mm-long pin for welding 3-mm-thick Al-5083 and 1 mm thick St-12 sheets. It was determined that the plates joined with rotational speed of 900 rpm had better bond strength than the plates joined with rotational speed of 1100 rpm. In this study, due to the use of thin steel plates and to prevent excessive wear of the tool, diffusion bonding was preferred. Also the effects of various tool rotational speeds (1040 rpm, 1320 rpm, 1500 rpm) on welding defects and mechanical properties in joining AA7075-T6 Al alloy plates with DP600 steel plates using FSSW were investigated.

2. Materials and Methods

Aluminium alloy (AA7075-T6) sheets of 100 × 30 × 3 mm and steel (DP600) sheets of 100 × 30 × 1.2 mm were used for the FSSW process. The experiments were carried out under room conditions, with an overlapping area of 30 mm × 30 mm, with an aluminum plate were placed on top of the steel plate. The chemical compositions of AA7075-T6 alloy and DP600 steel were given in Table 1 and Table 2 respectively, mechanical properties of AA7075-T6 alloy and DP600 steel used in the study were given in Table 3. The FSSW of the plates was made using a vertical spindle type 2.8 kW FIRST LC20VGN milling machine. FSSW is a joining method that entails three different stages. After a rotary tool is plunged into plates at a certain depth, it is left to dwell for the specified time and is then retracted without horizontal movement (Fig. 1).

A stirring tool made of hot work tool steel (H13) was used in the FSSW processes. The tool is manufactured with a shoulder diameter of 20 mm, a conical pin diameter of 4-6 mm and a pin length of 2.8 mm. Fig. 2a shows the schematic diagram of the tool. The plates were joined according to various rotational speeds, namely 1040, 1320, and 1500 rpm. In order to determine the effect of tool rotational speed on welding performance, the dwelling time was kept constant for 10 s and the tool was turned clockwise. The plunging amount of the rotating tool was adjusted by the movement of the milling table in the vertical direction followed by waiting for 10 seconds. The joint performance was determined by conducting metallographic analysis (i.e. scanning electron microscopy, X-ray diffraction analyses), microhardness measurements, and tensile tests. For the preparation of the metallography samples shown in Figure 2d, the wire EDM technique was used. Then samples were sanded with silicon carbide papers of 400, 600, 1200, and 2000 grade and polished with alumina suspensions. Cross sectioned samples were etched with a solution of 2 mL of HF, 3 mL of HCl, and 15 mL of HNO_3 in distilled water for metallographic

Table 1. Chemical composition of AA7075-T6.

Si	Fe	Cu	Mn	Mg	Cr	Ni	Zn	Ti	Zr	Al
0.07	0.14	1.6	0.06	2.7	0.19	60 ppm	5.8	0.02	0.01	89.4

Table 2. Chemical composition of DP600.

C	Mn	Si	S	Al	P
0.092	1.912	0.147	0.003	0.031	0.014

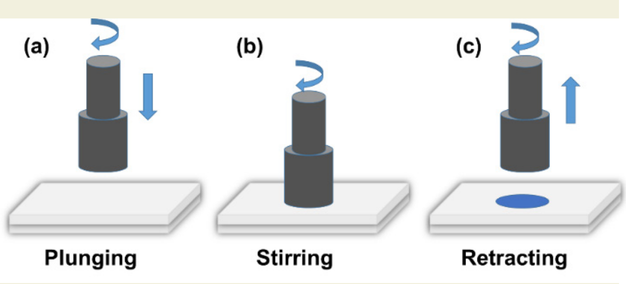

Figure 1. Schematic illustration of the FSSW process (a) plunging stage (b) stirring stage c) retracting stage.

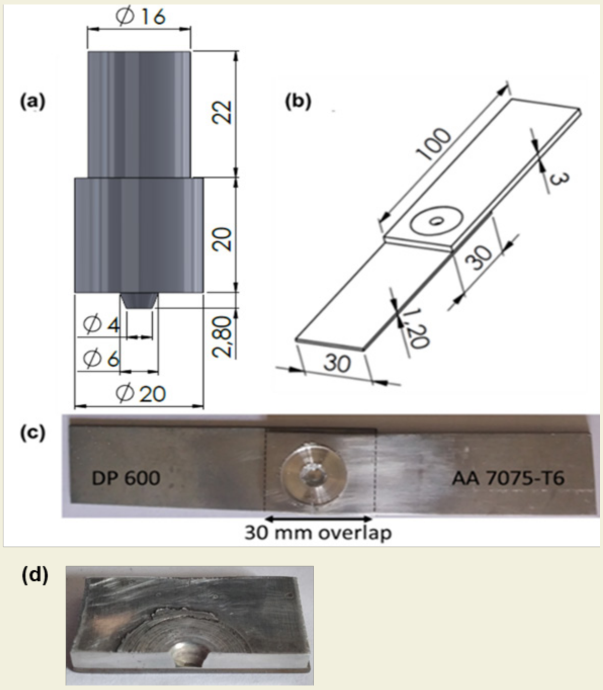

Figure 2. (a) Schematic diagram of the tool used in the FSSW process (b) Dimensions of the friction stir spot welded joint c) pictorial image of the as welded sample. d) pictoral image of the metallographic analysis sample

Table 3. Mechanical properties of the DP600 and AA 7075-T6.

Material	Tensile Strength (MPa)	Yield Strength (MPa)	Elongation Rate (%)	Modulus of Elasticity (GPa)	Hardness (HV)
DP 600	630	370	24	20	170
AA 7075-T6	572	503	11	71	175

analysis (Fig. 2d).

In addition, microhardness measurements were performed on the cross section of the welded plates to determine the hardness changes in the stir zones. For microhardness measurements, Vickers hardness test (Bulut, Microbul) method was used with a load of 100 grams with a loading time of 10 seconds. Fig. 2c and Fig. 2d shows a pictorial image of the as-welded sample that was used for the tensile shear tests and metallographic analyses respectively. For tensile shear test, a minimum of three tensile specimens for each parameter were tested using a loading speed of 1 mm/min (Fig. 2b).

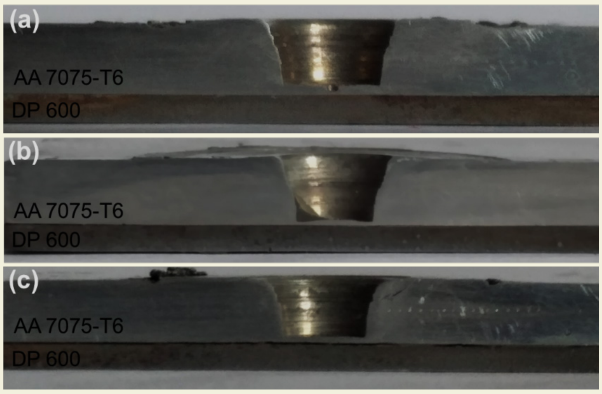

Figure 3. Cross-sectionol views of welded joints according to various tool rotational speeds, (a) 1040 rpm, (b) 1320 rpm, and (c) 1500 rpm.

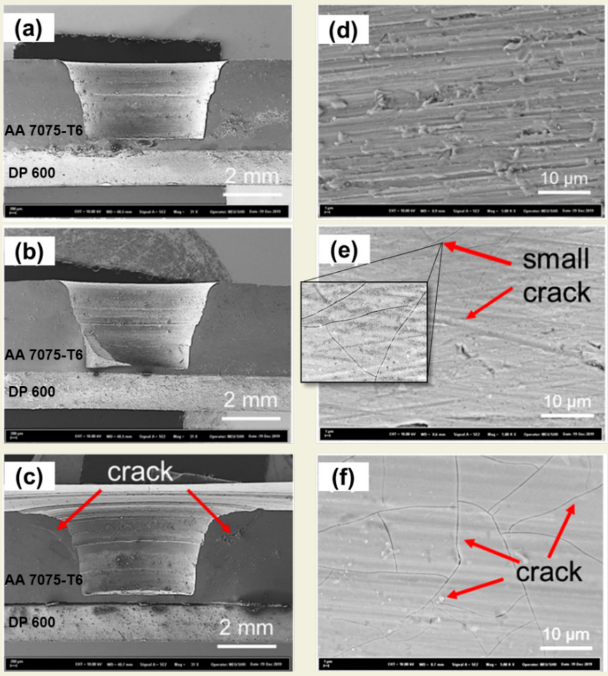

Figure 4. SEM images of welded joints according to various tool rotational speeds, (a-d) 1040 rpm, (b-e) 1320 rpm, and (c-f) 1500 rpm.

3. Results and discussion

3.1. Microstructural investigations

The cross-sectional views of Al plates and steel plates joined using different tool rotational speeds are shown in Fig. 3. According to the SEM images, there was no apparent weld defect in the samples joined at 1040 rpm (Fig. 4a) and 1320 rpm (Fig. 4b). In the sample joined at 1500 rpm (Fig. 4c), the presence of cracks in the area below the shoulder was observed. The presence of liquation cracks, whereby cracks occur during the formation of partially melting regions with the heat generated by friction and solidification of those regions, can be seen in Fig. 4c.

Gerlich et al. [34] determined that during the dwell time, reverse flow occurs as a result of the downward force acting on the material under the shoulder of the tool. Yamamoto et al. [35] determined that this reverse flow causes the material to move upwards following the stir zone boundary, and they explained this as the cause of liquation cracks.

It was observed in the SEM images of the region near the pin gap below the shoulder that the sample joined at 1040 rpm (Fig. 4d) did not have significant weld defects, but there were thin cracks in the sample joined at 1320 rpm (Fig. 4e). In addition, the sample joined at 1500 rpm (Fig. 4f) had more prominent and dense cracks, and it was determined that the cracks increased with the tool rotational speed. Since more heat is produced at high tool rotational speed, it is thought that the partially melted regions, which are in higher-temperature liquid form, cause larger cracks during solidification.

When the SEM images of the weld interface according to various tool rotational speeds were examined, it was observed that with the increase of the tool rotational speed, the porosity in the interface microstructure increased (Figs. 5a, 5b, 5c). It was determined that there were small gaps in the microstructure of the sample joined at 1040 rpm, there were dimples and gaps in the sample joined at 1320 rpm, and there were large gaps in the sample joined at 1500 rpm (Figs. 5d, 5e, 5f). This result is thought to have occurred due to the higher heat input when high tool rotational speed was used. Mahto et al. stated that as a result of low heat input, the porosity and intermetallic compound layer formation decreased. However, it was

https://doi.org/10.26701/ems.1161862

stated that due to the high heat input, aluminium softens more than steel, and that leads to an inhomogeneous mixing process and creates porosity in the welding zone [36].

When the cross sectional micrograph of the sample joined at rotational speed of 1040 rpm were examined (Fig. 6d), cracks and cavity-like weld defects were not observed, and a thin intermetallic layer formation was observed at the interface. Also, the crack line and seperate zone were observed in samples joined at 1320 rpm and 1500 rpm tool rotational speeds, respectively (Fig. 6e-6f). Sun et al. [27] In their study on the joining of Al and mild steel sheets with FSSW, determined that intermetallic layer formation took place at the Al/Fe interface as a result of the high temperature during the welding process. Esmaeili et al. [37], in their study on joining Al and Cu plates with FSW, determined that when low tool rotational speed is used, the intermetallic layer does not form. They also stated that the intermetallic layer formation begins as the tool rotational speed increases and the thickness of the intermetallic layer increases at a higher tool rotational speed. They concluded that the formation of a thin intermetallic layer increases the tensile strength, whereas the thickening of the intermetallic layer decreases the tensile strength. Bozzi et al. [38], in their study on the joining of Al and steel sheets with FSSW, reported that $FeAl_3$, Fe_2Al_5, and $FeAl_2$ intermetallic compounds were formed depending on the welding parameters.

When the results of XRD analysis were examined (Fig.

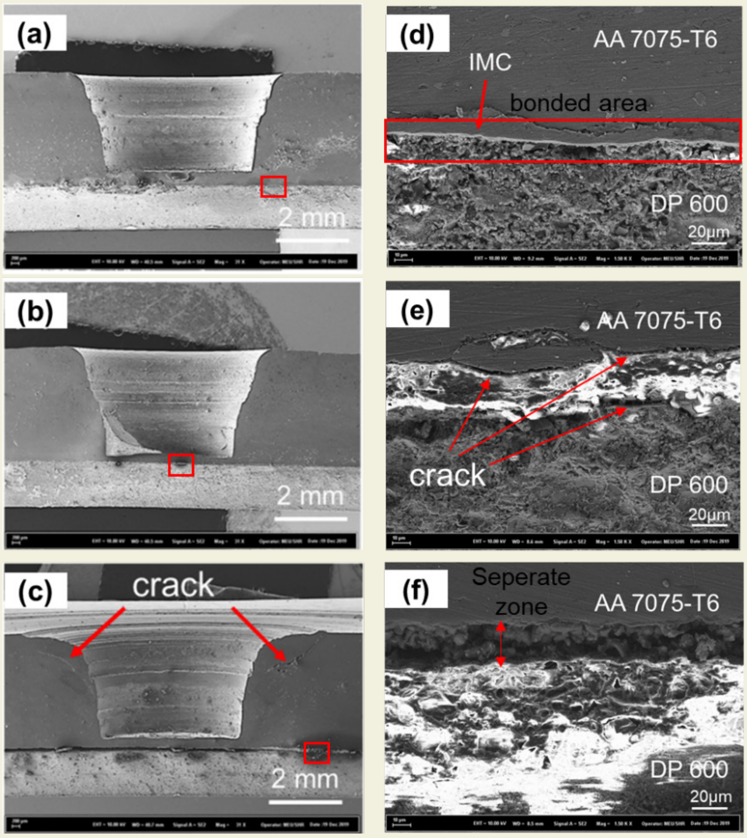

Figure 6. Cross sectional micrograph of samples, (a-d) 1040 rpm, (b-e) 1320 rpm, and (c-f) 1500 rpm.

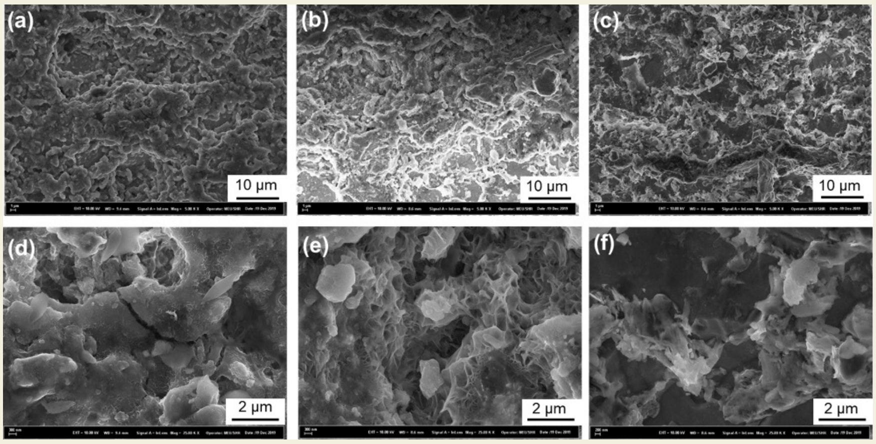

Figure 5. SEM images of weld interface according to various tool rotational speeds, (a-d) 1040 rpm, (b-e) 1320 rpm, and (c-f) 1500 rpm.

7) on the fractured steel sides of the tensile test samples, it was determined that there was mostly an iron phase, in addition to the Al and Zn peaks in the structure, and no apparent intermetallic compound was detected in the sample obtained using 1040 rpm as the tool rotational speed.

When the rotational speed of the tool was chosen as 1320 rpm or 1500 rpm, the presence of peaks similar to those mentioned in the above paragraph was determined. The phases were determined to be mostly Fe and Al, as well as peaks of the $Al_{13}Fe_4$ intermetallic compound.

In studies in the literature on joining pure Al with Zn-coated steel [39], pure Al with low carbon steel [40] and 6063 Al alloy with Zn coated steel [41], it was reported that an $Al_{13}Fe_4$ intermetallic compound was formed. Jiang and Kovacevic [42] reported that Al-Fe intermetallic compounds were formed by reacting with steel as a result of Al melting during the welding process. Lee et al. [43] reported that the first phase that began to nucleate at the Al-Fe interface was the $Al_{13}Fe_4$ phase. As a result of the reaction between $Al_{13}Fe_4$ and Fe, they reported that the Al_5Fe_2 phase occurred, but it was also said that the presence of this structure was not actually detected due to the short dwell time. In the study that we conducted, it was thought that the Al_5Fe_2 phase did not occur due to the joining of the tool without plunging into the steel plate through diffusion. Das et al. [44] reported that the formation of the $Al_{13}Fe_4$ phase increased when a high rotational speed was used, and this was explained by the lower rate of cooling at high rotational speed.

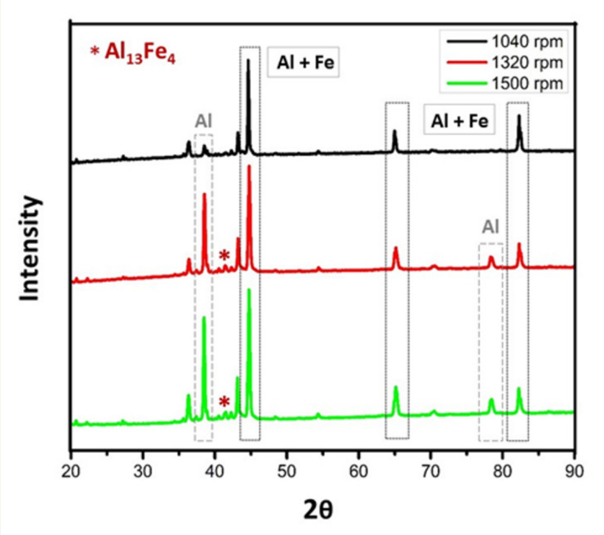

Figure 7. XRD analysis results of shear fracture surface on steel side.

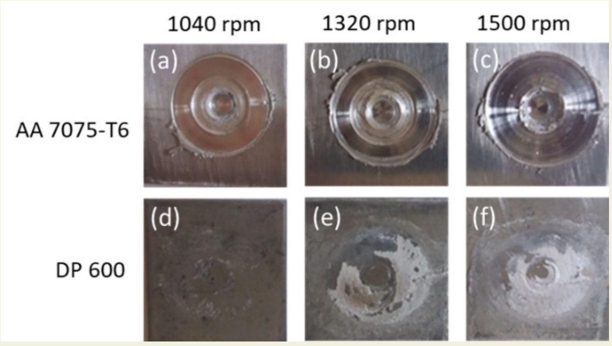

Figure 8. View of stir zones of Al plates (a), (b), (c), and DP600 plates (d), (e), (f) after the tensile test.

3.2. Tensile shear force

Fig. 8 shows the top surfaces of the DP 600/AA7075-T6 joints obtained under various FSSW process parameters. The materials used during the FSSW process were exposed to friction and downward force by the tool. For this reason, the steel material was transported towards the plasticized aluminum material side. Increasing the temperature in the stir zone (SZ) leads to the transfer of more materials from one to the other in the joined samples due to diffusion. When the surface of the Al plates at the top in the welding process was examined, it was determined that a similar appearance formed for various rotational

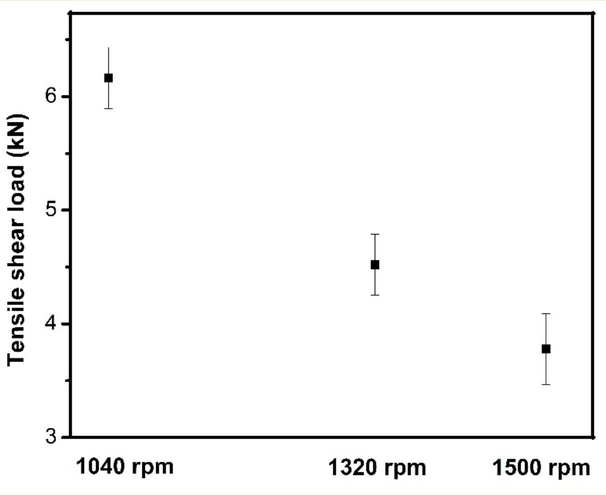

Figure 9. Lap shear fracture load of FSS-welded sheets according to various tool rotational speeds.

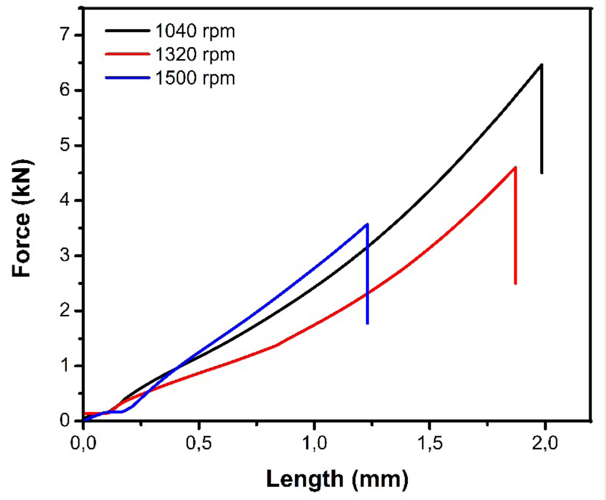

Figure 10. Force-elongation curves of welded joints according to various tool rotational speeds.

speeds (1040, 1320, and 1500 rpm), and, as a result of material transfer, shoulder and pin pits formed.

The fracture load values and force-elongation curves for the welded parts according to various tool rotational speeds are given in Fig. 9 and Fig. 10, respectively. It was determined that there was a decrease in the fracture loads due to the increasing tool rotational speed, and the highest fracture load of 6.5 kN was obtained from the sample joined at the rotational speed of 1040 rpm. The lowest fracture load of 3.5 kN was obtained from the sample joined with rotational speed of 1500 rpm (Fig. 9). The reason for the decrease in the fracture load determined at high tool rotational speed (1500 rpm) is thought to be the fragile intermetallic compounds that formed as a result of increased temperature in the welding zone. Choi et al. [45] reported in their study on the joining of Al and Mg sheets with FSSW that the tensile strength was decreased with the increase of the tool rotational speed. They explained this reduction in tensile strength with the thickness of the layer formed by the reaction and the cracks found.

3.3. Vickers microhardness

Vickers hardness values for each of the joints produced by FSSW at different rotational speeds are given in Fig. 11. The Vickers hardness measurements were carried out on the top plate 1 mm above the overlap line. As seen in Fig. 11, the sample joined with rotational speed of 1040 rpm had lower Vickers hardness values, while the samples joined at 1320 rpm and 1500 rpm showed similar hardness values. This change of hardness values obtained by moving away from the welding centre was similar for various rotational speeds, and with the distance away from the welding centre, the hardness values were first decreased and then increased. It is thought that the decrease in hardness values occurs in the heat-affected zone. Venukumar et al. [46] explained this situation with the coarsening of the grains as a result of excessive aging. A hardness value of approximately 160 HV was obtained for various rotational speeds at the exit hole of the pin. In the heat-affected zone, a hardness value of approximately 140 HV was measured for the sample joined at a rotational speed of 1040 rpm, and similar values for samples joined at rotational speeds of 1320 rpm and 1500 rpm were measured as approximately 150 HV.

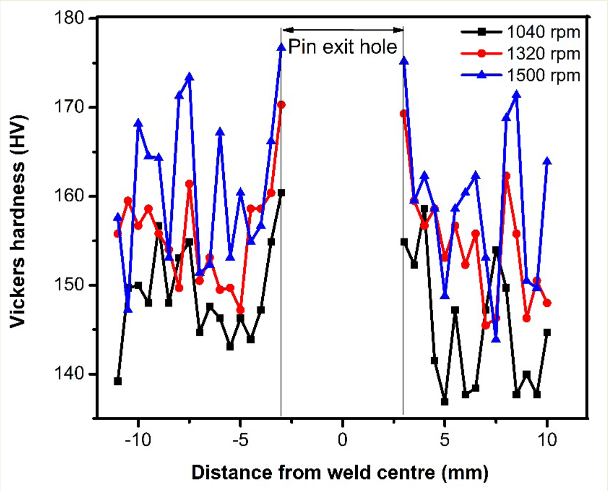

Figure 11. Vickers hardness values of FSW-welded joints using various rotational speeds.

4. Conclusions

In this study, DP600 steel and AA 7075-T6 al alloys were welded by FSSW method. The effects of various tool rotational speeds (1040 rpm, 1320 rpm, 1500 rpm) on joint performance were investigated.

The SEM examinations of the dissimilar spot welds fabricated by FSSW using different rotational speeds revealed that the sample joined using rotational speed of 1040 rpm did not exhibit any obvious cracks while cracking in the welding area of the samples joined at 1320 rpm and 1500 rpm was present. It was also determined that the cracking and porosity increased with increasing tool rotational speed. As a result of the XRD analysis of the fractured steel sides after the tensile testing, it was observed that the parts joined at 1320 rpm and 1500 rpm included the intermetallic Al13Fe4 phase. When the Vickers hardness values of the welded samples were compared, it was observed that the samples joined at 1320 rpm and 1500 rpm had hardness values close to each other, with hardness of approximately 150 HV, and the sample joined at 1040 rpm had the lowest hardness with a hardness value of 140 HV. It was determined that there was a decrease in the tensile shear force due to the increase in the tool rotational speed. The lowest tensile shear force was obtained as 3.5 kN from the sample joined at rotational speed of 1500 rpm. The highest tensile shear force was obtained as 6.5 kN from the sample joined using rotational speed of 1040 rpm.

5. References

[1] Ogura, T., Saito, Y., Nishida, T., Nishida, H., Yoshida, T., Omichi, N., Fujimoto, M., Hirose, A., (2012). Partitioning evaluation of mechanical properties and the interfacial microstructure in a friction stir welded aluminum alloy/stainless steel lap joint, Scripta Materialia. 66(8): 531–534. https://doi.org/10.1016/j.scriptamat.2011.12.035.

[2] Ogura, T., Nishida, T., Tanaka, Y., Nishida, H., Yoshikawa, S., Fujimoto, M., Hirose, A., (2013). Microscale evaluation of mechanical properties of friction stir welded A6061 aluminium alloy / 304 stainless steel dissimilar lap joint, Science and Technology of Welding and Joining. 18(2): 108–113. https://doi.org/10.1179/1362171812Y.0000000098.

[3] Doruk, E., Pakdil, M., Çam, G., Durgun, İ., Kumru, U. C., (2016). Resistance spot welding applications in automotive industry. Engineer and Machinery, 57(673): 48-53.

[4] Zhang, W., Sun, D., Han, L., Gao, W., Qiu, X., (2011). Characterization of intermetallic compounds in dissimilar material resistance spot welded joint of high strength steel and aluminum alloy. The Iron and Steel Institute of Japan. 51(11):

1870–1877. https://doi.org/10.2355/isijinternational.51.1870.

[5] Cakan, A., Atmaca, H., Ugurlu, M., (2018). Analysis and joining of Al – Cu plates using friction stir welding technique. European Mechanical Science. 2(1): 1–8. https://doi.org/10.26701/ems.358729.

[6] Cakan, A., Ugurlu, M., Kaygusuz, E., (2019). Effect of weld parameters on the microstructure and mechanical properties of dissimilar friction stir joints between pure copper and the aluminum alloy AA7075-T6. Materials Testing. 61(2): 142–148. https://doi.org/10.3139/120.111297.

[7] Ugurlu, M., Cakan, A., (2019). The effect of tool rotation speed on mechanical properties of friction stir spot welded (FSSW) AA7075-T6 aluminium alloy. European Mechanical Science. 3: 97–101. https://doi.org/10.26701/ems.520139.

[8] Çam, G., Javaheri, V., Heidarzadeh, A. (2022). Advances in FSW and FSSW of dissimilar Al-alloy plates. Journal of Adhesion Science and Technology, 1-33. https://doi.org/10.1080/01694243.2022.2028073.

[9] Çam, G., (2011). Friction stir welded structural materials: beyond Al-alloys. International Materials Reviews, 56(1): 1-48. https://doi: 10.1179/095066010X12777205875750 10.

[10] Çam, G., İpekoğlu, G., (2017). Recent developments in joining of aluminum alloys. The International Journal of Advanced Manufacturing Technology, 91(5): 1851-1866. https://doi.org/10.1007/s00170-016-9861-0. 11

[11] Çam, G., İpekoğlu, G., Tarık Serindağ, H., (2014). Effects of use of higher strength interlayer and external cooling on properties of friction stir welded AA6061-T6 joints. Science and Technology of Welding and Joining, 19(8): 715-720. https://doi.org/10.1179/1362171814Y.0000000247.

[12] Çam, G., Mistikoglu, S., Pakdil, M., (2009). Microstructural and mechanical characterization of friction stir butt joint welded 63% Cu-37% Zn brass plate. Welding Journal, 88(11): 225-232.

[13] Küçükömeroğlu, T., Aktarer, S. M., Çam, G., (2019). Investigation of mechanical and microstructural properties of friction stir welded dual phase (DP) steel. In IOP Conference Series: Materials Science and Engineering. 629(1): 012010. https://doi.org/10.1088/1757-899X/629/1/012010.

[14] Küçükömeroğlu, T., Aktarer, S. M., İpekoğlu, G., Çam, G., (2018). Mechanical properties of friction stir welded St 37 and St 44 steel joints. Materials Testing. 60(12): 1163-1170. https://doi.org/10.3139/120.111266.

[15] İpekoğlu, G., Erim, S., Kıral, B. G., Çam, G., (2013). Investigation into the effect of temper condition on friction stir weldability of AA6061 Al-alloy plates. Kovove Materialy, 51(3): 155-163. https://doi.org/10.4149/km-2013-3-155. 16.

[16] İpekoğlu, G., Çam, G., (2014). Effects of initial temper condition and postweld heat treatment on the properties of dissimilar friction-stir-welded joints between AA7075 and AA6061 aluminum alloys. Metallurgical and Materials Transactions A, 45(7): 3074-3087.

[17] İpekoglu, G., Çam, G., (2012). The effect of temper condition on friction stir welding of dissimilar Al-alloys (AA6061/AA7075) plates. Engineer and Machinery, 53(629): 40-47.

[18] İpekoğlu, G., Gören Kıral, B., Erim, S., Çam, G., (2012). Investigation of the effect of temper condition on friction stir weldability of AA7075 Al-alloy plates. Materials Technology, 46(6): 627-632. https://doi.org/669.715:621.791:620.17.

[19] Çam, G., (2005). Friction stir welding: A novel welding technique developed for Al-alloys. Engineer and Machinery. 46(541): 30-39.

[20] Cam, G., Gucluer, S., Cakan, A., Serindag, H.T., (2009). Mechanical properties of friction stir butt-welded Al-5086 H32 plate, Materwissenschaft und Werkstofftechnik: Entwicklung, Fertigung, Prüfüng, Eigenschaften und Anwendungen Technischer Werkstoffe. 40: 638–642. https://doi.org/10.1002/mawe.200800455.

[21] Mahto, R.P., Kumar, R., Pal, S.K., (2020). Characterizations of weld defects, intermetallic compounds and mechanical properties of friction stir lap welded dissimilar alloys, Materials Characterization. 160: 110115. https://doi.org/10.1016/j.matchar.2019.110115.

[22] Schneider, J., Radzilowski, R., (2014). Welding of very dissimilar materials (Fe-Al), Jom. 66(10): 2123–2129. https://doi.org/10.1007/s11837-014-1134-5.

[23] Bozkurt, Y., Salman, S., Çam, G., (2013). Effect of welding parameters on lap shear tensile properties of dissimilar friction stir spot welded AA 5754-H22/2024-T3 joints. Science and Technology of Welding and Joining. 18(4): 337-345. https://doi.org/10.1179/1362171813Y-0000000111.

[24] Ibrahim, H.K., Khuder, A.W.H., Muhammed, M.A.S., (2019). Effect of tool-pin geometry on microstructure and temperature distribution in friction stir spot welds of similar AA2024-T3 aluminum alloys. International Journal of Mechanical and Mechatronics Engineering. 19: 14–28.

[25] Shen, Z., Ding, Y., Gerlich, A.P., (2019). Advances in friction stir spot welding, Critical Reviews in Solid State Materials Sciences. 8436. https://doi.org/10.1080/10408436.2019.1671799.

[26] Li, M., Zhang, C., Wang, D., Zhou, L., Wellmann, D., Tian, Y., (2020). Friction stir spot welding of aluminum and copper: A review, Materials. 13(1): 156. https://doi.org/10.3390/ma13010156.

[27] Sun, Y.F., Fujii, H., Takaki, N., Okitsu, Y., (2013). Microstructure and mechanical properties of dissimilar Al alloy/steel joints prepared by a flat spot friction stir welding technique. Materials and Design. 47: 350–357. https://doi.org/10.1016/j.matdes.2012.12.007.

[28] Piccini, J.M., Svoboda, H.G., (2017). Tool geometry optimization in friction stir spot welding of Al-steel joints. Journal of Manufacturing Processes. 26: 142–154. https://doi.org/10.1016/j.jmapro.2017.02.004.

[29] Sun, Y., Fujii, H., Zhu, S., Guan, S., (2019). Flat friction stir spot welding of three 6061-T6 aluminum sheets. Journal of Materials Processing Technology. 264: 414–421. https://doi.org/10.1016/j.jmatprotec.2018.09.031.

[30] Wang, T., Sidhar, H., Mishra, R.S., Hovanski, Y., Upadhyah, P., Carlson, B., (2019). Evaluation of intermetallic compound layer at aluminum steel interface joined by friction stir scribe technology. Materials and Design. 174: 1–6. https://doi.org/10.1016/j.matdes.2019.107795.

[31] Hsieh, M.J., Lee, R.T., Chiou, Y.C., (2017). Friction stir spot fusion welding of low carbon steel to aluminium alloy. Journal of Materials Processing Technology. 240: 118–125. https://doi.org/10.1016/j.jmatprotec.2016.08.034.

[32] Haghshenas, M., Abdel-Gwad, A., Omran, A.M., Gokce, B., Sahraeinejad, S., Gerlich, A.P., (2014). Friction stir weld assisted diffusion bonding of 5754 aluminum alloy to coated high

strength steels. Materials and Design. 55: 442–449. https://doi.org/10.1016/j.matdes.2013.10.013.

[33] Fereiduni, E., Movahedi, M., Kokabi, A.H., (2015). Aluminum/steel joints made by an alternative friction stir spot welding process. Journal of Materials Processing Technology. 224: 1–10. https://doi.org/10.1016/j.jmatprotec.2015.04.028.

[34] Su, P., Gerlich, A., North, T.H., Bendzsak, G.J., (2007). Intermixing in dissimilar friction stir spot welds. Metallurgical and Materials Transactions A. 38: 584–595. https://doi.org/10.1007/s11661-006-9067-4.

[35] Yamamoto, M., Gerlich, A., North, T.H., Shinozaki, K., (2008). Cracking in dissimilar Mg alloy friction stir spot welds. Science and Technology of Welding and Joining. 13(7): 583–592. https://doi.org/10.1179/174329308X349520.

[36] Mahto, R.P., Gupta, C., Kinjawadekar, M., Meena, A., Pal, S.K., (2019). Weldability of AA6061-T6 and AISI 304 by underwater friction stir welding. Journal of Manufacturing Processes. 38: 370–386. https://doi.org/10.1016/j.jmapro.2019.01.028.

[37] Esmaeili, A., Zareie Rajani, H.R., Sharbati, M., Givi, M.K.B., Shamanian, M., (2011). The role of rotation speed on intermetallic compounds formation and mechanical behavior of friction stir welded brass/aluminum 1050 couple. Intermetallics. 19(11): 1711–1719. https://doi.org/10.1016/j.intermet.2011.07.006.

[38] Bozzi, S., Helbert-Etter, A.L., Baudin, T., Criqui, B., Kerbiguet, J.G., (2010). Intermetallic compounds in Al 6016/IF-steel friction stir spot welds. Materials Science and Engineering: A. 527(16-17): 4505–4509. https://doi.org/10.1016/j.msea.2010.03.097.

[39] Ahmed, E., Makoto, T., Kenji, I., (2005). Friction stir welded lap joint of aluminum to zinc coated steel. Quarterly Journal of the Japan Welding Society. 23(2): 186–193. https://doi.org/10.2207/qjjws.23.186.

[40] Elrefaey, A., Gouda, M., Takahashi, M., Ikeuchi, K., (2005). Characterization of aluminum/steel lap joint by friction stir welding. Journal of Materials Engineering and Performance. 14(1): 10–17. https://doi.org/10.1361/10599490522310.

[41] Das, H., Basak, S., Das, G., Pal, T.K., (2013). Influence of energy induced from processing parameters on the mechanical properties of friction stir welded lap joint of aluminum to coated steel sheet. The International Journal of Advanced Manufacturing Technology. 64(9): 1653–1661. https://doi.org/10.1007/s00170-012-4130-3.

[42] Jiang, W.H., Kovacevic, R., (2004). Feasibility study of friction stir welding of 6061-T6 aluminium alloy with AISI 1018 steel. Proceedings of the Institution of Mechanical Engineers, Part B: Journal of Engineering Manufacture. 218(10): 1323–1331. https://doi.org/10.1243/0954405042323612.

[43] Lee, I.S., Kao, P.W., Ho, N.J., (2008). Microstructure and mechanical properties of Al–Fe in situ nanocomposite produced by friction stir processing. Intermetallics. 16(9): 1104–1108. https://doi.org/10.1016/j.intermet.2008.06.017.

[44] Das, H., Jana, S.S., Pal, T.K., De, A., (2014). Numerical and experimental investigation on friction stir lap welding of aluminium to steel. Science and Technology of Welding and Joining. 19(1): 69–75. https://doi.org/10.1179/1362171813Y.0000000166.

[45] Choi, D.H., Ahn, B.W., Lee, C.Y., Yeon, Y.M., Song, K., Jung, S.B., (2011). Formation of intermetallic compounds in Al and Mg alloy interface during friction stir spot welding, Intermetallics. 19(2): 125–130. https://doi.org/10.1016/j.intermet.2010.08.030.

[46] Venukumar, S., Yalagi, S., Muthukumaran, S., (2013). Comparison of microstructure and mechanical properties of conventional and refilled friction stir spot welds in AA 6061-T6 using filler plate. Transactions of Nonferrous Metals Society of China. 23(10): 2833–2842. https://doi.org/10.1016/S1003-6326(13)62804-6.

EUROPEAN MECHANICAL SCIENCE
e-ISSN: 2587-1110

RESEARCH ARTICLE

Optimization of Friction Stir Welded Dissimilar Aluminum Alloys EN AW-5083-H111 and EN AW-6082-T651 using Hybrid Taguchi-Based Grey Relation Analysis

Uğur Eşme[1*], Şeref Öcalır[2], Mustafa Kemal Külekci[3]

[1]Tarsus University Engineering Faculty Department of Mechanical Engineering, Mersin-Tarsus
[2]Tarsus University Organized Industrial Zone Vocational School Machine Program, Mersin-Tarsus
[3]Tarsus University Engineering Faculty Department of Mechanical Engineering, Mersin-Tarsus

Orcid: U. Eşme(0000-0002-0672-7943), Ş. Öcalır (0000-0003-0123-2295), M.K. Külekci (0000-0002-5829-3489)

Abstract: Friction Stir Welding (FSW) which is a kind of solid state welding process used essentially for joining nonferrous metals and their alloys. Involving pollution free and no filler material are the advantages of FSW when compared to other welding methods. The present work was focused on the multi objective optimization of friction stir welded EN AW-6082-T651 and EN AW-5083-H111 aluminum alloys using Taguchi based Grey relational analysis (GRA) method under different parameters of shoulder diameter (SD, mm), tool rotation (TR, rpm) and welding speed (WS, mm/min) on tensile strength (TS, MPa), percent elongation (E, %) and joint efficiency (JE). Taguchi related experiments were performed using L_{27} Orthogonal Array. The grey relational analysis which relates between the FSW parameters and the responses applied to find the optimum condition. Additionally, the Analysis of Variance (ANOVA) approach was used to identify the most important factor and its impact on the multiple response. The results of the obtained tests were then verified using the confirmation test.

Keywords: Taguchi method, Grey relation analysis, Friction stir welding, Optimization, Tensile strength

1. Introduction

Friction stir welding (FSW) which was developed and patented in 1991 by TWI (The Welding Institute) in England is a new technology of solid state welding method for joining of similar and dissimilar metals [1,2]. The FSW technique is accomplished by rotating and advancing a tool made up of a pin and shoulder with a unique profile across the surface of the material to be connected. Surface friction and heat are produced as a result of the tool pin's pressure and rotating movement. This results a heat and softens the material locally and plastic deformation occurs on the area to be welded [2-4]. The welding procedure is carried out by the tool's advanced movement along the predetermined bond line [5-7]. The demonstration for the FSW process is given in Figure 1.

Where combining different metals and alloys that call for excellent performance, particularly when distortions and internal stresses are not sought, FSW is effectively used as a cold welding procedure [8-10]. The FSW process, which is used for creating high quality welds in a number of materials difficult to weld by conventional welding processes, finds application field such as ship and marine industry, aviation and space industry and land transport and railway industries [1,7,8]. There are numerous studies deals with modeling and optimization of friction stir welding using different kind of workpiece materials.

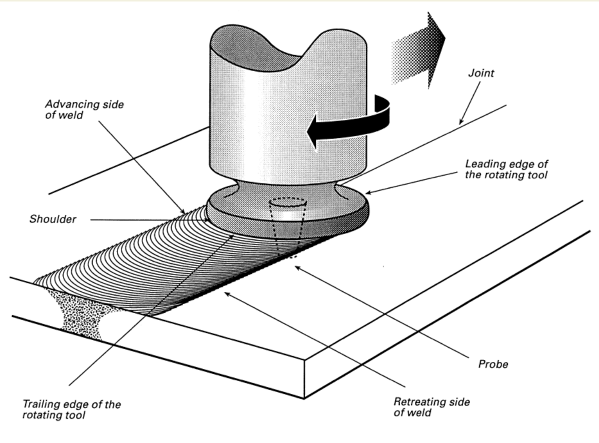

Figure 1. Schematic representation of FSW process [7]

---

[*] Corresponding author.
Email: esme@tarsus.edu.tr

European Mechanical Science (2022), 6(4): 241-250
https://doi.org/10.26701/ems.1187999
Received: October 12, 2022 — Accepted: November 01, 2022

Kumar et al. [11] presented hybrid fuzzy assisted grey Taguchi method for optimization of friction stir welded Al/Cu joints. Sun et al. [12] studied the influence of friction stir welding on mechanical properties of AZ61 magnesium alloy. Shanik et al. [13] investigated multi response optimization in friction stir welding of aluminum alloy using grey relational analysis. Pratash et al. [14] presented a study for multiple response Taguchi based grey relation analysis for optimization of magnesium alloy. Palani et al. [15] examined friction stir welding aluminum alloy using grey relation optimization method. Vijayan et al. [16] optimized AA5083 aluminum alloy using Taguchi based grey optimization method. Gupta et al. [17] presented genetic algorithm based optimization study for friction stir welded AA5083 and AA6063-T6 aluminum alloys. Babu et al. [18] optimized friction stir welding process using artificial neural network with genetic algorithm. Yunus et al. [19] modelled friction stir welding process of two dissimilar aluminum alloys using experimental design technique and genetic algorithm. Yousif et al. [20] developed an artificial neural network model for prediction of mechanical properties of friction stir welded aluminum alloy.

Taguchi's method is developed by Dr. Genichi Taguchi in 1950s who is a Japanese quality management advisor. Design of the experiments through orthogonal array using Taguchi's philosophy is an effective way to optimize the design, cost and quality with a minimum number of trials [21]. In the Taguchi method, optimum parameter combination is selected by using a statistical measurement of efficiency which is named as signal to noise ratio (S/N). The S/N rate is related to the ratio of mean to the standard deviation. This ratio is affected by optimized quality characteristics of the process [21,22]. Taguchi uses three types of quality characteristics of nominal the better (NB), lower the Better (LB) and higher the better (HB). The optimal parameter setting requires the highest S/N ratio [21].

In the present work, Taguchi based grey relational analysis (GRA) has been carried out for the multi response optimization of FSW process parameters such as shoulder diameter (SD, mm), tool rotation (TR, rpm) and welding speed (WS, mm/min) on the responses of tensile strength (TS, MPa), percent elongation (E, %) and joint efficiency (JE) during welding of dissimilar aluminum alloys of EN AW-5083-H111 and EN AW-6082-T651. So, an optimal FSW process parameters were determined through this method. Finally, the analysis of variance (ANOVA) was applied in order to examine the contribution of each FSW parameters on the responses.

2. Grey Relational Analysis

The Grey system theory, first put forward by Deng in 1989, is a system in which some of the information is known and some is unknown. In other words, grey system indicates the level of information between black and white. Although, black region does not have any information, the white region has the information completely. Grey modeling includes the subtitle "grey relation analysis" (GRA). To ascertain the degree of the link between the components, each component of the system was compared to a reference sequence [21].

2.1. Normalization of the Responses

The first step which is considering the conversion of the measured values come from different units is called as normalization. The criteria of "smaller is better," "larger is better," and "ideal is better" are used to make normalization of the experimental data between zero and one. In normalization calculation of this work, tensile strength (TS), joint efficiency (JE), and the normalized reference sequences were calculated using the "larger is better" (LB) criteria. Following formula expresses the larger the better criterion [21]:

$$x_i(k) = \frac{y_i(k) - min\, y_i(k)}{max\, y_i(k) - min\, y_i(k)} \tag{1}$$

Percent elongation (E) should follow the *smaller the better* (SB) criterion which is expressed as:

$$x_i(k) = \frac{max\, y_i(k) - y_i(k)}{max\, y_i(k) - min\, y_i(k)} \tag{2}$$

where $x_i(k)$ is calculated after the Grey relation generation, min$y_i(k)$ is the lowest value of $y_i(k)$ related to the k^{th} response, and max$y_i(k)$ is the highest value of $y_i(k)$ $y_i(k)$ related to the k^{th} response. A reference sequence is $x_0(k)$ (k=1, 2, 3......, 27) for the responses. The definition of the Grey relational degree in the process of GRG analysis is to show the degree of the connection between 27 sequences [$x_0(k)$ and $x_i(k)$, i=1, 2, 3.......,27].

2.2. Calculation of Grey Relational Coefficient

Normalization step should follow the calculation of grey relational coefficient (GRC) to determine the relation between the best and actual normalized responses. The Grey relational coefficient (GRC) $\xi_i(k)$ is calculated as [21]:

$$\xi_i(k) = \frac{\Delta_{\min} + \psi\Delta_{\max}}{\Delta_{0i}(k) + \psi\Delta_{\max}} \tag{3}$$

where $\Delta_{0i} = \|x_0(k) - x_i(k)\|$= difference of the absolute value $x_0(k)$ and $x_i(k)$; ψ is the distinguishing coefficient $0 \leq \psi \leq 1$, $\psi$is considered as 0.333 for each responses; $\Delta min^{min\|x_0(k)-x_j(k)\|}{}_{min}$=the smallest value of Δ_{0i}; and $\Delta max^{max\|x_0(k)-x_j(k)\|}{}_{max}$= highest value of Δ_{0i}.

2.3. Grey Relational Grade Calculations

The Grey relational grade (GRG) γ_i for each response of the FSW process is determined by averaging the Grey relational coefficients and is computed as follows [21]:

$$\gamma_i = \frac{1}{n}\sum_{k=1}^{n} \xi_i(k) \tag{4}$$

(a)

(b)

(c)

Figure 2. (a) Milling machine used in the FSW experiments, (b) Fixture and components, (c) Welding tool geometry

Table 1. Chemical (wt.%) and mechanical characteristics of the workpieces [23,24]

EN AW-5083-H111							
Chemical composition (wt.%)	Fe%	Cr	Mg%	Mn%	Cu%	Si%	Al%
	0.40	max 0.25	4.50	0.60	max 0.10	0.40	Balance
Mechanical properties	Tensile strength (MPa)		Yield strength (MPa)		% Elongation		Hardness (HV$_{0.2}$)
	310		170		17		92.46
EN AW-6082-T651							
Chemical composition (wt.%)	Fe%	Cr	Mg%	Mn%	Cu%	Si%	Al%
	0.50	max 0.25	1.20	0.80	max 0.10	0.80	Balance
Mechanical properties	Tensile strength (MPa)		Yield strength (MPa)		% Elongation		Hardness (HV$_{0.2}$)
	330		270		16		123.30

where n is the number of the friction stir welding responses. The higher value of GRG means that there is a stronger relational degree between the reference sequence $x_0(k)$ and the given sequence$x_i(k)$. The reference sequence $x_0(k)$ represents the best process sequence; hence, higher Grey relational grade indicates that obtained parameter combination is very close to the optimal value. Both, the average response for the GRG and the main effect graph of GRG are very important for the evaluation of optimal welding process condition [21,22].

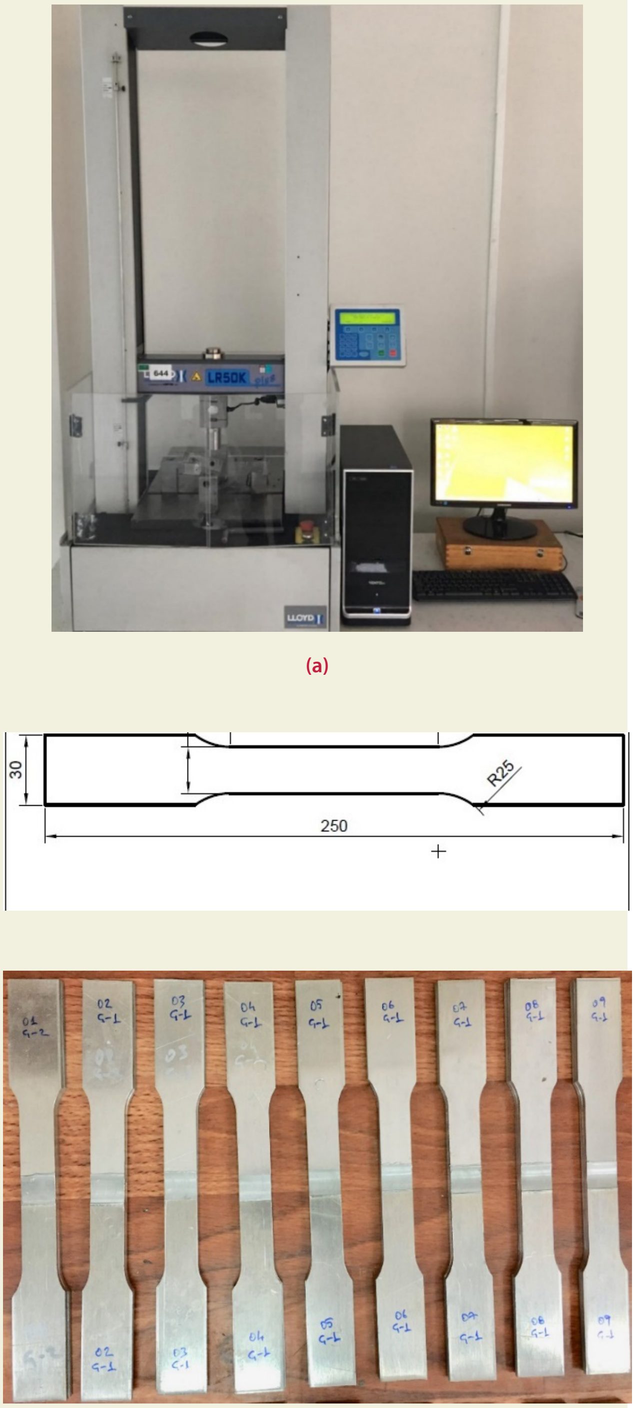

(a)

(b)

Figure 3. (a) Tensile testing equipment, (b) Prepared samples according to EN ISO 6892-1

3. Experimental Methodology and Test Results

3.1. Experimental Details

The aluminum alloys of EN AW-5083-H111 and EN AW-6082-T651 were used in this investigation with the dimensions of 125 mm x 400 mm x 4 mm and used for butt joint form using FSW process [1]. Table 1 provides the chemical composition (wt.%) and mechanical characteristics of the workpiece material.

The experiments were performed on the semi-automatic vertical milling machine. Hot work tool (H13) steel, due of its excellent wear resistance, hardness at elevated temperatures, and ease of availability, was employed as the friction welding tool [1]. Used tool pin profile was M5 screw type with a 3.8 mm pin length. Figure 2 also displays the experimental details, such as fixtures and experimental components, the pin profile and shape.

As shown in Figure 3, the tensile test specimens were cut perpendicular to the direction of welding, and then machined as per EN ISO 6892-1 standards and which were tested in the LLOYD Instruments tensile testing machine.

3.2. Experimental Details and Test Results

Taguchi experimental design offers an opportunity for designing and conducting the experiments using minimum resources. Throughout this work, the L_{27} orthogonal array which consists of 27 sets of data was utilized to set the parameters for friction stir welding. Table 2 shows the input parameters and their levels.

The experiments were conducted in accordance with the Taguchi's L_{27} orthogonal array assigning different levels values to the FSW parameters and the final results for tensile strength (TS), percent elongation (E) and joint efficiency (JE) is tabulated in Table 3. All of these L_{27} array data have been used in a grey relation analysis to identify the best FSW parameter combinations for the desired weld quality in the experimental setting.

4. Fsw Parameter Optimization Using Grey Relation Method

4.1. Finding the Optimum FSW Parameter

Prior to creating the grey relation generation (GRG), ob-

Table 2. FSW parameters and their limits

Welding parameters	Notation	Unit	Levels of parameters 1	2	3
Shoulder diameter	SD	mm	16	20	24
Tool rotation	TR	rpm	710	1000	1400
Welding speed	WS	mm/min	56	112	160

Table 3. Experimental and calculated results

Experimental run	Process parameters			Results			Fracture zones HAZ: heat affected zone WZ: weld zone
	SD	TR	WS	TS (MPa)	E (%)	JE	
1	1	1	1	209.43	3.81	67.56	EN AW-6082 HAZ
2	1	1	2	219.73	4.97	70.88	WZ
3	1	1	3	223.49	4.61	72.09	WZ
4	1	2	1	159.55	2.28	51.47	WZ
5	1	2	2	213.18	3.76	68.77	WZ
6	1	2	3	230.43	5.44	74.33	EN AW-6082 HAZ
7	1	3	1	207.04	4.12	66.79	EN AW-6082 HAZ
8	1	3	2	212.53	4.33	68.56	EN AW-6082 HAZ
9	1	3	3	228.92	5.24	73.85	EN AW-6082 HAZ
10	2	1	1	201.11	4.06	64.87	EN AW-6082 HAZ
11	2	1	2	209.36	4.47	67.54	EN AW-6082 HAZ
12	2	1	3	217.13	4.82	70.04	EN AW-6082 HAZ
13	2	2	1	200.30	4.02	64.61	EN AW-6082 HAZ
14	2	2	2	206.92	4.24	66.75	EN AW-6082 HAZ
15	2	2	3	220.81	4.95	71.23	EN AW-6082 HAZ
16	2	3	1	193.62	4.38	62.46	EN AW-6082 HAZ
17	2	3	2	212.63	5.02	68.59	EN AW-6082 HAZ
18	2	3	3	221.05	4.92	71.31	EN AW-6082 HAZ
19	3	1	1	196.43	4.19	63.36	EN AW-6082 HAZ
20	3	1	2	200.96	4.29	64.83	EN AW-6082 HAZ
21	3	1	3	213.98	4.49	69.03	EN AW-6082 HAZ
22	3	2	1	206.65	4.58	66.66	EN AW-6082 HAZ
23	3	2	2	211.05	4.84	68.08	EN AW-6082 HAZ
24	3	2	3	225.81	5.23	72.84	EN AW-6082 HAZ
25	3	3	1	200.58	4.17	64.70	EN AW-6082 HAZ
26	3	3	2	207.80	4.28	67.03	EN AW-6082 HAZ
27	3	3	3	214.76	4.93	69.28	EN AW-6082 HAZ

Table 4. Tabulation of normalization results and Δ_{0i} for TS, E, and JE

Run	Grey relation generation			Δ_{0i}		
	TS	E	JE	TS	E	JE
Reference sequence	1.000	1.000	1.000	1.000	1.000	1.000
1	0.704	0.516	0.704	0.296	0.484	0.296
2	0.849	0.149	0.849	0.151	0.851	0.151
3	0.902	0.263	0.902	0.098	0.737	0.098
4	0.000	1.000	0.000	1.000	0.000	1.000
5	0.757	0.532	0.757	0.243	0.468	0.243
6	1.000	0.000	1.000	0.000	1.000	0.000
7	0.670	0.418	0.670	0.330	0.582	0.330
8	0.747	0.351	0.748	0.253	0.649	0.252
9	0.979	0.063	0.979	0.021	0.937	0.021
10	0.586	0.437	0.586	0.414	0.563	0.414
11	0.703	0.307	0.703	0.297	0.693	0.297
12	0.812	0.196	0.812	0.188	0.804	0.188
13	0.575	0.449	0.575	0.425	0.551	0.425
14	0.668	0.380	0.668	0.332	0.620	0.332
15	0.864	0.155	0.864	0.136	0.845	0.136
16	0.481	0.335	0.481	0.519	0.665	0.519
17	0.749	0.133	0.749	0.251	0.867	0.251
18	0.868	0.165	0.868	0.132	0.835	0.132
19	0.520	0.396	0.520	0.480	0.604	0.480
20	0.584	0.364	0.584	0.416	0.636	0.416
21	0.768	0.301	0.768	0.232	0.699	0.232
22	0.665	0.272	0.664	0.335	0.728	0.336
23	0.727	0.190	0.727	0.273	0.810	0.273
24	0.935	0.066	0.935	0.065	0.934	0.065
25	0.579	0.402	0.579	0.421	0.598	0.421
26	0.681	0.367	0.681	0.319	0.633	0.319
27	0.779	0.161	0.779	0.221	0.839	0.221

Table 5. Calculated GRC and GRG in accordance with the order

Experimental run	GRC ($\xi_i(k)$) TS	E	JE	GRG	Rank
1	0.527	0.405	0.527	0.4859	14
2	0.686	0.279	0.686	0.5500	7
3	0.771	0.309	0.771	0.6165	4
4	0.248	1.000	0.248	0.4982	10
5	0.576	0.413	0.576	0.5210	9
6	1.000	0.248	1.000	0.7486	1
7	0.500	0.362	0.500	0.4535	18
8	0.566	0.337	0.567	0.4896	13
9	0.939	0.261	0.940	0.7126	2
10	0.444	0.369	0.444	0.4185	22
11	0.526	0.323	0.526	0.4579	17
12	0.638	0.291	0.637	0.5215	8
13	0.437	0.375	0.437	0.4158	23
14	0.499	0.347	0.499	0.4478	20
15	0.709	0.281	0.709	0.5655	6
16	0.389	0.332	0.389	0.3693	27
17	0.568	0.276	0.568	0.4700	15
18	0.714	0.283	0.714	0.5698	5
19	0.408	0.353	0.407	0.3890	26
20	0.442	0.342	0.443	0.4085	25
21	0.587	0.321	0.587	0.4978	11
22	0.496	0.312	0.496	0.4341	21
23	0.547	0.289	0.547	0.4606	16
24	0.835	0.261	0.835	0.6431	3
25	0.439	0.356	0.439	0.4110	24
26	0.508	0.343	0.508	0.4526	19
27	0.599	0.282	0.599	0.4929	12

Table 6. Calculated GRG and its S/N ratios

Experimental run	GRG	S/N
1	0.4859	-6.27
2	0.5500	-5.19
3	0.6165	-4.20
4	0.4982	-6.05
5	0.5210	-5.66
6	0.7486	-2.52
7	0.4535	-6.87
8	0.4896	-6.20
9	0.7126	-2.94
10	0.4185	-7.57
11	0.4579	-6.78
12	0.5215	-5.65
13	0.4158	-7.62
14	0.4478	-6.98
15	0.5655	-4.95
16	0.3693	-8.65
17	0.4700	-6.56
18	0.5698	-4.89
19	0.3890	-8.20
20	0.4085	-7.78
21	0.4978	-6.06
22	0.4341	-7.25
23	0.4606	-6.73
24	0.6431	-3.83
25	0.4110	-7.72
26	0.4526	-6.89
27	0.4929	-6.14

served and computed data were first adjusted using Equations (1) and (2). For each of the replies, the normalized data and the difference in the absolute value (Δ_{0i}) have been computed and are shown in Table 4.

Generally, the distinguishing coefficient (ψ) takes the value between 0 and 1. A survey of the literature reveals that the grey relational grade is unaffected by the distinguishing factor [3]. Throughout this work, each response is given an identical weight of 0.333. Namely, $\psi_{TS} = \psi_E = \psi_{JE} = 0.333$. Table 5 shows the calculated Grey relational coefficients (GRC) for each response corresponding grey relational grade (GRG) calculated by using Eqs. (3) and (4).

The time has come to employ Eq. (7) to calculate the S/N ratio using the larger is better formula for total GRG [21].

$$S/N = -10\log\left[\frac{1}{n}\sum_{i=1}^{n}\frac{1}{y_i^{2}}\right] \tag{7}$$

where n is the number of tests, and y_i is the experimental value i^{th} performance in the j^{th} experiment at the k^{th} test. The computed GRG and its S/N ratio are shown in Table 6.

The highest GRG and S/N mean that within the experimental domain, the chosen parameter setting is extremely near the ideal value [21]. Throughout this work, maximum GRG and corresponding S/N ratios of 0.748 and

-2.52 respectively were obtained at the 6th experimental run for the FSW parameter combination of $SD_1TR_2WS_3$. S/N ratio and GRG graphs plotted vs parameter level are shown in Figure 4. Here, dashed line implies the average of the GRG and S/N ratio.

As indicated in Figure 4, the optimal FSW parameter level combination for EN AW-5083-H111 and EN AW-6082-T651 aluminum alloys obtained as $SD_1TR_2WS_3$ (shoulder diameter of level 1, tool rotation of level 2 and welding speed of level 3). Table 7 lists the corresponding averages of the GRG and S/N ratio for input parameters of the FSW.

Additionally, the method of Analysis of Variance (ANOVA) approach was used on GRG to determine the percent contribution and most important parameter which affects the selected responses. Therefore, in forthcoming section of this work ANOVA is tabulated and discussed.

Table 7. Mean GRG and S/N response table

Factors	**Mean GRG**				
	Level I	**Level 2**	**Level 3**	**max-min**	**Rank**
SD	0.56	0.46	0.47	0.10	1
TR	0.48	0.53	0.49	0.05	2
WS	0.43	0.47	0.60	0.17	3
Total average GRG= 0.50					
Factors	S/N				
	Level I	Level 2	Level 3	max-min	Rank
SD	-5.10	-6.63	-6.73	1.63	1
TR	-6.41	-5.73	-6.32	0.68	2
WS	-7.36	-6.53	-4.58	2.78	3
Total mean S/N= -6.20					

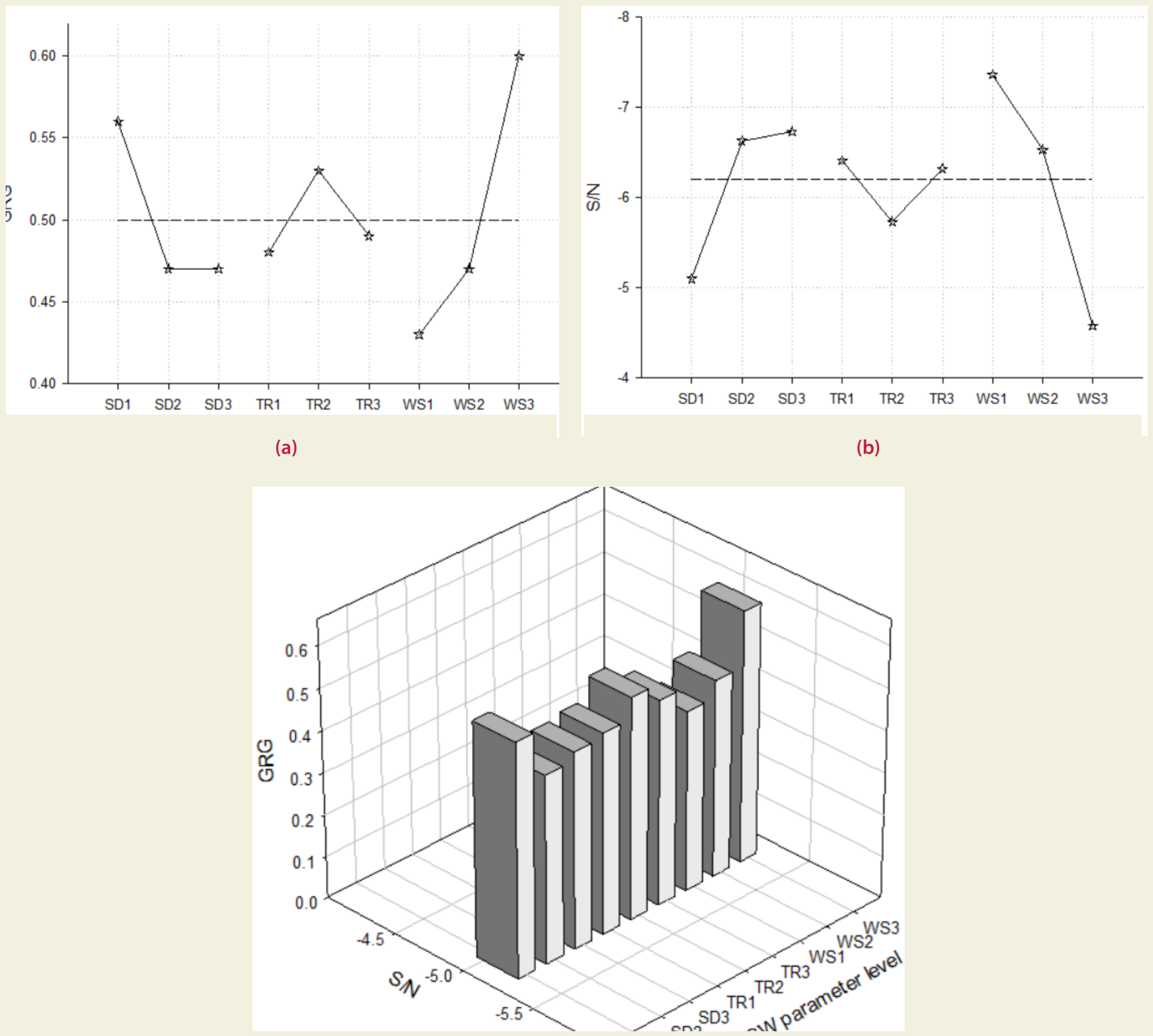

(a)

(b)

(c)

Figure 4. (a) GRG vs. Parameter level, (b) S/N vs. parameter level, c) 3D bar chart representation GRG and S/N vs. parameter level

Table 8. Calculated ANOVA for input parameters of FSW

Parameter	Degree of freedom	Sum of square	Mean square	F ratio	Contribution (%)
SD	2	0.055	0.028	25.01	24.66
TR	2	0.009	0.004	4.28	4.035
WS	2	0.130	0.067	60.44	58.29
SDxTR	4	0.004	0.001	0.950	1.798
SDxWS	4	0.007	0.001	1.720	3.139
TRxWS	4	0.010	0.002	2.280	4.484
SDxTRxWS	8	0.008	0.001	1.100	3.587
Total	**26**	**0.223**			**100**

Table 9. The results of Confirmation

	Initial factor settings	Optimal process condition	
		Prediction	Experiment
Optimum parameter level	$SD_1TR_1WS_1$	$SD_1TR_2WS_3$	$SD_1TR_2WS_3$
Shoulder diameter (mm)	16	-	16
Tool rotation (rpm)	710	-	1000
Welding speed (mm/min)	56	-	160
Grey relational grade	0.485	0.690	0.748
	Improvement in GRG: 0.263		

4.2. Analysis of Variance Method

A common statistical method for determining the importance of each component on the process's quality characteristics is the ANOVA methodology. Alternatively say, it provides a clear understanding of how much the process parameter impacts the answer and the relative importance of each parameter taken into account. [10,21,22]. Also, the F ratio test which is the ratio of the mean of squares deviations to the mean of the squared error was used in order to imply the significance of the parameters on the selected response. The ANOVA table for GRG is calculated and tabulated in Table 8.

According to the ANOVA analysis, welding speed of 58.29% and shoulder diameter of 24.66% are the most effective parameter while tool rotation of 4.03% is the primary factor that has the least impact on joint efficiency, elongation, and tensile strength. Binary interaction contributions of parameters becomes: shoulder diameter and tool rotation of 1.79%, shoulder diameter and welding speed of 3.13%, tool rotation and welding speed of 4.48%. Lastly, triple interaction contributions of shoulder diameter and tool rotation and welding speed of 3.587% were obtained. Figure 5 displays the graphical representation of the FSW parameters' percentage contributions and the effects of their interactions.

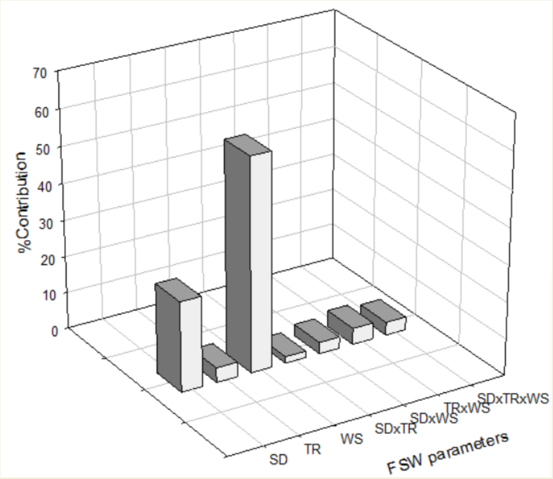

Figure 5. Multiple percentage contributions of parameters

4.3. The Test of Confirmation

The confirmatory test was conducted in the current study utilizing the perfect parameter combination to evaluate the effectiveness in the response parameters and the accuracy of the optimal welding condition ($SD_1TR_2WS_3$). The following formula was used for the prediction GRG ($\hat{\gamma}$) values [21,22]:

$$\hat{\gamma} = \gamma_a + \sum_{i=1}^{p}(\bar{\gamma}_o - \gamma_a) \tag{10}$$

where p is the design parameter number, $\bar{\gamma}_o$ is the average GRG at the optimum level, and γ_a is the overall average GRG [6,14]. The confirmation test results are given in Table 11.

The results of the confirmatory tests make it evident that the GRG has improved overall, coming in at 0.263. The suggested Taguchi-based grey relation optimization approach for the dissimilar friction stir welding process uses this as its primary indication. Also, the method showed that higher tensile strength of 230.43 MPa, elongation of 5.44% and joint efficiency of 74.33 were obtained under determined optimum welding condition. Figure 6 shows the friction stir welded sample at the optimal parameter setting.

For the optimal weld parameter setting, the scanning electron microscope (SEM) analysis of dissimilar friction stir welded aluminum alloys shown in Figure 7 proved that due to the sufficient friction together with proper mixing and material flow promoted the plastic deformation in the weld interface and this caused regular microstructure at the welding zone [1,15].

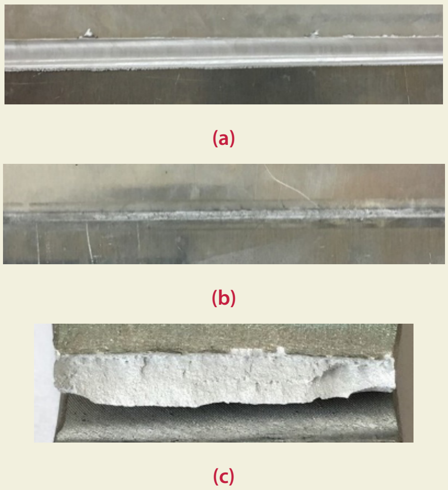

Figure 6. Friction stir welded samples at optimal parameter settings of; SD: 16mm, TR: 1000 rpm and WS: 160 mm/min. (a) top surface, (b) bottom surface, (c) fractured surface

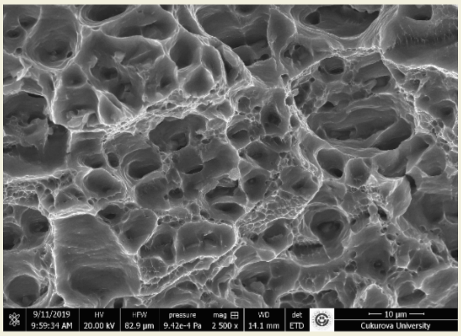

(a) EN AW-5083-H111 weld zone

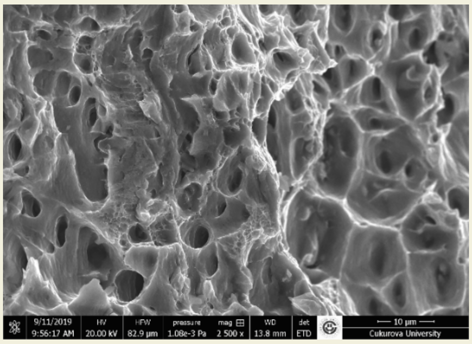

(b) EN AW-6082-T651 weld zone

Figure 7. SEM micrograph (2500X) and EDS image at the optimal process condition at the weld Interface

5. Conclusion

The Taguchi based grey relation analysis method was adopted in this investigation to optimize the friction stir welding process parameters of dissimilar welding for EN AW-5083-H111 and EN AW-6082-T651 aluminum alloys. The following conclusions can be drawn from this work as follows:

1. The Taguchi based grey relation method for FSW of dissimilar aluminum alloys were successfully applied.
2. Taguchi's L_{27} orthogonal array was used to perform the experiments by varying the process parameters such as shoulder diameter, tool rotation and welding speed.
3. The FSW parameters of shoulder diameter of 16 mm, tool rotation of 1000 rpm, and welding speed of 160 mm/min resulted in the best performance for the responses of tensile strength of 230.43 MPa, elongation of 5.44%, and joint efficiency of 74.33.
4. The ANOVA analysis emphasize that the dominant welding parameters on the responses are welding speed (58.29 %), shoulder diameter (24.66 %) and tool rotation (4.03 %) respectively.
5. Significant improvement in grey relation grade of 0.263 was obtained at the optimal parameter setting.
6. The microstructure examination of the FSW joint at the weld interface demonstrated that sufficient friction between tool and samples was properly achieved for the optimal parameter setting condition.

6. References

[1] Ocalir, S., (2018). The investigation of the effects of welding parameters on mechanical properties and corrosion resistance of joints in friction stir welding of dissimilar materials. MSc Thesis, Tarsus University, Graduate Education Institute, Tarsus, Turkey.

[2] Navale, S.B., Borkar, B.R., (2018). Process parameters optimization in FSW process using Taguchi method. International Journal of Advance Research and Innovative Ideas Education, 4(4):551-558.

[3] Meran, C., (2006). The joint properties of brass plates by friction stir welding. Materials and Design, 27(9):719-726. Doi: 10.1016/j.matdes.2005.05.006.

[4] Nandan, R., DebRoy, T., Bhadeshia, H.K.D.H., (2008). Recent advances in friction-stir welding-process, weldment structure and properties. Progress in Materials Science. 53:980-1023. Doi:10.1016/j.pmatsci.2008.05.001.

[5] Lee, W.B., Jung, S.B., (2004). The joint properties of copper by friction stir welding. Materials Letters, 58(6):1041-1046. Doi: 10.1016/j.matlet.2003.08.014.

[6] Meran, C., Kovan, V., (2008). Microstructures and mechan-

ical properties of friction stir welded dissimilar copper/brass joints. Materialwissenschaft Und Werkstofftechnik, 39(8):521-530. Doi: 10.1002/mawe.200800278.

[7] Thomas, W.M., Nicholas, E.D., (1997). Friction stir welding for the transportation industries. Materials & Design, 18:269-273. Doi: 10.1016/S0261-3069(97)00062-9.

[8] Yaroshevsky, A., (2006). Abundances of chemical elements in the Earth's crust. Geochemistry International, 44(1):48-55. Doi: 10.1134/S001670290601006X.

[9] Rankin, D.W.H. (2008)., CRC Handbook of Chemistry and Physics, CRC Press.

[10] http://www.mta.gov.tr/v3.0/bilgi-merkezi/boksit.

[11] Sahu, P.K., Kumari, K., Pal, S., Pal, S.K., (2016). Hybrid fuzzy-grey-Taguchi based multi weld quality optimization of Al/Cu dissimilar friction stir welded joints. Advances in Manufacturing, 4:237–247. Doi: 10.1007/s40436-016-0151-8.

[12] Sun, S.J, Kim, J.S., Lee, W.G., Lim, J.Y., Go, Y., Kim, Y.M., (2017). Influence of friction stir welding on mechanical properties of butt joints of AZ61 magnesium alloy. Advances in Materials Science and Engineering, Article ID 7381403. Doi: 10.1155/2017/7381403.

[13] Shaik, B.G., Gowd, H., Prasad, B.D., (2019). Investigations on friction stir welding process to optimize the multi responses using GRA method. International Journal of Mechanical Engineering and Technology, 10(3):341–352.

[14] Prasath, S., Vijayan, S., Raja, D.E., (2020). Multi Response Optimization of Friction Stir Welding Process Parameters on Dissimilar Magnesium Alloys AZ31 and ZM21 using Taguchi-Based Grey Relation Analysis. La Metallurgia Italiana, 8:18-27.

[15] Palani, K., Elanchezhian, C., (2018). Multi response Optimization of Friction stir welding process parameters in dissimilar alloys using Grey relational analysis. The 3rd International Conference on Materials and Manufacturing Engineering, 390:1-8. Doi: 10.1088/1757-899X/390/1/012061.

[16] Vijayan, S., Raju, R., Rao, S.R.K., (2010). Multiobjective Optimization of Friction Stir Welding Process Parameters on Aluminum Alloy AA5083 Using Taguchi-Based Grey Relation Analysis. Materials and Manufacturing Processes, 25:1206-1212. Doi: 10.1080/10426910903536782.

[17] Gupta, S.K., Pandey, K.N., Kumar, R., (2014). Multi-Objective Optimization of Friction Stir Welding of Aluminium Alloy Using Grey Relation Analysis with Entropy Measurement Method. Nirma Univeristy Journal of Engineering and Technology, 3(1):29-34.

[18] Babu, K.K., Panneerselvam, K., Sathiya, P., Haq, A.N., Sundarrajan, S., Mastanaiah, P., Murthy, C.V.S., (2018). Parameter optimization of friction stir welding of cryorolled AA2219 alloy using artificial neural network modeling with genetic algorithm, International Journal of Advanced Manufacturing Technology, 94, 3117-3129. Doi: 10.1007/s00170-017-0897-6.

[19] Yunus, M., Alsoufi, M.S., (2018). Mathematical modelling of a friction stir welding process to predict the joint strength of two dissimilar aluminium alloys using experimental data and genetic programming. Modelling and Simulation in Engineering, 1-18.

[20] Yousif, Y.K., Daws, K.M., Kazem, B.I., (2008). Prediction of friction stir welding characteristic using neural network. Jordan Journal of Mechanical and Industrial Engineering, 2(3):151-155.

[21] Datta, S., Bandyopadhyay, A., Kumar, P.P., (2008). Grey-based taguchi method for optimization of bead geometry in submerged arc bead-on-plate welding. International Journal of Advanced Manufacturing Technology, 39:1136-1143. DOI: 10.1007/s00170-007-1283-6.

[22] Esme, U., Bayramoglu, M., Kazancoglu, Y., Ozgun, S., (2009). Optimization of weld bead geometry in tig welding process using grey relation analysis and taguchi method. Materiali in Tehnologije, 43(3):143-149.

[23] http://referansmetal.com/alasimli-aluminyum/list/4/genel-endustri.

[24] http://www.empo.com.tr/aluminyum-lama-ve-cubuk/en-aw-6082.html.

EUROPEAN
MECHANICAL
SCIENCE

e-ISSN: 2587-1110

RESEARCH ARTICLE

Numerical analysis of a novel silicone sole-based passive orthosis for home gait rehabilitation training

Hamid Asadi Dereshgi[1*], **Dilan Demir**[1]

[1]Department of Biomedical Engineering, Istanbul Arel University, 34537 Istanbul, Turkey

Orcid: H. Asadi Dereshgi (0000-0002-8500-6625), D. Demir (0000-0001-7413-1597)

Abstract: Drop foot syndrome is a neuromuscular disease characterized by weakness of the muscles in the front of the lower leg. This disease can cause partial or complete loss of control over the foot and affects the ability to lift the foot from the ankle. Orthoses are used to help improve the gait of patients with limited control over the foot muscles. The most important advantages of passive orthoses are that they are light and inexpensive. Thermoplastic materials are generally preferred in lower extremity orthoses due to their high strength and elasticity. The novelty of this study was to perform a silicone sole between the housing sole and the shoe sole in order to minimize the mechanical changes caused by the weight force. Thus, the mechanical behavior of the proposed passive Ankle Foot Orthosis (AFO) at different weight forces was investigated. It was observed that displacement, stress, and strain values increased with the increase of weight force and vibration frequency. Consequently, Polypropylene-based orthosis was accepted as the ideal design material as it exhibits higher elastic behavior than Polyetherimide and Polylactic Acid-based orthoses. Consequently, this study enables researchers a useful reference on passive orthosis parameters such as modeling, material behavior, shape control, geometry, and size optimization for key biomechanical engineering applications.

Keywords: Passive orthosis, Rehabilitation system, Finite Element Analysis, Polypropylene, Polyetherimide, Polylactic Acid

1. Introduction

Drop foot syndrome is the loss of dorsiflexion movement of the foot from the ankle. It often occurs in cases of stroke and disorders of the muscular system. This condition, which reduces the quality of life of the patients, is treated with electrical stimulation, gait training, foot support, and splints. Foot orthoses, one of these treatment methods, provide improvement by keeping the feet of the patients in plantar flexion [1]. Foot orthoses are divided into three parts as passive, semi-active, and active actuators [2]. Passive orthoses have been preferred in recent years due to the development of technology and ease of fabrication. Literature survey shows that there are many studies about the foot orthosis. For example, Jamshidi et al. (2010) designed a passive foot orthosis to reduce the stress on the sole of the foot. The sole of the presented orthosis was formed in three layers as the inner, middle, and outer parts, additionally, elastic and hyper-elastic material was defined and the kinematics changes during walking were examined. As a result of the study, it was observed that the stress in the midfoot decreased [3]. Deberg et al. (2014) proposed a Shape Memory Alloy (SMA)-based passive foot orthosis. The passive AFO was equipped with a hinged brace and SMA wires. It was aimed to store mechanical energy thanks to these super elastic wires. It was observed that the SMA AFO presented in this study has the ability to meet the torque angle requirements much better than the traditional passive AFO [4]. Kubasad et al. (2020) designed a passive orthosis in order to prevent foot drop disease. In this study, 3 mm and 4 mm thick polypropylene and high-density polyethylene material were used for static analysis. In addition, dynamic calculations were carried out to determine the situations in the gait analysis. In order to analyze the force of a 55 kg human weight, 275 N was used in the analysis. As a result, the tensile strength was obtained by Finite Element Analysis (FEA) to be 30 MPa [5]. Gautam et al. (2021) designed an AFO with 4 mm thickness and polypropylene material. Stress analysis of the proposed model was performed with FEA. A force of 294 N was applied to the simulated orthosis for a 60 kg patient and the maximum stress was obtained as 31.26 MPa [6].

In this study, passive AFO based on Polypropylene, Polyetherimide, and Polylactic Acid was designed and analyzed by the Finite Element Method (FEM). The purpose of the study was to investigate the mechanical behavior of

---

[*] Corresponding author.
Email: hamidasadi@arel.edu.tr

European Mechanical Science (2022), 6(4): 251-256
https://doi.org/10.26701/ems.1123082
Received: May 29, 2022 — Accepted: September 19, 2022

the lower sole of the proposed orthosis at different weight forces. The paper is organized as follows. The working principle of the new AFO and the finite element modeling procedure is presented in Section 2. In Section 3, the results of FEM simulations are presented and discussed. Finally, the concluding remarks are reviewed in Section 4.

2. Material and Method

In this study, passive AFO based on Polypropylene, Polyetherimide, and Polylactic Acid was investigated (see Figure 1). The proposed AFO consisted of a housing and a silicone sole, which were 2 mm and 3 mm thick, respectively. The material properties of AFO were given in Table 1. The mechanical behavior of the proposed orthosis at applied dynamic weight forces was investigated for three different materials. It should be noted that forces ranging from 50 kg to 100 kg were applied to the upper sole of the AFO in 10 kg increments. In addition, dynamic forces were applied at 1 Hz to 4 Hz intervals in 1 Hz increments. Analyzes were performed using the FEM with a sensitivity of 0.001. Moreover, mesh convergence analysis was performed to determine the accuracy of the analyzes (see Figure 2). Therefore, Normal, Fine, and Finer meshes (see Figure 3) were defined for the AFO model. The physical properties of the meshes were given in Table 2. As a result of the mesh convergence analysis, 6.48% and 0.90% error rates were obtained between the first meshing step (Normal), the second meshing step (Fine), and the third meshing step (Finer), respectively. Therefore, Fine mesh was accepted as the ideal mesh. The results of the mechanical behavior of the orthoses were given in Section 3.

3. Results

In this study, a novel passive orthosis was proposed for the treatment of foot drop patients. The properties of Polypropylene, Polylactic Acid, and Polyetherimide materials were numerically defined separately for the presented orthosis. The mechanical behavior of three different materials was investigated against the weight force. The me-

Table 1. Mechanical properties of materials used in AFO's housing.

Materials	Density (kg/m³)	Young's modulus (GPa)	Poisson's Ratio
Polypropylene (PP)	900	2.4	0.43
Polylactic Acid (PLA)	1250	3.7	0.35
Polyetherimide	1340	2.5	0.36
Silicone Rubber	3800	1.90	0.50

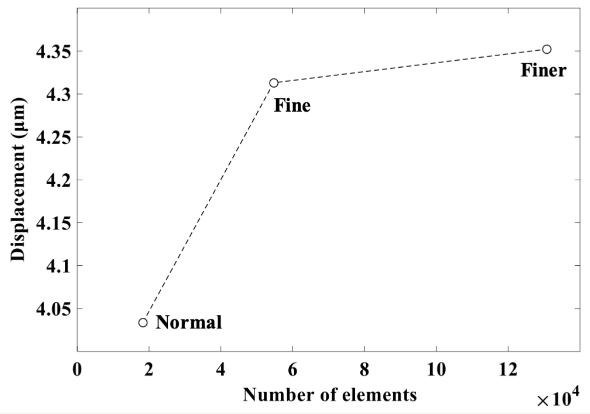

Figure 2. Mesh convergence analysis for the model displacement.

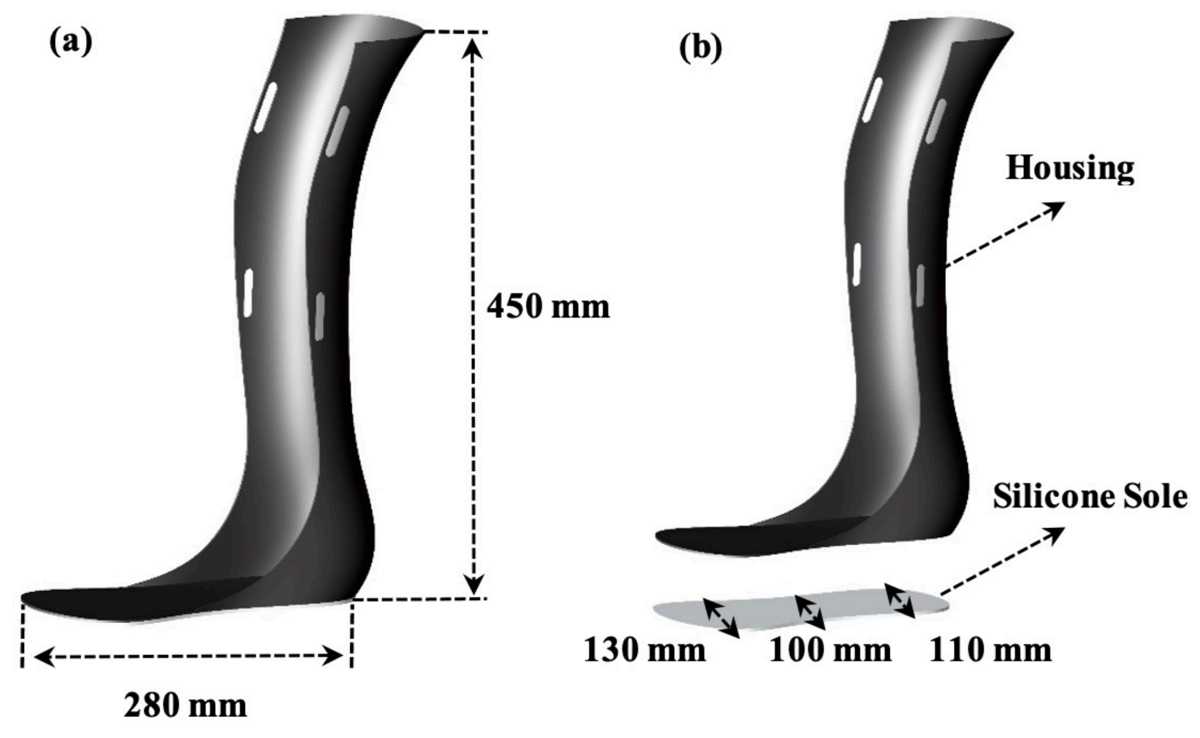

Figure 1. Proposed AFO view, **(a)** integrated, **(b)** exploded.

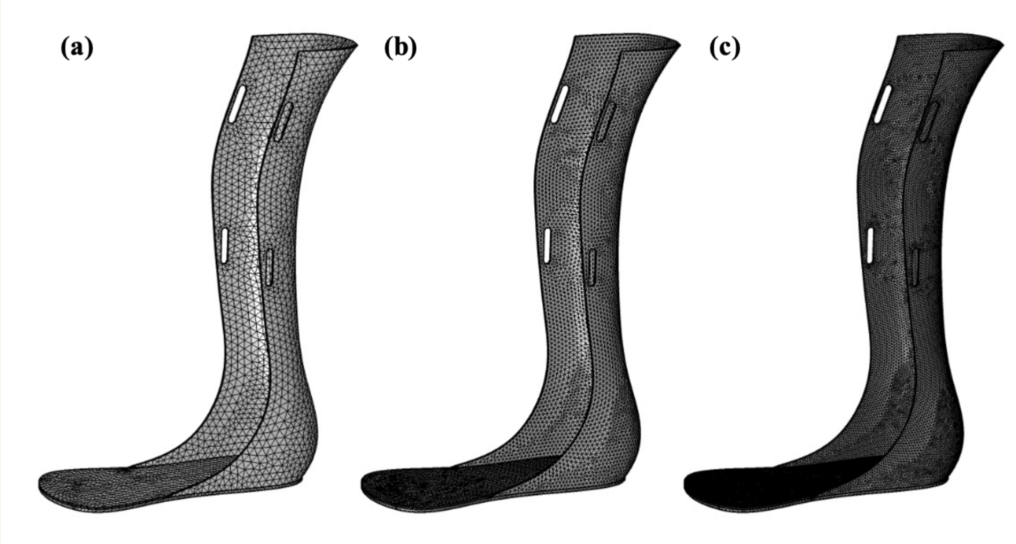

Figure 3. Mesh types of the finite element model, a) Normal, b) Fine, and c) Finer

Table 2. Specifications of Finite Element Method (FEM).

Domain element statistics	Number of elements	Minimum element quality	Average element quality	Element volume ratio	Mesh volume (μm^3)
Normal	18237	0.04002	0.3488	0.002276	3.316E14
Fine	54673	0.1695	0.5423	0.002881	3.316E14
Finer	130710	0.1635	0.6704	0.002966	3.315E14

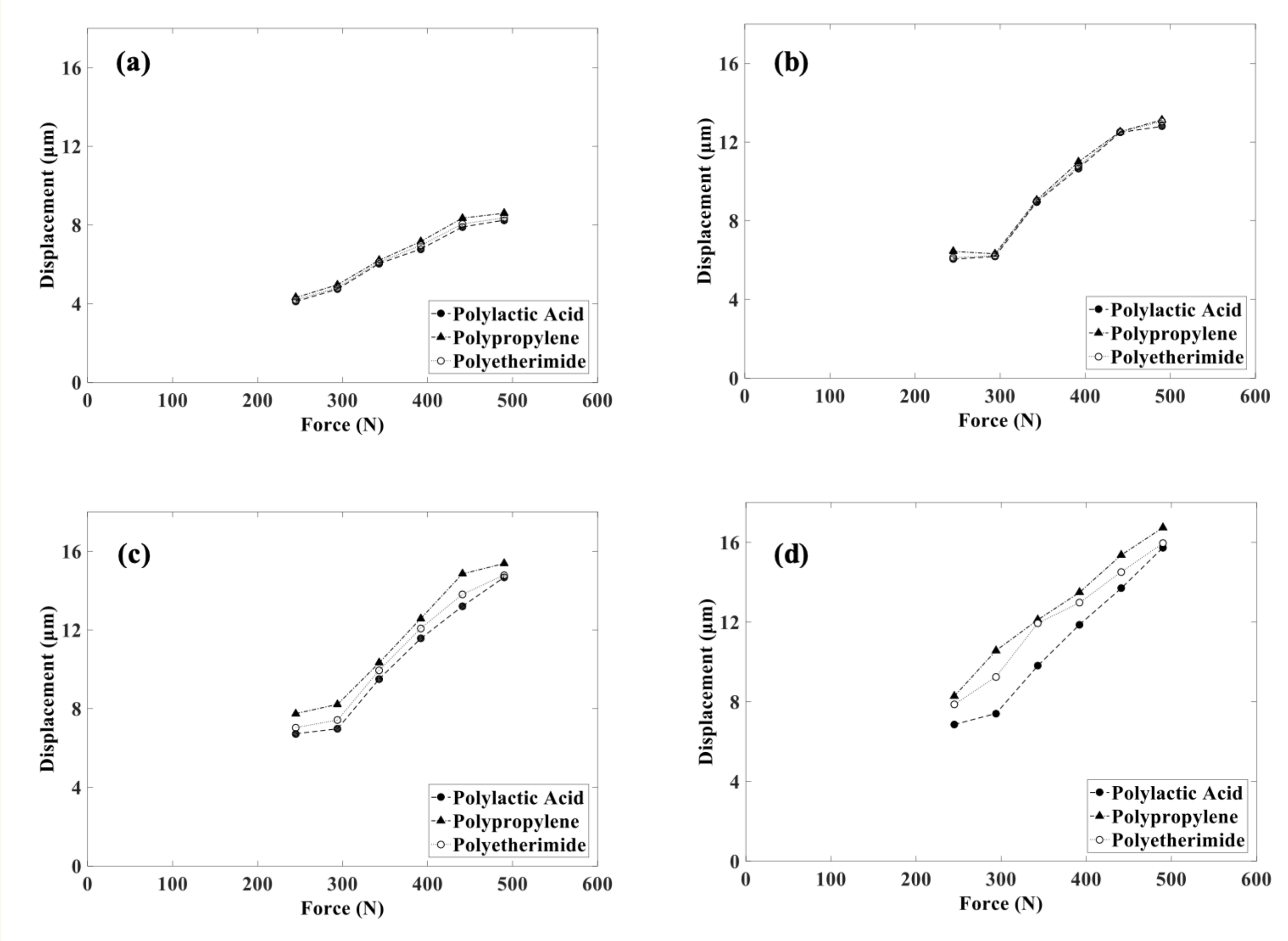

Figure 4. The maximum displacement results at (a) 1 Hz, (b) 2 Hz, (c) 3 Hz, and (d) 4 Hz.

chanical behavior of the proposed orthosis was analyzed between 50 kg and 100 kg by 10 kg steps. It is worth noting that dynamic analysis was performed for the optimized design to examine the behavior of the AFO in the walking condition. Dynamic forces were applied to the upper sole of the orthosis in 1 Hz steps between 1 Hz and 4 Hz. Consequently, displacement (See Figure 4) and stress-strain (See Figure 5) values of Polypropylene were higher than Polyetherimide and Polylactic Acid materials since it has a more flexible structure. Maximum displacements of Polypropylene, Polyetherimide, and Polylactic Acid based orthoses were obtained as 16.74 µm, 15.96 µm, and 15.73 µm at 490 N, and 4 Hz, respectively. In addition, the minimum displacement was obtained as 4.31 µm, 4.2 µm, and 4.10 µm for Polypropylene, Polyetherimide, and Polylactic Acid materials at 245 N and 1 Hz, respectively. The vibrational frequencies of the dynamic forces were less than the resonance frequency of the proposed materials. Therefore, a linear correlation was observed between mechanical behavior and vibration frequencies. Accordingly, the same registrations were obtained for the stress-strain parameters. The maximum stress achieved on the upper sole of the Polypropylene, Polyetherimide, and Polylactic Acid based orthosis was 1800373.729 N/m^2, 1798258.732 N/m^2, and 1767058.128 N/m^2, respectively. In addition, the minimum stress values were obtained as 453257.1671 N/m^2, 422823.2138 N/m^2, and 402392.4274 N/m^2, respectively.

It is clear that the displacement, stress, and strain results achieved in this study are less than the orthoses with the same mechanical and material properties proposed in the open literature [6,7]. As mentioned in Section 2, the proposed AFO has two soles and the bottom sole was silicone. Thus, the mechanical behavior of AFO was low due to the high elastic property of the silicone sole. In addition, the silicone sole absorbed the weight forces due to its compression feature, hence, there were 95% to 99% linear correlation was obtained between force and displacement, which was 92% to 100% between force and stress-strain. In this study, it was obtained that the stress and strain relationship was linear in different materials, forces, and frequencies. Thus, it is evident that the materials foreseen for the AFO design are suitable for the treatment of patients weighing up to 100 kg, as they remain in the elastic region as a result of deformation.

4. Discussion

Many studies have been carried out on passive AFOs. However, none of them contain detailed information about design parameters, mechanical and material effects on physical therapy and rehabilitation. In addition, new designs have been proposed by different researchers, but

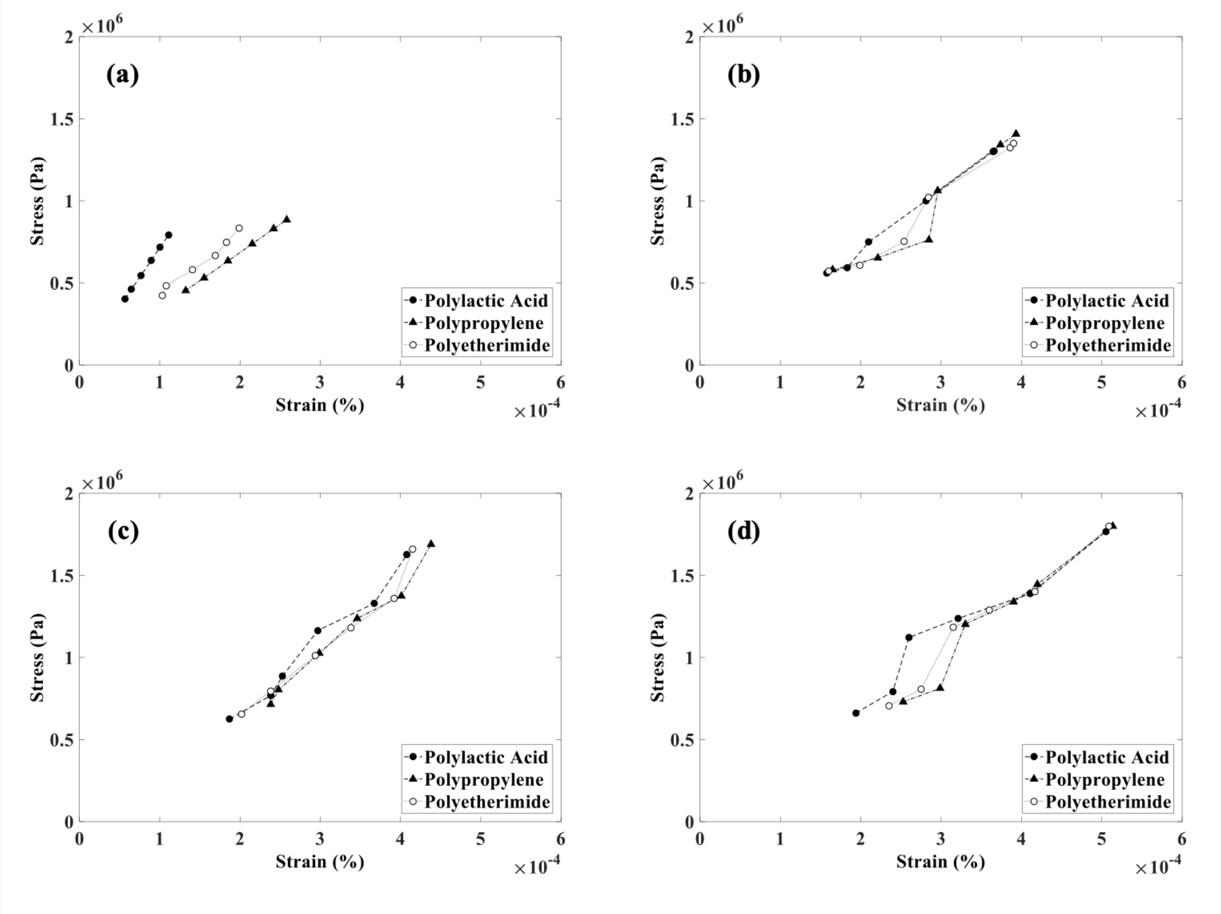

Figure 5. The maximum stress-strain results at (a) 1 Hz, (b) 2 Hz, (c) 3 Hz, and (d) 4 Hz.

there are no studies supporting each other. For example, Cha et al. (2017) fabricated a polyurethane-based AFO using rapid prototyping technique [8]. Biocompatibility, durability and minimum elastic deformation are important parameters to be considered in the housing design of passive AFO [9,10]. The elastic modulus of Polyurethane (~0.24 GPa) is very low compared to Polypropylene (~8.25 GPa), Polyetherimide (~56 GPa), and Polylactic Acid (~13.8 GPa). Therefore, the AFO recommended by Cha et al. (2017) has been durable up to 300,000 repetitions. The main purpose of passive AFOs is to stabilize the patient's foot in the desired position. The low elastic modulus indicates that it is not suitable for this purpose. Additionally, Polyurethane contains toxicity compared to Polypropylene, Polyetherimide, and Polylactic Acid materials. However, non-isocyanate synthesis methods are preferred for biomedical applications, hence its tensile stress is reduced [11-13]. Accordingly, it is clear that Polyurethane is not very compatible in terms of durability and biocompatibility compared to Polypropylene, Polyetherimide, and Polylactic Acid materials.

Kubasad et al. (2020) numerically analyzed the proposed polypropylene-based AFO [5]. Housing thickness of the presented model was 3 mm and 4 mm. The mechanical behavior of the AFO was obtained in the walking scenario. As a result of dynamic analysis, 14.69 mm deformation was obtained in the lower sole of the AFO. A high deformation value may cause the AFO to break or crack. Therefore, the touch points of the foot and the AFO should be predetermined by biomechanical analysis. By contrast, the deformation of our proposed orthosis was 4.63 µm at the same conditions. This is due to the spring-like behavior of the silicone sole.

Gautam et al. (2021) investigated a polypropylene-based passive AFO [6]. The purpose of the study was to keep the patient's foot in a stable position. Therefore, the mechanical behavior of the AFO was studied under the influence of static forces. However, dorsiflexion and plantarflexion movements apply dynamic forces to the AFO. The frequency of dynamic forces directly affects the durability of the AFO housing. Therefore, we applied different dynamic forces to analyze the durability of our proposed AFO under walking conditions. It is worth mentioning that there is an inverse correlation between the housing thickness of the AFO and the stress-strain curve. Additionally, Gautam et al. (2021) also examined the relationship between the housing thickness and durability of AFO. In this study, the housing of AFO was simulated from a 4 mm thick polypropylene material. Consequently, a maximum stress of 31.26 MPa was obtained with the application of 294 N. However, a maximum stress of 0.53 MPa was obtained at 294 N in our proposed 2 mm thick polypropylene-based AFO. Although the housing thickness of the AFO presented by Gautam et al. (2021) was two times that of our proposed model, there was a 98.30% decrease in stress at the same force conditions. The reason for the reduction of stress was the housing, silicone sole and shoe sole designed in sandwich appearance. Thus, this feature is the outstanding innovative aspect of our study.

5. Conclusion

Foot drop is a complication characterized by difficulty in raising the front of the foot. It can be temporary or permanent, depending on the degree of muscle weakness or paralysis. This disorder can occur in one or both feet. Toe walking is common in children just beginning to learn to walk, but they usually return to normal walking after the age of two. Some people may continue walking with this model due to habituation or because their cuff muscles and tendons shorten over time. This disorder is not usually a separate disease in itself and is a symptom of a significant problem. Foot drop is usually diagnosed by physical examination. Foot drop is characterized by the inability or impairment of the ability to lift the toes or flex the ankle inward (dorsiflexion). Passive foot orthoses help patients stabilize their feet and ankles in a normal position. Moreover, the therapeutic use of passive AFOs has proven beneficial in the open literature [14]. Therefore, many studies have been carried out on passive AFO. However, none of them contain detailed information about design parameters and material effects on mechanical behavior. In this study, the effects of material behavior on AFO performance were investigated using the FEM. In addition, a silicone sheet was preferred to minimize the effect of the weight force applied to the orthosis. Physically, silicone showed spring property against applied forces. Thus, it has increased the resistance of the orthosis against forces and its useful life. In addition, silicone is a good biocompatible material and was appropriate for biomedical applications [15]. After the proposed AFO is studied experimentally, it will have significant contributions to rehabilitation and clinical applications.

6. Acknowledgement

The authors would like to acknowledge the technical support provided by Artificial Intelligence Studies, Application and Research Center (ArelMED-I) of Istanbul Arel University related to the numerical analysis.

7. References

[1] Grissom, S.P., Blanton, S. (2001). Treatment of upper motoneuron plantarflexion contractures by using an adjustable ankle-foot orthosis. Archives of physical medicine and rehabilitation, 82(2): 270-273, DOI:10.1053/apmr.2001.19018.

[2] Chen, B., Zi, B., Zeng, Y., Qin, L., Liao, W.H. (2018). Ankle-foot orthoses for rehabilitation and reducing metabolic cost of walking: Possibilities and challenges. Mechatronics, 53: 241-250, DOI:10.1016/j.mechatronics.2018.06.014.

[3] Jamshidi, N., Hanife, H., Rostami, M., Najarian, S., Menhaj, M.B., Saadatnia, M., Salami, F. (2010). Modelling the interaction of ankle-foot orthosis and foot by finite element

methods to design an optimized sole in steppage gait. Journal of medical engineering & technology, 34(2): 116-123, DOI:10.3109/03091900903402063.

[4] Deberg, L., Taheri Andani, M., Hosseinipour, M., Elahinia, M. (2014). An SMA passive ankle foot orthosis: Design, modeling, and experimental evaluation. Smart Materials Research, 2014: 1-11, DOI:10.1155/2014/572094.

[5] Kubasad, P.R., Gawande, V.A., Todeti, S.R., Kamat, Y.D., Vamshi, N. (2020). Design and analysis of a passive ankle foot orthosis by using transient structural method. In Journal of Physics: Conference Series, 1706(1): 1-12, DOI:10.1088/1742-6596/1706/1/012203.

[6] Gautam, G.Y., Jain, M.L., Gehlot, V. (2021). Design and Analysis of Thermoplastic Polypropylene Ankle Foot Orthosis. Journal of Manufacturing Engineering, 16(3): 087-091, DOI:10.37255/jme.v16i3pp087-091.

[7] Chen, R.K., Chen, L., Tai, B.L., Wang, Y., Shih, A.J., Wensman, J. (2014). Additive manufacturing of personalized ankle-foot orthosis. Proceedings of transactions of the North American manufacturing research institution of SME (NAMRC42), 42.

[8] Cha, Y.H., Lee, K.H., Ryu, H.J., Joo, I.W., Seo, A., Kim, D.H., Kim, S.J. (2017). Ankle-foot orthosis made by 3D printing technique and automated design software. Applied bionics and biomechanics, 1-6, DOI:10.1155/2017/9610468.

[9] Shorter, K.A., Xia, J., Hsiao-Wecksler, E.T., Durfee, W.K., Kogler, G. F. (2011). Technologies for powered ankle-foot orthotic systems: Possibilities and challenges. IEEE/ASME Transactions on mechatronics, 18(1): 337-347, DOI:10.1109/TMECH.2011.2174799.

[10] Chaudhari, R., Loharkar, P.K., Ingle, A. (2022). Medical Applications of Rapid Prototyping Technology. In Recent Advances in Industrial Production, 241-250.

[11] Ozimek, J., Pielichowski, K. (2021). Recent advances in polyurethane/POSS hybrids for biomedical applications. Molecules, 27(1): 1-31, DOI:10.3390/molecules27010040.

[12] Heijkants, R.G.J.C., Schwab, L.W., Van Calck, R.V., De Groot, J.H., Pennings, A.J., Schouten, A.J. (2005). Extruder synthesis of a new class of polyurethanes: Polyacylurethanes based on poly (ε-caprolactone) oligomers. Polymer, 46(21): 8981-8989, DOI:10.1016/j.polymer.2005.06.089.

[13] Banoriya, D., Purohit, R., Dwivedi, R.K., Baghel, U. (2019). Development and testing of polyurethane based composites using rapid prototyping techniques for biomedical applications-a review. Materials Today: Proceedings, 18: 5410-5415, DOI:10.1016/j.matpr.2019.07.569.

[14] Asadi Dereshgi, H., Dal, H., Demir, D., Türe, N.F. (2021). Orthoses: A Systematic Review. Journal of Smart Systems Research, 2(2): 135-149.

[15] Saddow, S.E. (2012). Silicon carbide biotechnology: a biocompatible semiconductor for advanced biomedical devices and applications. Elsevier, Amsterdam.

EUROPEAN MECHANICAL SCIENCE
e-ISSN: 2587-1110

RESEARCH ARTICLE

Electric tariffs and thermal energy storage systems for buildings

Ahmet Fertelli[1*]

[1]Department of Mechanical Engineering, Engineering Faculty, Sivas Cumhuriyet University, Sivas, Turkey

Orcid: A. Fertelli (0000-0003-2279-1918)

Abstract: Thermal energy storage methods are systems that can be an alternative to the systems used especially in residential heating in our country. These systems shift the electricity demand to night and they constitute an electricity use strategy that is both effective and efficient. In this study, the ten-year price changes of the fuels used for heating in our country, the change in the real electricity consumption of a province over time, the electricity tariffs were examined and cost calculations were made in case of heating a space. It is seen that fuel prices have increased significantly in recent years, and thermal energy storage systems (TES) are 20-40% less costly than other systems until 2020, and 40-55% less costly than natural gas in 2021 and 2022.

Keywords: Thermal Energy Storage, Electric Tariff, Energy Efficiency, Heating

1. Introduction

Energy production, which plays an important role in providing the basic needs of human beings for life, is the most important issue with the increasing primary energy demand in proportion to both population growth and increasing industrialization. It has also emerged that it is necessary to support the transition to clean energy in total energy production and to provide support for the development of its sub-components wind turbines, batteries, electrolysers and other technologies. According to the 2050 projection, it is expected that the first role of coal in power capacity will pass to natural gas by 2030, and then solar photovoltaic panels and wind systems are expected to gradually replace coal and natural gas [1,2]. In our country, according to the 2021 TEIAŞ (Turkish Electricity Transmission Corporation) December power report, it is seen that the total electrical installed power capacity has increased to 99,819.6 MW, the total number of power plants is 10457, and natural gas ranks first in total installed power [3]. It is known that with the investments made in renewable energy in recent years, the installed power from solar energy has increased by 7.80% and wind energy by 10.6% compared to the total power [4].

A three-dimensional model is designed for a thermal storage device used in a space heating. It was observed that the brick and outlet air temperatures in the system increased up to 1002 K and 835 K, respectively, and 40.4% of the total electric heating energy was used for charging in natural convection. [5]. In the city of Nova Scotia, it has been determined that by applying incentive programs for homeowners who heat their homes with electricity to switch from conventional electric heaters to electric thermal storage systems, savings in the range of 41-48% are achieved in ETS systems compared to conventional heating systems, with a payback period of less than 8 years [6]. By using the wind farm and thermal energy storage system together in Prince Edward Island of Canada, 5.15 MW of the residential heating demands were met. In the study, in which simulations were made on the model created with the real housing demand profile, a load model was defined and it was aimed to offer energy, maintain the comfort level and increase the efficiency of the electricity distribution network in case the customer demand changes [7]. In the numerical study on the feasibility of the central thermal storage system, different models were developed using the TRNSYS program. [8], Annual heating cost and unit storage capacities are examined in numerical models made to manage the heating and electricity demand of central electric thermal storage systems in Quebec [9].

2. Materialals and Methods

2.1. Thermal energy storage

Energy storage can be done in 4 different categories: chemical, mechanical, thermal and electrical. Synthetic natural gas and hydrogen are used in chemical energy storage, flywheel, compressed air etc. in mechanical en-

---

[*] Corresponding author.
Email: fertelli@cumhuriyet.edu.tr

European Mechanical Science (2022), 6(4): 257-262
https://doi.org/10.26701/ems.1188559
Received: October 13, 2022 — Accepted: October 31, 2022

ergy storage, battery, fuel cell, electrochemical capacitor, magnetic and conductive in electrochemical energy storage, thermo-chemical, sensible heat and latent heat in thermal energy storage are used (Figure 1) . Thermal energy storage (TES) with sensible heat is obtained by increasing or decreasing the temperature difference in materials with low heat transmission coefficient but also high specific heat and density, by performing charging and discharging processes. In heating processes, it is preferred to use materials that can store energy at high temperatures. It is possible for them to preserve the stored energy for a long time with a good insulation and to perform heating in the space for a long time during use.

2.2. Electric Tariffs

The most important parameter in thermal energy storage systems is the tariffs determined by the electricity supplier companies. In the our country, electricty pricing is made according to many different parameters such as the type of electricity usage, places of use, distribution and transmission system users [10]. In Table 1, there is a sample electricity tariff table published by EPDK (Republic of Türkiye Energy Market Regulatory Authority) in certain periods [10]. In tariff pricing, distribution system users are divided into industry, business, residential, agricultural irrigation, lighting, low voltage and medium voltage users. In our country, household subscribers with a single

Table 1. Activity based tariffs approved by EPDK and approved as March 1,2022 [10]

	1/3/2022	Activity Based Consumer Tariffs(kr/kWh)					Total Tariffs Excluding Power Fee (kr/kWh)			
Transmission System Users	Transmission System Users Receiving Energy from the Incumbent Supply Company	Retail One-Time Energy Cost	Retail Daytime Energy Fee	Retail Peak time Energy Fee	Retail Night time Energy Fee	Distribution Fee	Single Time	Daytime	Peak time	Night time
	Consumer	370,0212	374,5341	590,2971	200,3921	0,0000	370,0212	374,5341	590,2971	200,3921
Distribution System Users	Distribution System Users	Retail One-Time Energy Cost	Retail Daytime Energy Fee	Retail Peak time Energy Fee	Retail Night time Energy Fee	Distribution Fee	Single Time	Daytime	Peak time	Night time
	Medium voltage						Medium voltage			
	Double-Term						Double-Term			
	Industry	157,3709	159,3408	253,5227	83,3267	14,5454	171,9163	173,8862	268,0681	97,8721
	Public and Private Services Sector and Other	179,7944	181,6169	286,0048	98,5597	22,6686	202,4630	204,2855	308,6734	121,2283
	Residence	130,2756	132,4429	211,3815	69,3172	22,4532	152,7288	154,8961	233,8347	91,7704
	Agricultural Activities	134,8303	136,2335	216,3321	72,2270	18,6693	153,4996	154,9028	235,0014	90,8963
	Lighting	165,5392				21,7570	187,2962			
	Single-Term						Single-Term			
	Industry	156,8345	158,8053	252,9872	82,7910	16,0666	172,9011	174,8719	269,0538	98,8576
	Public and Private Services Sector and Other	183,0499	184,8724	289,2603	101,8147	28,2765	211,3264	213,1489	317,5368	130,0912
	Residence	131,3609	133,5284	212,4659	70,4019	27,7239	159,0848	161,2523	240,1898	98,1258
	Agricultural Activities	136,3465	137,7497	217,8485	73,7424	23,2453	159,5918	160,9950	241,0938	96,9877
	Lighting	168,5589				27,1401	195,6990			
	Low voltage						Low voltage			
	Single-Term						Single-Term			
	Industry	166,9128	168,8825	263,0643	92,8686	24,8584	191,7712	193,7409	287,9227	117,7270
	Public and Private Services Sector and Other(30 kWh/day ve below)	133,7425	190,8402	295,2280	107,7829	33,6884	167,4309	224,5286	328,9164	141,4713
	Public and Private Services Sector and Other(30 kWh/day ve above)	189,0181	190,8402	295,2280	107,7829	33,6884	222,7065	224,5286	328,9164	141,4713
	Residence (8 kWh/day ve below)	79,4622	137,0507	215,9889	73,9241	32,9483	112,4105	169,9990	248,9372	106,8724
	Residence (8 kWh/day above)	134,8829	137,0507	215,9889	73,9241	32,9483	167,8312	169,9990	248,9372	106,8724
	Agricultural Activities	139,8998	143,5746	221,4022	77,2958	27,6811	167,5809	171,2557	249,0833	104,9769
	Lighting	174,2104				32,2661	206,4765			

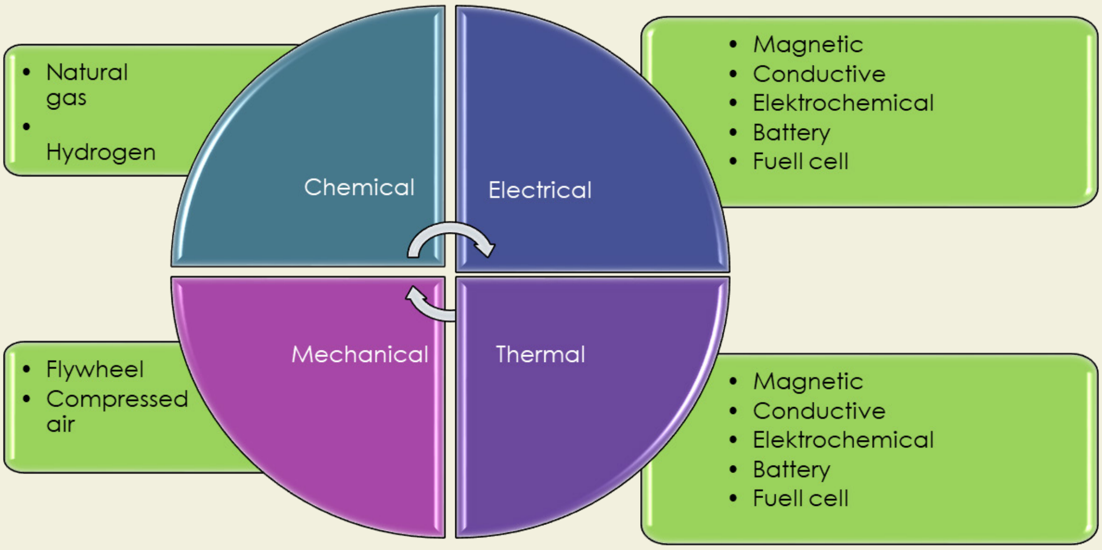

Figure 1. Energy storage methods

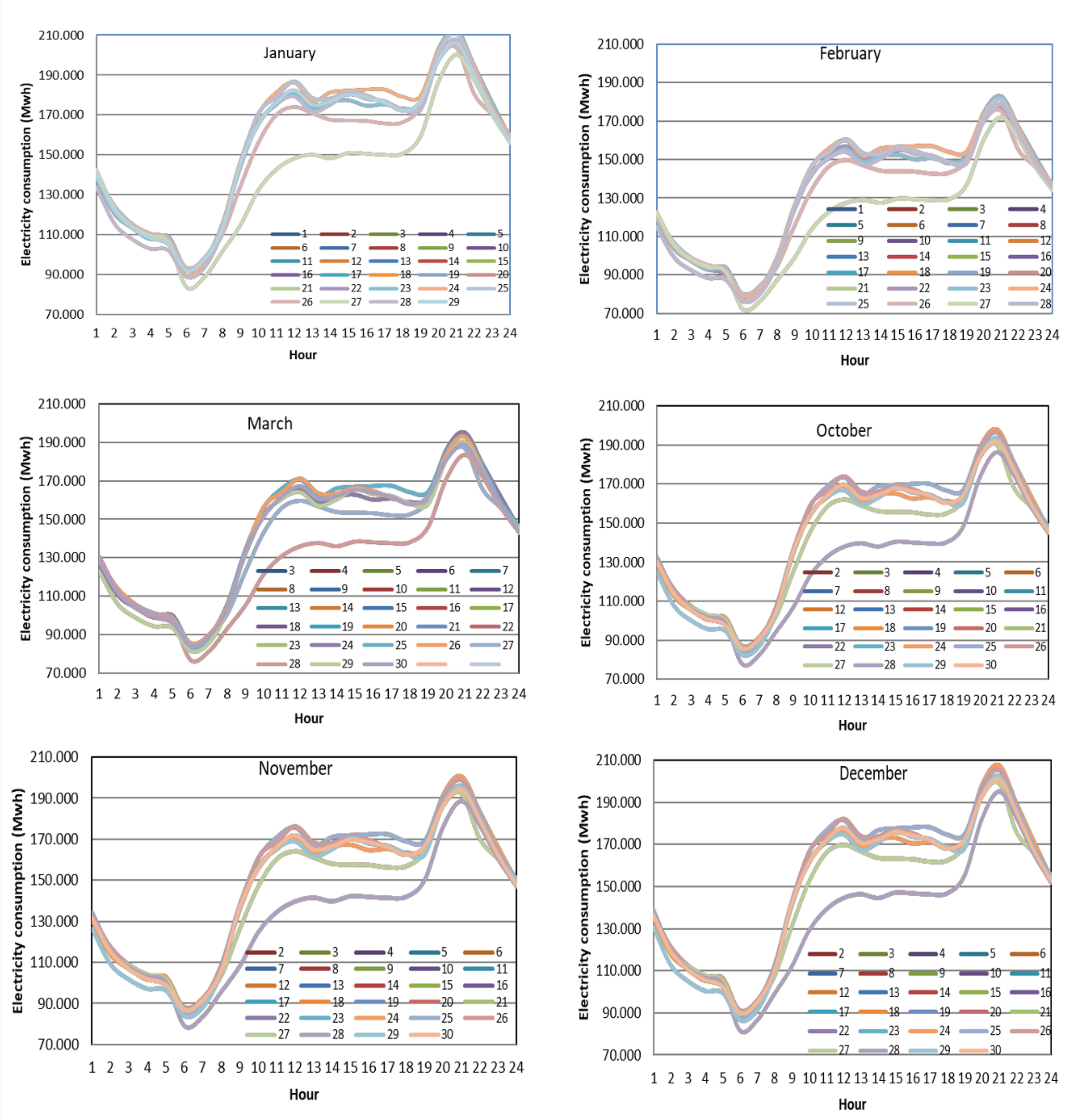

Figure 2. Hourly electricity consumption for a province [11]

term of low voltage prices the electricity they consume in their residences over this tariff. In addition, as can be seen from the Table 1, there are 4 different pricing options for all types of users and voltages: one-rate tariff, single time, daytime, peak and night (three- rate tariff). Residential users can choose one or three-time tariff pricing according to their preferences. As of 1.3.2022, a separate pricing option has been added depending on whether the consumption is below or above 8 kWh per day. In the one-time tariff, the electricity consumed for a day is calculated over a single price, while in the three-time tariff, it is calculated at 3 different prices. When the prices are examined, it is seen that the night tariff price is the cheapest, the day price is close to the single time price, and the peak price is the highest.

3. Results and Discussions

Hourly electricity consumption for a province in Turkey during the heating season (October – March) is shown in Figure 2 [11]. As can be seen, electricity demand increases from 06:00 to 12:00 in the morning and becomes constant between 13:00 and 18:00. The electricity consumption, which increases again after 18:00, reaches its maximum value around 21:00 and decreases again after 22:00. When looking at all the months, it is seen that the peak load occurs in the peak time (18:00-22:00) and the least electricity consumption occurs in the night time period.

All electricity planning is made according to the peak load occurring during these hours. By using these three-

https://doi.org/10.26701/ems.1188559

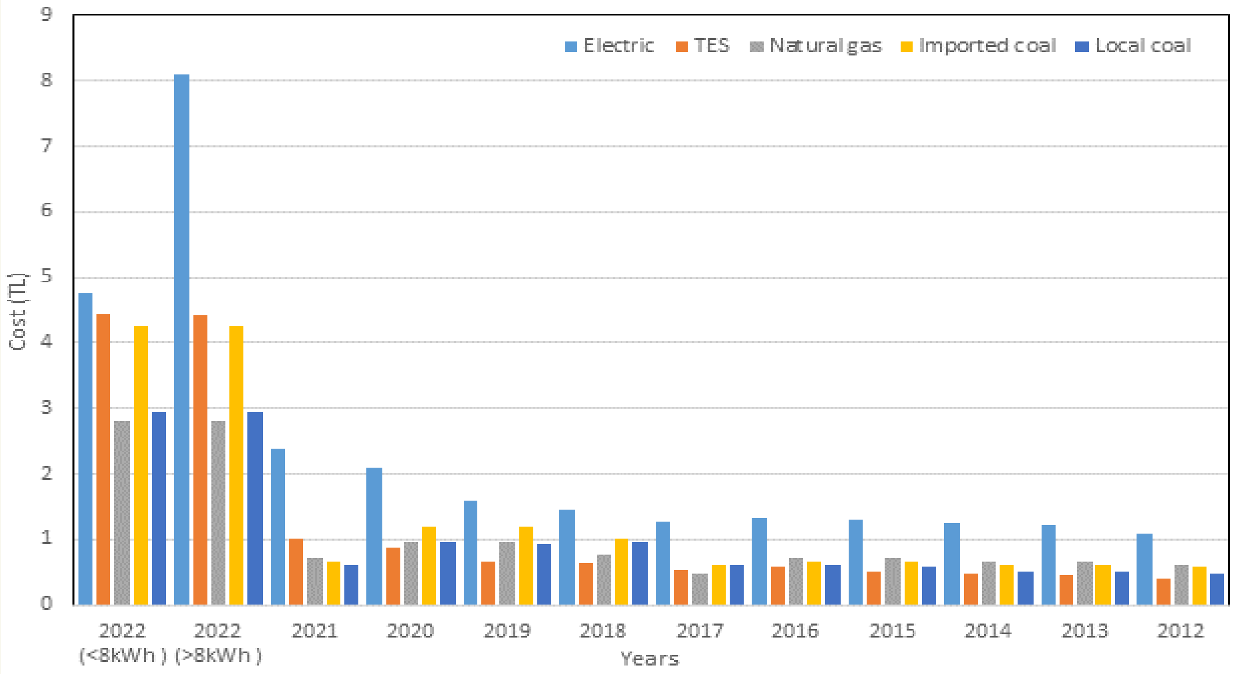

Figure 3. Heating costs for different fuels

Table 2. Variation of prices of different fuels by years TL(Turkish Lira)/kWh [10,12]

Years	Natural gas (TL/kWh)	Imported coal (TL/kWh)	Local coal (TL/kWh)	Fuel Oil (TL/kWh)	Retail One-Time Energy Cost (TL/kWh)	Retail Daytime Energy Fee (TL/kWh)	Retail Peak time Energy Fee (TL/kWh)	Retail Night time Energy Fee (TL/kWh)
1.03.2022 (<8kWh)	0.47	0.71	0.49	1.72	0.794622	1.37051	2.15989	0.739241
1.03.2022 (>8kWh)	0.47	0.71	0.49	1.72	1.348.829	1.370507	2.159889	0.7392
1.01.2021	0.12	0.11	0.1	0.18	0.397629	0.405797	0.703224	0.167946
1.04.2020	0.16	0.2	0.16	0.36	0.348202	0.355468	0.620066	0.14387
1.04.2019	0.16	0.2	0.156	0.39	0.263304	0.268803	0.469052	0.108664
1.01.2018	0.13	0.17	0.16	0.45	0.244666	0.243097	0.434817	0.106691
1.04.2017	0.079	0.1	0.1	0.14	0.214058	0.212672	0.382009	0.090337
1.07.2016	0.12	0.11	0.1	0.18	0.22102	0.219634	0.388971	0.097299
1.01.2015	0.12	0.11	0.096	0.18	0.216738	0.19934	0.36091	0.082684
1.07.2014	0.11	0.1	0.083	0.23	0.207728	0.191159	0.345038	0.080056
1.07.2013	0.11	0.1	0.083	0.23	0.203752	0.187183	0.340562	0.07658
1.04.2012	0.102	0.098	0.078	0.23	0.181647	0.166939	0.303092	0.06875896

time tariffs and thermal energy storage systems together, it aims to reduce the peak load and shift it to night hours when electricity demand is much less. In the study, the 10-year price distribution of the fuels used for heating was examined and the consumption costs for 1 kWh heating and the energy calculations in case of heating for 6 hours were made. The cost of the thermal energy storage system is calculated from the night tariff price. Table 2 shows the pricing of electricity and other fuels in the last 10 years between 2012-2022. Prices do not include additional payments such as taxes and distribution fee [10,12].

When Table 2 is examined, it is seen that electricity prices have increased in 10-year time change, and the price change for night and single time in all years except 2022 is between 55.98% and 62.42% [13]. In the 3-time tariff, it is seen that the price change is between 55.70% - 59.57% for day and night time, and the price change for night and peak times is between 75% - 77.51%. In the 2022 tariff, in

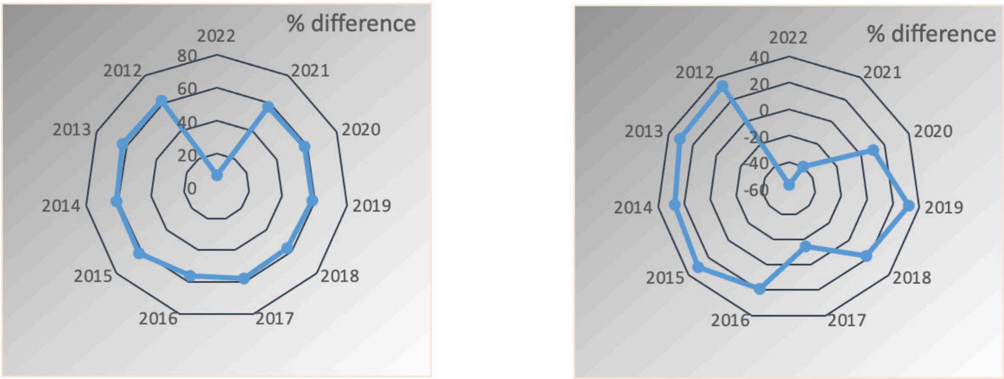

a) Electric b) Natural gas

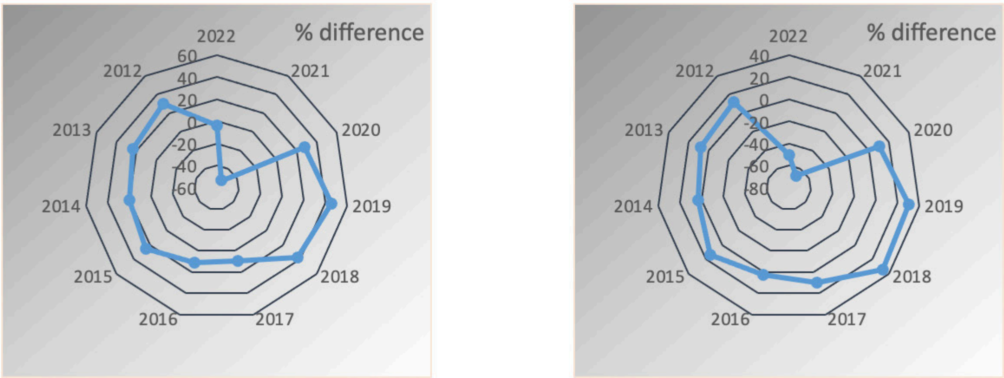

c) Imported coal d) Coal

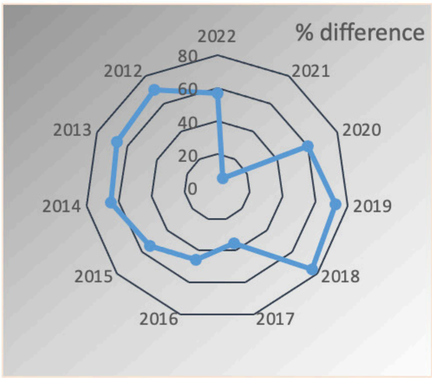

e) Fuel oil

Figure 4. Cost differences of other fuels compared to thermal energy storage system

case of consumption below 8 kWh per day, it is observed that there is little difference (6.97%) between night and single time, 46.06% during night and day, and 65.77% in night and peak change. In the case of a daily consumption of more than 8 kWh, it is observed that it is 45.20% between night and single time, 46.06% during night and day, and 65.77% at night and peak change. The prices of all other fuel types have increased over the years, and the nighttime electricity tariff is 10%-39% compared to natural gas, 9.5%-52% for imported coal, 9.5%-67% for domestic coal, and 35% -76% for fuel oil.

If the space is heated with different fuels for 6 hours, the cost calculations according to the price change for 10 years are shown in Figure 3. In all billings up to 2021, it is seen that the thermal energy storage system is very economical, and the most expensive system is heating with electricity. It is seen that the cost difference for the two systems is around 55-62% in all years except 2022. (Figure 3). In the calculations made for the year 2022, it is seen that the consumption above and below 8 kWh is the effective parameter. Since the daytime and nighttime prices are close to each other for consumptions below 8 kWh, it is seen that an electric heater can be used instead of the energy storage system. The cheapest heating system is the natural gas system. Above 8 kWh, natural gas and coal make more economical heating.

As seen in Figure 4, when the thermal energy storage system used in the night tariff is compared with electricity, it is seen that the system has an advantage of 60% in all years, and the system is usable in terms of hours and price.

Compared to natural gas, it is seen that the energy storage system is 20%-30% cheaper

until 2019, and between 2020-2022, natural heating is 40%-57% cheaper. When imported and domestic coal are examined, it is seen that energy storage systems are advantageous at rates ranging between 2%-45% (imported coal 11-45%, domestic coal 2%-30%) until 2021, due to the increasing electricity prices in 2021-2022. It is seen that coal is less costly over the years. Fuel oil, which is imported and always expensive among fuels, is expensive in the range of 35-76% compared to electricity and seems to be the most disadvantageous system in terms of usability.

4. Conclusions

As can be seen from the results, energy costs are increasing for all fuels every year in our country as well as in the whole world. It is seen that the heating costs of the heat storage system and the electric heater are the same for consumptions below 8 kWh, and natural gas is more advantageous than these systems. In consumptions above 8 kWh, it is seen that the heat storage system is more advantageous than electricity heating, but it is also expensive compared to other heating systems. In order for these systems to be used effectively and in accordance with their purpose, it is obligatory to rearrange the peak and night tariffs and to provide incentive price updates.

5. Acknowledgements

The Sivas Cumhuriyet University's Scientific Research Projects Unit (SCUBAP) provided funding for this work under the terms of project M-787. We would like to thank SCUBAP for their support

6. References

[1] Eames P., Loveday D.,Haines V., Romanos P. (2014). The Future Role of Thermal Energy Storage in the UK Energy System, U.K. Energy Research Center.

[2] International Energy Agency (2021), Electricity Market Report.

[3] https://www.gensed.org/basin/tei%CC%87as-2021-aralik-ayi-kurulu-guc-raporunu-yayinladi

[4] https://enerji.gov.tr/eigm-yayinlar

[5] Guizhi X., Xiao H., Zhirong L., Chao X., Cenyu Y., Zhanfeng D. (2018). Experimental And Numerical Study Of An Electrical Thermal Storage Device For Space Heating, Energies, 11, pp.2180.

[6] Syed, A.M. (2011). Electric Thermal Storage Option For Nova Scotia Power Customers: A Case Study Of A Typical Electrically Heated Nova Scotia House, Energy Engineering, 108:6, pp.69-79.

[7] Hughes, L., (2010). Meeting Residential Space Heating Demand With Wind-Generated Electricity, Renewable Energy, 8:35, pp.1765-1772

[8] Bedouani B.Y., Moreau A, Parent M., Labrecque B. (2001). Central Electric Thermal Storage (ETS) Feasibility For Residential Applications: Part 1. Numerical And Experimental Study, International Journal of Energy Research., 25, pp. 53-72.

[9] Bedouani B.Y., Labrecque B., Parent M., Legault A. (2001). Central Electric Thermal Storage (ETS) Feasibility For Residential Applications: Part 2. Techno-Economic Study, International Journal of Energy Research., 25, pp. 73-78.

[10] https://www.epdk.gov.tr/Detay/Icerik/3-1327/elektrik-faturalarina-esas-tarife-tablolari

[11] Turkish Electricity Distribution Corporation (TEDAS) 9th Regional Directorate, http://www.tedas.gov.tr

[12] https://www.dosider.org

[13] Fertelli A. (2022). Energy Storage Systems and Applicability for Buildings, I. Interdisciplinary Approaches Natıonal Congress, Istanbul, Turkiye.

EUROPEAN MECHANICAL SCIENCE
e-ISSN: 2587-1110

RESEARCH ARTICLE

Volume fraction of retained austenite in 1.2842 tool steel as a function of tempering temperature[§]

Ender Günerli[1], Melih Bayramoğlu[2*], Necdet Geren[2]

[1]ADOCIM TITAN Cement Company SA, Turkey
[2]Mechanical Engineering Department, The University of Cukurova, 01330 Adana, Turkey

Orcid: E. Günerli (0000-0002-2373-5603), M.Bayramoğlu (0000-0002-5152-3798, N. Geren (0000-0002-9645-0852)

Abstract: Untransformed austenite during quenching process is known as retained austeinite. The quantitative determination of the retained austenite is of great importance to the steel mechanical properties. Its percentage has a large effect on the mechanical properties and service life of components. The amount of retained austenite in through-hardened tool steels should be kept at its optimum level in order to minimize size change, and increase service life. In this study, the influnce of tempering temperature on the amount of retained austenite was evaluated by using X-ray diffraction phase analyses. It was seen that tempering at low temperatures resulted in small amount of retained austenite for the studied steel.

Key Words: Tool steel, Tempering temperature, X-ray diffraction, Retained austenite

1. Introduction

Tool steels are quenched and tempered at different conditions depending upon the type of steel being used and service requirements. The quenching and tempering operations increase the toughness and strength of the material for better service life. The selection of the proper tool steel and the application of the proper heat treatment processes affect the performance of the tools used in engineering applications. [1].

The microstructure of hardened tool steels made up of martensite and retained austenite (RA) when these are quenched to the room temperature. This may be either undesirable or desirable depending upon the application and amount of retained austenite. In some type of applications, the mixture of retained austenite and martensite are desirable due to compensation of the adverse effects of these phases. The amount of retained austenite depends on the chemical composition, austenizing temperature, quenchant temperature, tempering temperature and subsequent mechanical treatments. Generally, a small amount of retained austenite may cause increase in ductility and toughness, but too much retained austenite adversely affects the dimensional stability mechanical properties of steel components. For example, retained austenite at a certain level could be helpful to increase service performance when it is present in the carburized cases of gear teeth.

On the other hand, unstable retained austenite is not desired for components used in the tool and die industry. It leads to a short service life due to the loss of strength, hardness and dimensional stability in fully hardened tool steels [2-4]. Therefore, it is important to control the percentage of retained austenite in order to get optimum service life and mechanical properties for a given application [5-7].

Tolerable amount of retained austenite depends on the type of steel and service conditions. However, it is difficult to define exactly the tolerable amount of retained austenite due to insufficient data [3]. To solve this problem, each research in this aspect has been concentrated to find the effect of untransformed austenite on the performance of a specific steel in service.

These studies generally were concentrated on the evaluation of the effect of retained austenite formed at various heat-treating conditions on the mechanical properties and to find the optimum heat treating conditions and/or composition lead to a better service life for a given application [8-10].

Optical microscopy, scanning electron microscopy, transmission electron, magnetic methods, dilatometer, Mossbauer spectroscopy and X-ray diffraction (XRD) techniques are the common methods that have been used to determine the amount of RA include [11-13]. The suitable method is usually selected based on the percentage of retained austenite, level of accuracy and type of mate-

---

* Corresponding author.
Email: bayramog@cu.edu.tr

European Mechanical Science (2022), 6(4): 263-268
https://doi.org/10.26701/ems.1186751
Received: October 10, 2022 — Accepted: November 07, 2022

[§] This article was produced from the master thesis.

rial. With the development of diffractometer technology, quantitative determination of retained austenite content in heat-treated steels by x-ray diffraction has provided a reliable means of controlling properties and ensuring quality [14]. XRD methods are generally gives accurate measurements. This method can used to determine the amount of retained austenite to 0.5% level [15].

In this study, the effect of tempering temperature on the amount of retained austenite was investigated for the hardened 1.2842 (O2) cold work tool steel. X-ray diffraction method was used to estimate the volume fraction of retained austenite in as quenched and tempered specimens. At different tempering temperatures, volume fractions of retained austenite were estimated. Then, obtained results were interpreted to evaluate the influece of tempering temperatures on the volume fractions of retained austenite.

2. Determination of Retained Austenite Content

X-ray diffraction is one of the primary techniques used for the determination of retained austenite in steel. It is based on observing the scattered intensity of an X-ray beam hitting a sample as a function of incident and scattered angle, polarization, and wavelength or energy. One of the most commonly used method to calculate volume fraction of retained austenite is the direct comparison method based on a direct comparison of integrated intensities from each phase. In this method, the austenite fraction is determined from the ratio of the austenite and ferrite diffraction peak intensities and the values of R for each phase [16].

The following expressions needed for the determination of RA phase in steel are given in the American Society for Testing Materials (ASTM) based on direct comparison method. It is a standard practice for X-Ray determination of RA in steel with near random crystallographic orientation. In this practice, if possible, X-ray diffraction peak interference from other crystalline phases such as carbides should be eliminated from the ferrite and austenite peak intensities.

It has been stated that [17], "for a randomly oriented sample, quantitative measurements of the relative volume fraction of ferrite and austenite can be made from X-ray diffraction patterns because the total integrated intensity of all diffraction peaks for each phase is proportional to the volume fraction of that phase. If the crystalline phase or grains of each phase are randomly oriented, the integrated intensity from any single diffraction peak (hkl) crystalline plane is also proportional to the volume fraction of that phase". Based on the ASTM E975-03, for steel containing ferrite (α) and austenite (γ), the ratio of integrated intensity is given by Eq. 1.

$$\frac{{I_\alpha}^{hkl}}{{I_\gamma}^{hkl}} = \left(\frac{{R_\alpha}^{hkl}}{{R_\gamma}^{hkl}}\right)\left(\frac{V_\alpha}{V_\gamma}\right) \qquad (1)$$

Eq.1 holds, if ferrite (or martensite) and austenite are the only two phases present (Vα+Vγ =1) in a steel and both phases are randomly oriented.

The volume fraction of austenite (Vγ) for the ratio of measured integrated intensities of ferrite and austenite peak to R-value can be found using Eq. 2.

$$V_\gamma = \left[{}^{I_\gamma}/_{R_\gamma} \Big/ \left({}^{I_\alpha}/_{R_\alpha}\right) + \left({}^{I_\gamma}/_{R_\gamma}\right)\right] \qquad (2)$$

For numerous ferrite and austenite peaks, each ratio of measured integrated intensity to R-value can be summed up in Eq. 3.

$$V_\gamma = \left[\left(\frac{1}{q}\,\Sigma_{j=1}^{q}\frac{I_{\gamma j}}{R_{\gamma j}}\right)\Big/\left(\frac{1}{p}\,\Sigma_{i=1}^{p}\frac{I_{\alpha i}}{R_{\alpha i}}\right) + \left(\frac{1}{q}\sum_{j=1}^{q}\frac{I_{\gamma j}}{R_{\gamma j}}\right)\right] \qquad (3)$$

Rα and Rγ are the theoretical intensities and they can be calculated by using Eq. 4.

$$R^{hkl} = \frac{1\left(|F|^2 pLPe^{-2M}\right)}{v^2} \qquad (4)$$

Where;

$|F|^2$: structure factor times its complex conjugate,

p : multiplicity factor of the (hkl) reflection,

LP : Lorentz Polarization factor and equals to [(1 + cos22θ)/sin2θ cosθ] where θ is Bragg angle,

e-2M : Debye-Waller or temperature factor which is a function of θ,

v : volume of the unit cell.

3. Material and Method

3.1. Material

The commercial 1.2842 (AISI O2) cold work tool steel was used in this work Cold work tool steels contain high amount of carbon steels and relatively low amonut of alloys. The chemical composition of the steel used in this study is given in Table 1.

This group of steels is relatively inexpensive, and they are widely used for blanking and forming dies that require high surface hardness and minimal distortion during hardening.

3.2. Heat Treatment Process

Hardening and tempering processes have been carried

Table 1. Chemical composition of 1.2842 steel used in the experiments

C %	Si %	Mn %	Cr %	Mo %	Ni %	V %	W %	P %
0.90	0.25	2.00	0.40	-	-	0.10	-	0.03

Table 2. The selected heat treatment conditions for 1,2842 Steel.

	Temperature (°C)	Time (h)	Medium
Stress Relieving	400	2	Furnace
Hardening	820	0.5	Oil
Tempering	150	1.5	Still air
	200		
	250		
	300		
	400		

out, under the conditions listed in Table 2, according to the technical specification suggested for the heat treatment of 1.2842 steel [18].

Stress relief annealing heat treatment (at 400°C for 2h) is applied to all samples before the quenching process. Then, samples were austenitized at 820°C for 30 minutes and quenched in oil. The samples were stress relieved again before the tempering process at a temperature of 150°C to avoid any crack and distortion. Then, the samples were tempered at different tempering temperatures for 1.5 hours in an electrical muffle furnace and allowed to cool in still air.

3.3. X-ray Diffraction Phase Analyses

XRD phase analyses were performed by using Rigaku Miniflex 2 Benchtop diffractometer (shown in Figure 1) with 40 kV tube voltage, 15 mA tube current.

Six specimens tempered at different temperatures and a specimen as-quenched condition were used for X-ray diffraction phase analyses. The dimensions of each specimen,

Figure 1. Rigaku Miniflex 2 Benchtop diffractometer

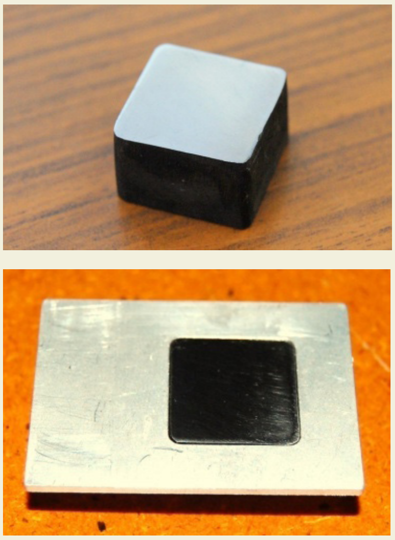

Figure 2. The picture of test specimen and the holder used for XRD phase analyses.

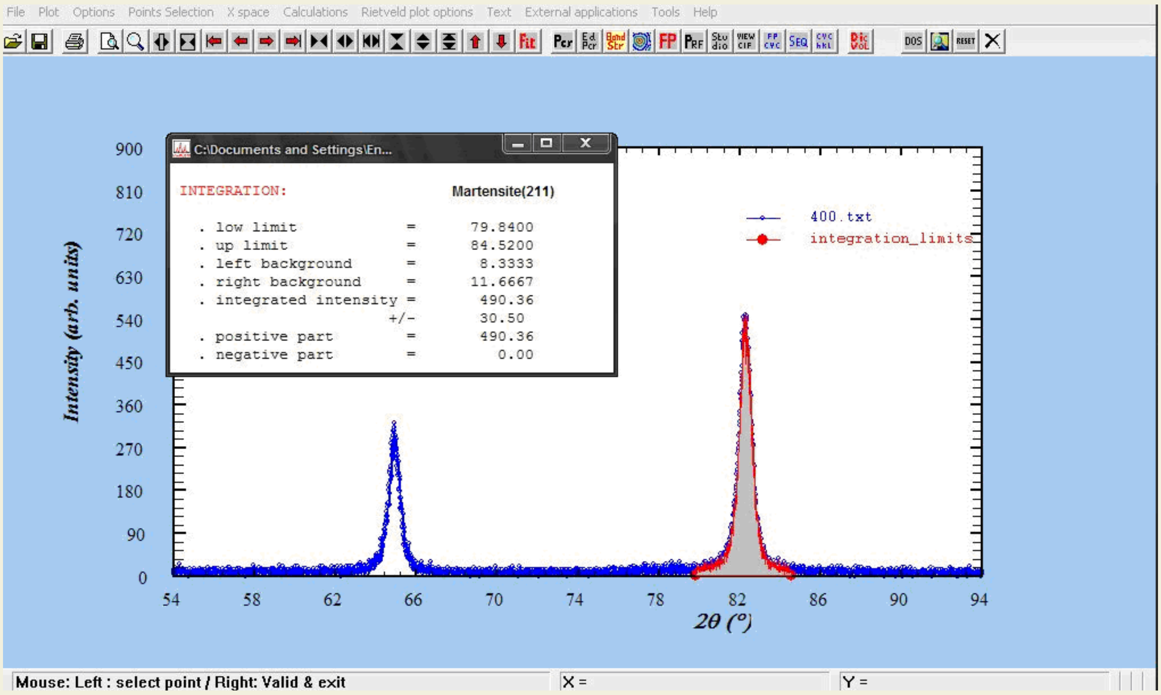

```
INTEGRATION:                          Martensite(211)

  . low limit              =     79.8400
  . up limit               =     84.5200
  . left background        =      8.3333
  . right background       =     11.6667
  . integrated intensity =      490.36
                        +/-      30.50
  . positive part          =    490.36
  . negative part          =      0.00
```

Figure 3. An example of XRD pattern of the tempered sample obtained from WINPLOTRTM software and integrated intensities of each peak.

shown in Figure 2, were 20x20x12 mm. The impruties on face of samples were removed by applying grinding and polishing. Then, each speciemen was located into the holder and subjected to x-ray to obtain XRD patterns for the specimens.

The phases represented by each peak were defined according to the Joint Committee on Powder Diffraction Standards (JCPDS) peak lists. In this study the (200) α, (211) α, (220) γ and (311) γ peaks and their integrated intensities (Iα200, Iα211, Iγ220, and Iγ311) were compared with JCPDS peaks for the definition of the phases obtained in each sample after tempering. WINPLOTRTM software was used to determine the integrated intensities from the XRD patterns by calculating the area under the X-ray diffraction peaks as shown in Figure 3.

The volume fraction of retained austenite (Vγ) was estimated by substituting calculated R values into Eq. 5, which is derived from Eq. 3 [19].

$$
{}_{\gamma} = \frac{\left(I_{\gamma}^{220} \Big/ \left(1.42 I_{\alpha}^{200} + I_{\gamma}^{220}\right)\right) + \left(I_{\gamma}^{220} \Big/ \left(0.71 I_{\alpha}^{211} + I_{\gamma}^{220}\right) + \left(I_{\gamma}^{311} \Big/ \left(1.62 I_{\alpha}^{200} + I_{\gamma}^{311}\right) + \left(I_{\gamma}^{311} \Big/ \left(0.81 I_{\alpha}^{211} + I_{\gamma}^{311}\right)\right)\right)\right)}{4} \qquad (5)
$$

Finally, the determined volume percentage of retained austenite were plotted as a function of tempering temperatures and results were interpreted in the following section.

4. Result and Discussion

During quenching process, all of the austinite obtained at the austenizing temperature is not transformed into martensite. Depending upon the final temperature reached during cooling stage, some of the austenine will not transform into martensite. Then the final structure consists of austenite transformed into martensite with some amount of untransformed austenite (RA). Mechanical properties of hardened tool steels can be altered during tempering process by controoling the amaunt of RA. In this work, the volume fraction of RA was calculated by comparing the integrated intensities in order to study the effect tempering temperatures on the volume fraction of RA. The results obtained from the calculations are given in Table 3. The same method was also used by Li et al [20]. They have estimated RA content by using the direct comparison techniqueu and they have investigated the effect of RA content on mechanical properties such as hardness and toughness of cold work tool steel. They reported that XRD peaks obtained in the XRD analyses were changed depending on the volume of retained austenite obtained at different tempering temperatures.

Patterns obtained from XRD analyses for as-quenched and tempered samples are presented in Figure 4..

As seen in Figure 4 (a), as-quenched samples were contained the highest volume of RA. Because compared to the XRD patterns of tempered specimens, (220)γ and (311)γ peaks at the 2θ values of about 75 and 90 degrees were hihgher that the (200)α and (211)α peaks obtained in the as-quenched samples.

As shown in Figure 4 (b), (220)γ and (311)γ peaks are lower in compared to (200)α and (211)α peaks and (200) α and (211)α peaks are higher in tempered samples compared to the as-quenched samples. This inidicates that the amount of untransformed austenite content decreases in the saples tempered at the temperature of 150°C.

Similarly, increasing the tempering temperature from 150 to 200°C (Figure 4 c) resulted higher amount of RA. Above the tempering temperature of 200°C, significan decrease was observed at the (220)γ and (311)γ peaks and austenite peaks were not seen very clearly. Almost non-existent austenite peaks are observed in Figure 4 (d), (e) and (f). The reason for extinction after tempering temperature of 200°C is due to the dcrease in the amount of RA

Volume fractions of RA estimated from the X-ray diffraction analyses based on the comparison method are summarized in Figure 5.

As shown in Figure 5, the highest amount of retained austenite (about 11.80%) was obtained after the quenching process. The samples tempered at about 150°C caused a reduction in the amount of RA (about 8.45%). It could be said that the formation of very fine particles of epsilon

Table 3. Integrated intensities and the volume fractions of RA obtained at different heat treating conditions

Tempering at (°C)	I_{α}^{200}	I_{α}^{211}	I_{α}^{220}	I_{α}^{311}	V_{α}	RA, % Vol.
As quenched	137.71	213.6	22.24	26.88	0.118	11.80
150	217.54	406.71	29.72	28.98	0.08448	8.45
200	108.16	203.88	18.24	17.25	0.10056	10.06
250	178.31	345.46	6.94	12.06	0.0339	3.39
300	193.04	359.4	6.13	5.59	0.02043	2.04
400	257.02	490.36	3.61	3.76	0.0096	0.96

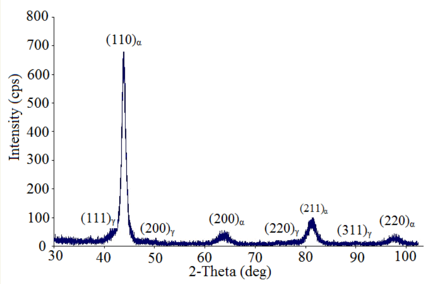

(a) As quenched

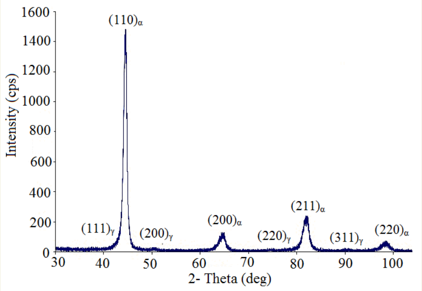

(b) Tempered at 150 °C

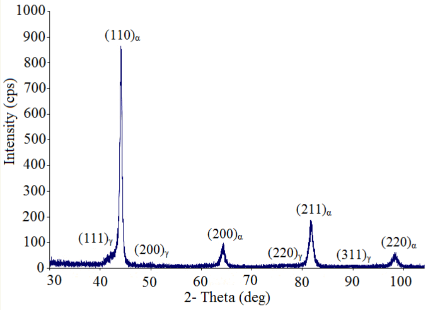

(c) Tempered at 200 °C

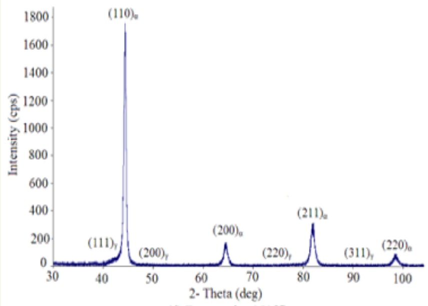

(d) Tempered at 250 °C

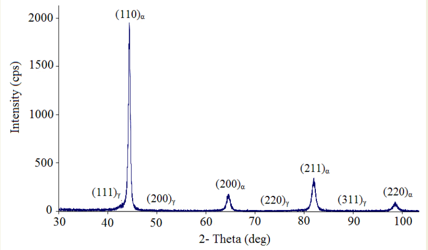

(e) Tempered at 300 °C

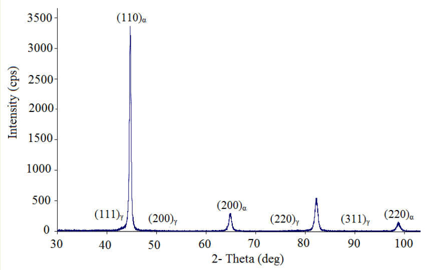

(f) Tempered at 400 °C

Figure 4. XRD Patterns of as-quenched specimen and specimens tempered at different temperatures

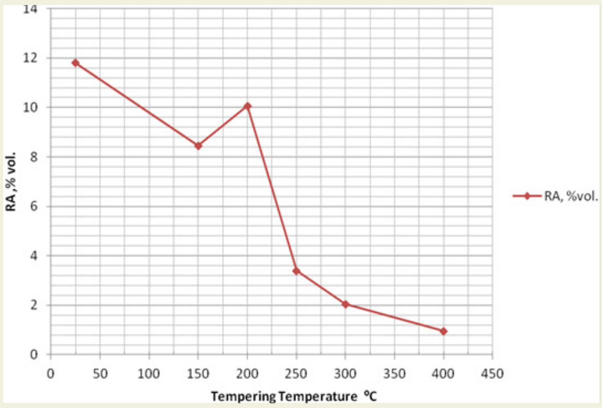

Figure 5. The effect of tempering temperatures on the volume fraction of RA

(hexagonal) carbide as a result of supersaturated carbon precipitation out of the martensite caused the reducion in the volume of RA content up to the tempering temperature of 150°C. Increasing tempereing temperature from 150°C to 200°C resulted a slight increase (about 10.06%) in the amount of RA content. In this tempering temperature range, a slight increase of RA volume was observed due to the decomposition of carbide which resulted the stabilization of austenite. A sharp reduction of RA is observed between the tempering temperatures of 200 °C and 250°C. Amonut of RA continued to decrease in the samples tempered above the temperature of 250 °C.

RA volume dropped suddenly above the tempering temperature of 200°C due to the thermal destabilization of this phase [21]. As stated by Dong et al. [9], Kokosza and Pacyna [22] and Talebi et al [23], after the tempering temperature of 200°C, untransforfed austenite within the structure could be decomposed by a diffusion mechanism and causes precipitation of more carbides. This causes reduction in the austenite stability and results the transformation of austenite to a hard martensitic structure during the cooling process. This could be the reason for the sharp reduction in the amount of RA and carbon concentration of retained austenite. The reduction in the amount of RA was continued when the tempering temperature was increased and nearly no RA was seen at about tempering temperature of 400 °C.

5. Conclusion

Characterization of the RA in quenched and tempered 1.2842 tool steel was evaluated by using XRD phase analyses. The samples were quenched at 820 °C and tempered for 1.5 h at 150 °C, 200 °C, 250 °C, 300 °C and 400 °C. The the amount of RA was calculated for each sample and the results were presented. Following conclusions were drawn from the XRD analses carried out for the quenched and tempered 1.2842 steel.

About 11.8 % of RA was observed in the as-quenched 1.2842 steel. Increasing tempering temperature to 150 °C resulted a reduction in the amount of RA to 8.45 % level. Amount of RA (10.06 %) started to increase again when the tempering temperature was increased to 200 °C. Above the tempering temperature of 200 °C, the thermal destabilization of austenite resulted a gradual reduction in the amount of RA. Very small amount of RA (0.96 %.) was observed athe samples tempered at about 400 °C.

6. Acknowledgments

The authors would like to thank the Scientific Research Projects Coordination Unit (BAP) of Cukurova University in Adana, Turkey for the financial support provided. Project No: MMF2012YL15

7. References

[1] Broyson ,W.E. (2015), Heat treatment, selection, and application of tool steels 2nd ed., Hanser Publishers, Munich.

[2] Li, J., Feng Y., Tang, L., Wu, X. (2013), FEM prediction of retained austenite evolution in cold work die steel during deep cryogenic treatment, Materials Letters, 100,. 274-277, doi:10.1016/j.matlet.2013.03.046

[3] Vander, G. F. (2009), Martensite & retained austenite, Industrial Heating, 76, 51-52

[4] Wiewiorowska, S., Muskalski, Z. (2016), Effect of the die approach zone shape on the transition of retained austenite and the mechanical properties of TRIP steel wires, Materials Testing, 58, No. 4, pp. 302-305, doi:10.3139/120.110852

[5] Abdulkareem, N.M., Jabbar, M.A. (2017), Micro-structure and Mechanical Properties of AI-SI4340 High Strength Low Alloy Steel (HSLA steel) Using Magnetic Saturation Measurement and X-Ray Diffraction methods, Basrah Journal for Engineering Sciences, 17(2) , 1-8

[6] Zhang, M.X., Kelly, Bekessy, L.K., Gates, J.D. (2000), Determination of retained austenite using an X-ray texture goniometer, Materials Characterization, 45 (1), pp. 39-49, doi:10.1016/S1044-5803(00)00044-9

[7] Kumar, R., Dwivedi, R.K., Ahmed, S. (2021), Stability of retained austenite in carbide free bainite during the austempering temperature and its influence on sliding wear of high silicon steel, Silicon 13, 1249–1259, DOI:10.1007/s12633-020-00513-2

[8] Zou, D., Han, Y., Zhang, W., Fang, X. (2010), Influence of tempering process on mechanical properties of 00Cr13Ni4Mo super martensitic stainless steel, Journal of Iron and Steel Research International, 17 (8), 50-54, doi:10.1016/S1006706X(10)60128-8

[9] Murathan, Ö.F., Davut, K., Kilicli, V. (2021), Effect of austenitizing temperatures on the microstructure and mechanical properties of AISI 9254 steel, Materials Testing, 63 (1), 48-54, doi:10.1515/mt-2020-0007

[10] Bakhshi, S., Asadabad, M. A., Bakhshi, S. (2022), Influence of the heat treatment on the quantitative features of the fracture surfaces and the mechanical properties of AISI 4340 steel sheets, Ironmaking & Steelmaking, 1-15, doi: 10.1080/03019233.2022.2107111

[11] Wu, D., Qi, J.G., Li, Y., Qiu, H. (2015), Determination of retained austenite content in Fe–Cr–Ni weld metal, Materials Research Innovations, 19 (5), 410-414, doi:10.1179/1432891714Z.0000000001120

[12] Ferreira, H.C., Boratto, F.J.M, , Buono, V.T.L. (2015), Determination of low levels of retained austenite in low-carbon high-manganese steel using X-ray diffraction, Materials Science and Engineering: A. 628, 110-115, doi:10.1016/j.msea.2015.01.019

[13] Sharmaa, S., A. Hegde, A. (2021), An Analysis of the Amount of Retained Austenite in Manganese Alloyed Austempered Ductile Iron , Materials Research. 24(6), 1-6, doi: https://doi.org/10.1590/1980-5373-MR-2021-0301

[14] Cui, C., Dong, J., Epp, j., Schulz, A., Steinbacher, M., Acar, S., Herbst, S., Maier, H.J. (2021), In Situ X-Ray Diffraction Analysis of Microstructure Evolution during Deep Cryogenic Treatment and Tempering of Tool Steels, Steel Reseach Int. 92(12), 1-9, https://doi.org/10.1002/srin.202100076

[15] Magner, S. H., De Angelis, R. J., Weins, W. N., Makinson, J. D. (2002), A historical review of retained austenite and its measurement by x-ray diffraction, JCPDS Advances in X-Ray Analysis 45, 92-97

[16] Cullity, B.D. (1978), Elements of X-ray diffraction, 2nd ed., Addison-Wesley Publishing Company Inc., Phillippines.

[17] ASTM E975-03, (2013), Standard practice for X-ray determination of retained austenite in steel with near random crystallographic orientation, ASTM International

[18] Ko K.K., Jang, J.H., Tiwari S, Bae H.J., Sung, H.K., Kim, J.G., Seol. J.B. (2022), Quantitative analysis of retained austenite in Nb added Fe-based alloy. Applied Microscopy, 52(1):5,1-10, doi: 10.1186/s42649-022-00074-1.

[19] Kim, S., Lee, Y. (2011), Effect of retained austenite phase on springback of cold-rolled TRIP steel sheets, Materials Science and Engineering: A 530, 218-224, doi:10.1016/j.msea.2011.09.077

[20] Li, S., Deng, Y., Wu, X., Wang, H., Min, Y. (2010), Effect of deep cryogenic treatment on internal friction behaviors of cold work die steel and their experimental explanation by coupling model. Materials Science and Engineering: A 527 29, 7950-7954, doi:10.1016/j.msea.2010.08.086

[21] Gunerli, E. (2012), Effect of tempering temperature on the mechanıcal propertıes of hardened 1.2842 tool steel, MSc diss., University of Cukurova.

[22] Euser, V. K. (2021), The Role of Retained Austenite in Tempered Martensite Embrittlement of 4340 and 300-M Steels Investigated through Rapid Tempering" Metals 11, no. 9: 1349. https://doi.org/10.3390/met11091349

[23] Talebi, S.H., Jahazi, M., Melkonyan, H. (2018), Retained Austenite Decomposition and Carbide Precipitation during Isothermal Tempering of a Medium-Carbon Low-Alloy Bainitic Steel, Materials (Basel), 11(8):1441. doi: 10.3390/ma11081441.

EUROPEAN MECHANICAL SCIENCE

e-ISSN: 2587-1110

RESEARCH ARTICLE

Wind energy and assessment of wind energy potential in Turkey: A case study for Mersin province

Metin Dağtekin[1*], **Bekir Yelmen**[2]

[1]Ceyhan Technical College, Cukurova University, Ceyhan-Adana, Turkey.
[2]Department of Environmental Protection Control Adana Metropolitan Municipality, Adana, Turkey.

ORCID: M. Dağtekin (0000-0002-1397-1725) B. Yelmen (0000-0001-7655-530X)

Abstract: Today, decrease in fossil resources and the ever increasing need for energy increases the importance of renewable energy resources. Wind power; It has an important potential and usage area in clean and renewable energy sources. The measurement of wind speed and direction values is very important in terms of evaluating the data of wind power plant (WPP) project and estimating the amount of energy that can be produced. Wind energy is a good example of clean energy source due to its advantages such as cleanness fast commissioning, and reliability. There has been a significant increase in recent years especially in terms of utilizing wind energy. By the end of 2016, the installed wind power capacity in the world is 486749 MW, Turkey takes the 11th place with 6081 MW of installed capacity. In this study, the use of wind power in Turkey's Mersin province were studied. Mersin province in terms of installed wind power capacity has an important place in Turkey. As of 2016, the installed wind power capacity throughout the province is 364 MW, but the usable wind energy potential in the region is about 3414 MW.

Keywords: renewable energy; wind energy; wind power plant, Mersin

1. Introduction

The rapid growth of the population and industrialization have increased the demand for renewable energy sources all over the world due to insufficient fossil fuel energy resources. Accordingly, wind energy as a renewable energy source has attracted attention because of its sustainability, efficiency, and cleannes. As a result, worldwide wind power plant (WPP) investments have increased in recent years [1]. The fact that fossil energy resources will be depleted in the future, cause environmental pollution and depend on the countries where these resources are located, has increased the demand for renewable energy sources [2]. Energy production is one of the basic requirements for development in industrialized societies. Today, industrialized countries obtain approximately 65% of their energy from fossil fuels. Researches indicate that developed countries will realize 50% of world energy production by 2030 [3]. While the depletion times of the world's energy reserves are approximately 200 years for coal, 65 years for gas and 40 years for oil, this period is endless for wind energy [4]. The energy consumption rate in the world is 300 thousand times the formation rate of fossil fuels [5]. Regarding the history of wind turbines, it is estimated that the oldest wind power machine, the windmill, was built near Alexandria 3000 years ago [6]. Renewable energy sources are sources that reduce external dependency, help protect the environment and do not harm humanity. In addition, these energy resources, which are not consumed in nature, have the characteristics of accessibility, availability and acceptability [7]. Renewable energy sources can contribute to development thanks to business and infrastructure opportunities in rural and underdeveloped areas such as mountainous regions. Although the businesses of renewable energy sources projects are

Figure 1. A photo of Wind power plant

---

[*] Corresponding author.
Email: mmdagtekin@gmail.com

European Mechanical Science (2022), 6(4): 269-277
https://doi.org/10.26701/ems.1174354
Received: September 12, 2022 — Accepted: November 07, 2022

cheap, initial investment costs are higher than fossil-based technologies [8] [9]. There are some advantages of wind energy, which is renewable. There is no transportation problem and it does not require high technology to use at the same time. It is abundant and freely available in the atmosphere, a clean energy source that is easy to obtain and has no environmental pollution. The photograph, given in Fig. 1, shows operational wind turbines [10].

In the active use of this energy in the world, Germany has set a target in a short time and plans to obtain 50% of its energy from the wind in 2050. Regarding wind energy use, Japan shows similarity with Germany. The common goal of European countries in the 2020s is to meet 20% of their energy needs from wind energy [11]. In our country, wind energy investment was first made in 1998 in Çeşme (8.7 MW). In 2000, only an investment of 10.2 MW was made in Bozcaada. Rapid industrialization in Turkey, a large amount of energy is causing the deficit between supply and demand. Turkey imports approximately 72% of energy sources [12]. Turkey is a very rich country in terms of wind potential. If the wind is converted to energy, big gains can be obtained [13] [14]. Prepared jointly by the Electrical Works Survey Administration (EIE) and the State Meteorological Service (SMS) and published in June 2002; Turkey Wind Atlas is providing a hope in this regard [15]. According to the State Planning Organization Electric Energy Special Commission (2001), the potential mentioned in the work of the Electrical Works Survey Administration is about 10000 MW [16] [17]. Investments in wind energy have been increased especially in recent years; Because investments such as wind energy provide a significant advantage due to the limited resources such as natural gas and coal and being dependent on foreign sources [18]. According to Wind Map of Turkey, the regions with the greatest wind potential is given in Tab. 1.

In Turkey, it is estimated that a wind power plant with a power of 5 MW .km^{-2} can be built in areas with 50 meters above ground level and at least 7.5 m . s^{-1} of wind speed;. Accordingly, Turkey wind energy potential figure is determined to be about 48000 MW. Wind power plants start generating electricity from 3 m . s^{-1} and continue to generate electricity up to 25 m . s^{-1} wind speed. When the wind map of Turkey is analysed, it can be seen that even the places receiving the least wind have more than 3 m . s^{-1} wind potential (Fig. 2) [20].

Table 1. Distribution according to the months SE total potential of Turkey[19]

Region	Average annual wind speed (m . s^{-1})	Annual average wind density (W . m^{-2})
Marmara Region	3.29	51.91
Aegean Region	2.65	23.47
Mediterranean region	2.45	21.36
Central Anatolia Region	2.46	20.14
Black Sea region	2.38	21.31
Eastern Anatolia Region	2.12	13.19
Southeastern Anatolia	2.69	29.33
Region Average	2.58	25.82

In determining the wind energy potential of a region, statistical data obtained by processing raw data are used. Rayleigh and Weibull distributions are the most commonly used among statistical methods used for this purpose (Fig. 3) [21].

When the situation of Mersin province is analysed according to the latest data, it is seen that the wind power plants (WPP) in the enterprise come after Osmaniye and Çanakkale provinces in the installed power distribution according to the provinces (Fig. 4) [22]. In this context, it is seen that the existing potential is appropriate and started to be evaluated.

Gülersoy and Çetin have obtained the wind data from 2008 and 2009, by measuring hourly; They showed that the wind energy potential of Menemen is suitable for the production of electricity [23]. Intense population growth in Turkey, as in other developing countries, industrialization effort to increase investment and support for the development of technology; it increases the demand for energy day by day [2]. Arslan et al. analyzed the wind energy potential of a region located in the campus area of Kırıkkale University and whose wind speed was determined [24]. Yıldırım et al. analyzed the wind energy potential of Nigde province statistically [25]. With today's technology, wind energy is one of the most suitable renewable energy source. It is at a level to compete with conventional fossil fuels in suitable wind areas. Its cost also decreases as wind technology improves and usage areas increase. It is thought that, with the technological developments occurring in the wind energy sector, the costs of the wind turbine and its components decrease and the incentives given to the wind energy increase, it will gain importance

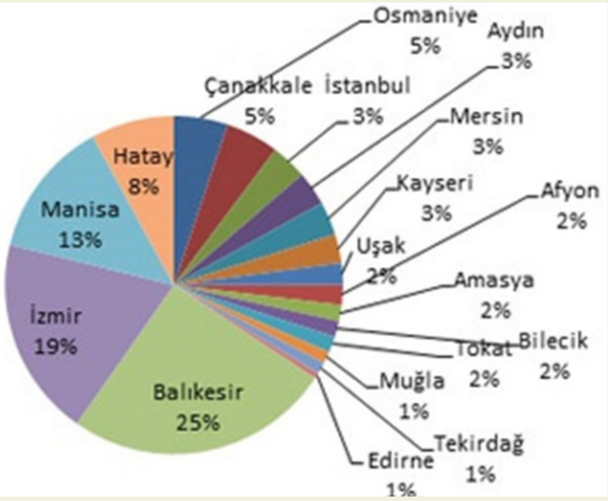

Figure 4. Distribution of wind power plants in the enterprise by provinces

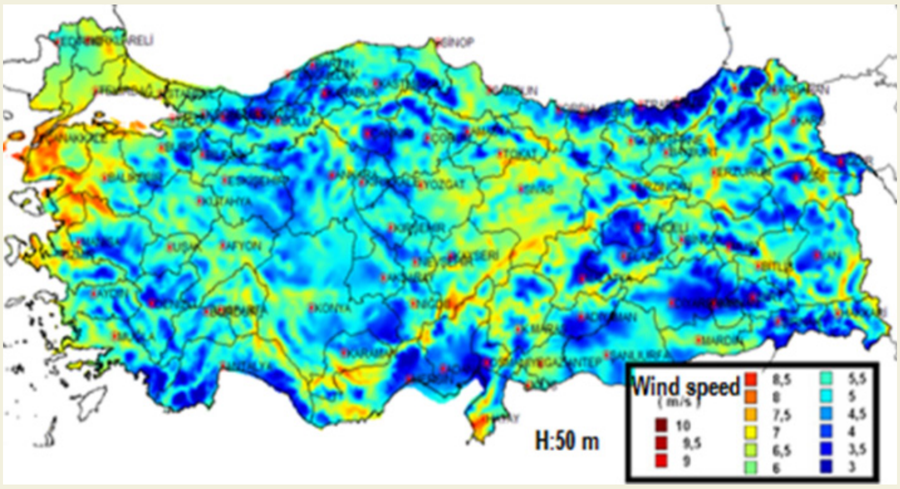

Figure 2. Turkey wind energy potential

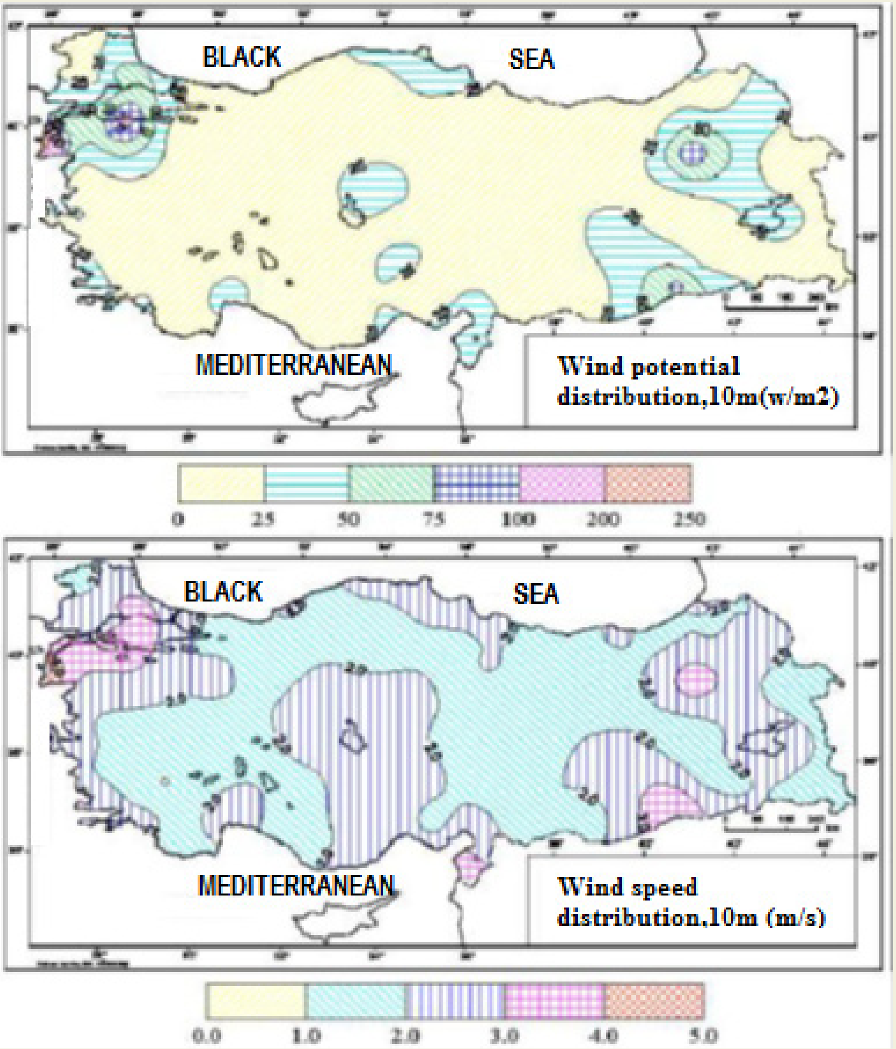

Figure 3. Wind potential distribution map (10 m)

in the investments to be made. Turkey has provided for 72% of the available energy supply from outside. This raises the issue of utilizing the potential of renewable energy sources to reduce this dependency. To analyse the wind energy potential of any region, hourly wind speed and direction information in that region should be measured for at least one year. Wind energy, Turkey's natural conditions and terms of energy production costs, is a potential that needs assessment. Turkey has an important place in terms of wind energy potential in Europe. As it is close to the regions where consumption is intensive and it has wind investments and potential, Çukurova region is one of the most important regions of the country, and with the development of the energy sector, it is an in-

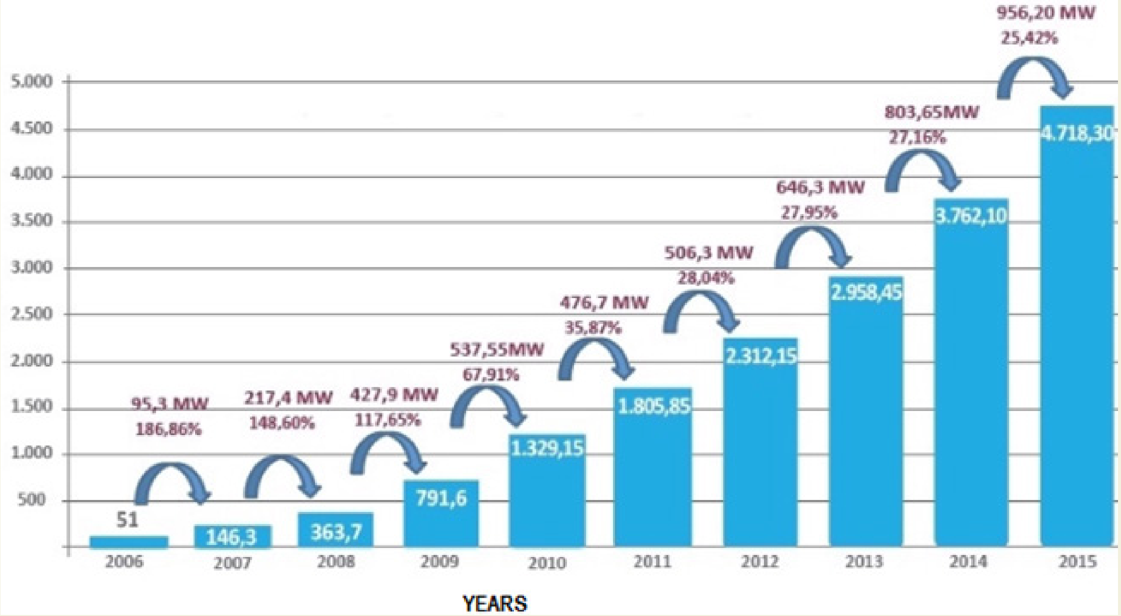

Figure 5. Cumulative installation for wind power plants in Turkey (MW)

creasingly important region. Mediterranean region with wind energy projects with 156 of them in the assessment stage is ranked third in Turkey. 7 of these projects are in Çukurova region. In addition to the land and wind structure, in the region; Considering that the industry is also developed, the Çukurova region means a new market for the wind energy sector. It is possible to express these developments in wind energy field with numerical data. In 2015, the global installed renewable energy power reached 913.48 GW and the installed power in the wind reached 428 GW. In 2015, the installed wind energy capacity of the European Union countries increased by 5.4 percent to 13805.3 MW. Turkey in terms of installed capacity, which ranks 10th in Europe, and was ranked 15th in the world. In addition, wind power plants, which were put into operation in 2015, have taken their place as the 10th largest market in the world with its installed power (Fig. 5) [26].

Table 2. Wind power plants (WPP) in operation

Project	Installed Power(M)	Province	Turbine Manufacture
Altik Belen WPP	18.0	Hatay	Gamesa
Belen WPP	48.0	Hatay	Vestas
Çerçikaya WPP	57.0	Hatay	ACCIONA
Dağpazarı WPP	39.0	Mersin	Siemens
Gökçedağ WPP	135.0	Osmaniye	GE
Hasanbeyli WPP	50.0	Osmaniye	Nordex
Hilal-2 WPP	9.9	Mersin	Vestas
Mersin MutWPP	42.0	Mersin	Vestas
Mut WPP	52.8	Mersin	Vestas
Sebenoba WPP	63.7	Hatay	Vestas
Senkoy WPP	36.0	Hatay	Alstom
Şenbük WPP	27.7	Hatay	Vestas
Şenbük WPP	38.1	Hatay	Vestas
Ziyaret WPP	76.0	Hatay	GE

Looking at the wind energy view; Turkey in terms of wind power installed capacity in the year 2015, 956 megawatt power plant was put into operation. While reaching 4718 megawatts in total; While 74 percent of the wind power plants in the circuit are located in the Aegean and Marmara regions, the Mediterranean Region is in the third place with a share of 9.85 percent. On the other hand, the total installed power of 88 licensed wind power plants, whose construction has not started, reaches 3144 megawatts. With its 174 megawatts of power capacity, the Mediterranean Region is in the fifth place. The total installed power of 61 Wind Power Plants, which is currently under construction, reaches 869 megawatts. The Mediterranean Region ranks third with 184 megawatts (Tab. 2) [26].

Wind speed data for Mersin province was obtained from the General Directorate of State Meteorology Affairs.

In this study, suitable areas were researched for the wind energy potential and for the establishment of a Wind Power plant (WPP) in Mersin region based on the hourly wind speed data measured. To focus on the elements necessary to increase the efficient use of this resource is to determine how we can utilize wind energy more efficiently with the national renewable energy policy to be regulated [27].

2. Materials and Methods

Mersin province is located in the southern part of Mediterranean coast (36° 48' It is in North Latitude and 34° 38 ' East longitudes). The settlement map of Mersin province

Figure 6. Location of Mersin on Turkey map

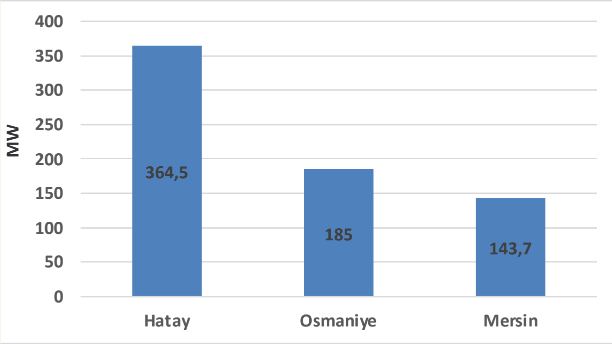

Figure 7. Distribution of WPPs in business in Çukurova region by province

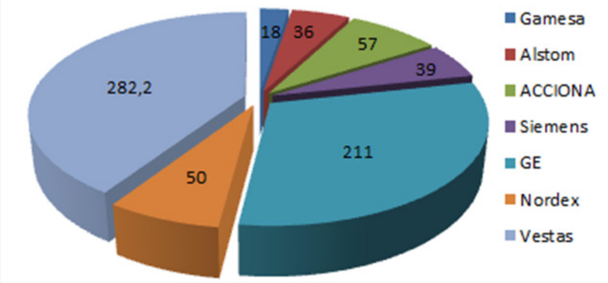

Figure 8. Distribution of WPs in the enterprise by turbine brands (MW)

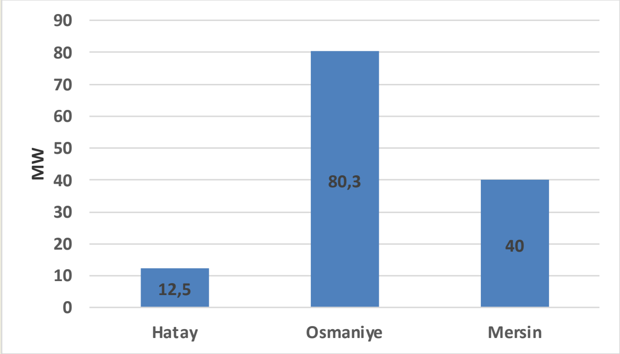

Fig. 9 The installed power (MW) distribution of WPPs in different provinces of Çukurova region

is shown in Fig. 6 [28].

Çukurova region, one of the most important area of the Mediterranean Region with a great potential in terms of wind energy. The developments in the electricity market have important repercussions on the Çukurova region. Distribution of WPPs in the service in the Çukurova Region by Provinces is shown in Fig. 7.

The region has an important potential in terms of wind, hydroelectricity and solar resources. Especially in Mersin, Gülnar, Mut and Silifke districts and Belen district of Hatay attract attention with their wind power plant investments. The installed power of the wind power plants, in operation, in the Çukurova region was 534.8 MW in 2014. In line with the 2015 data, it increased by 27% (149.4 megawatts). The cumulative installed power reached 693.2 MW. There are 14 wind power plants and 252 wind turbines in this region. The wind power plants of the region produce electricity that can meet the electrical energy needs of approximately 475601 houses. In 2015, Hatay took the first place with 87.5 MW and Mersin took the second place with an installed capacity increase of 62.7 MW. On the basis of provinces, Hatay is the fourth with 7.73%, Osmaniye is the seventh with 3.92% and Mersin is the 10th with 3.05%. It has been remarkable that Osmaniye and Mersin have risen one line lately. Distribution of WPPs in the enterprise by Turbine brands (MW) is shown in Fig. 8.

Vestas, which is among the turbine brands used in operating wind power plants in Çukurova, ranks first with 282.2 megawatts. While General Electric is in second rank with 211 MW, Acciona is in third rank with 57 MW. Apart from these turbine brands, turbine brands such as Alstom, Gamesa, Nordex and Siemens are also used in power plants. 75% Vestas at the plants commissioned in 2015, 25% Acciona brand turbines were used.

Mersin, Hatay and Osmaniye have more favourable areas for the establishment of wind power plants compared to Adana. This situation also explains the reason for the current location of WPP investments in these cities. Wind power plants, which were under construction in the Mediterranean Region in 2014, which were 177.3 megawatts, became 184 megawatts in 2015. At the same time, while the wind energy capacity in the Çukurova region, which was 98.18 megawatts in 2014, increased by 20% (24.62 megawatts) compared to the previous year, the capacity of 4 wind energy projects under construction in 2015 was 122.8 egawatts (Tab. 3).

The distribution of installed power (MW) of WPPs in different provinces of Çukurova region is shown in Fig. 9.

The total installed power of the three licensed WPP projects with approximately 47 MW, whose construction has not been started. With 33 MW of these projects, two are located in Hatay and one in Mersin. There are also two unlicensed WPP in the region. Two power plants with a total capacity of 1000 kW belongs to Baykal Energy Ltd. In addition, there are 1750 kilowatts of unlicensed WPP projects in the same city, with three project approvals. There are 156 wind energy projects in the evaluation stage in Turkey and 72 of these projects are in the region of Çukurova. It ranks third as the total power is considered. Wind Power Plants that are under evaluation are given in Fig. 10.

There are 10 projects with a total power of 275 MW in Hatay, 2 projects with 34 MW in Osmaniye and 41 projects with 1909 MW in Mersin. It is striking that the projects are concentrated in the districts of Mut, Gülnar and Silifke in Mersin, while in Hatay, they are concentrated in Yayladağı and the Center. Turkey Electrical Works Study Administration prepared wind map in cooperation with the State Meteorology Affairs General Directorate of Turkey for the evaluation of the wind energy potential. When the map and data are analysed, it is seen that Çukurova Region has a very rich potential in terms of wind energy. The annual average wind speed at the height of 10 m in the Mediterranean Region was 2.5 m . s^{-1} and the power density was 21.36 W . m^{-2}. Çukurova region, Turkey's wind energy power density of 20 W .m^{-2} not exceeding, has greater potential than 64.5%. In line with all

Table 3. Wind Power Plants Under Construction

Trade Name	Project	Installed Power (MW)	Province
Aksa Energy Products Inc.	Atik Belen WPP	12.5	Hatay
Zorlu Wind Products Inc.	Demirciler WPP	23.3	Osmaniye
Hanay Energy Products Inc.	Elmalı WPP	30.0	Mersin
Zorlu Wind Products Inc.	Sarıtepe WPP	57.0	Osmaniye

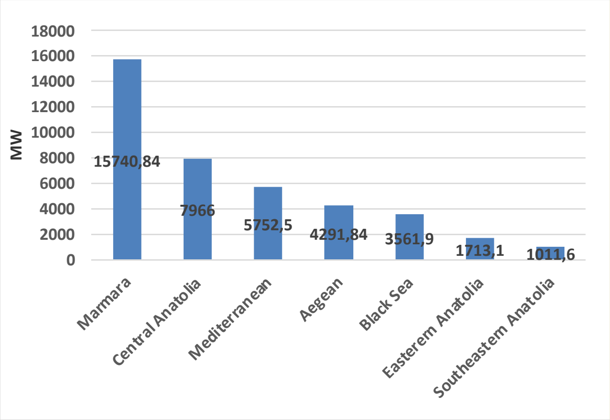

Fig. 10 Wind power plants under evaluation

Fig. 11 Wind power plant of Mersin province

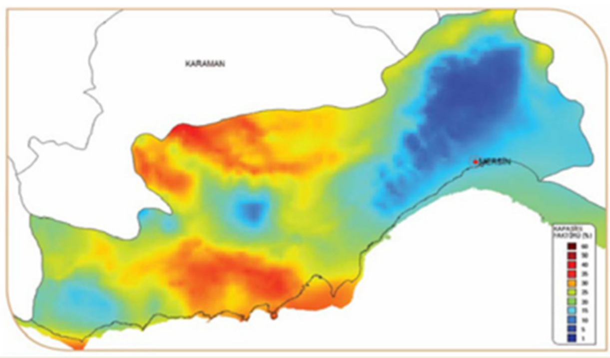

Figure 12. Capacity factor distribution of Mersin province

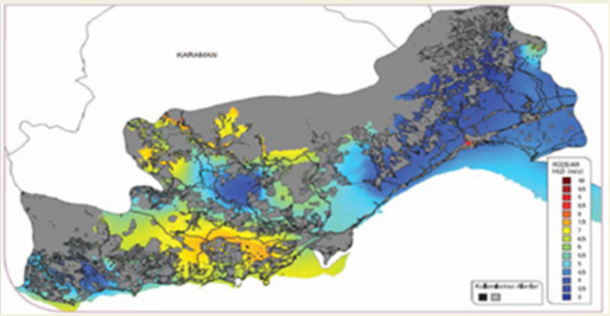

Figure 13. WPP installable areas of Mersin province

these data, in the Mediterranean and Çukurova region, number of wind power plants in operation, under construction, unlicensed and under evaluation show that the region has a very rich wind potential (Fig.11) [29.

Balikesir province has the highest installed wind power capacity is in Turkey. Balıkesir is followed by Manisa and İzmir provinces, respectively. There is a WPP named “Mersin WPP”, owned by Ağaoğlu Energy Group company Akdeniz Elektrik Üretim A.Ş., operating in the Özlü Village of Mut district of Mersin. Mersin WPP project was licensed in 2003 and the operation was started in 2009.

There is also a 39 MW capacity project named “Dagpazarı WPP” of EnerjiSA, which continues in the Mut district of Mersin. Capacity factor maps were examined to determine the wind energy potential of Çukurova Region. The red areas indicate the areas where the capacity is higher and the blue areas are low (Fig. 12). According to the maps in Fig. 12 and Fig. 13 showing the capacity factor distribution and WPP installable areas of Mersin province, Silifke-Gülnar coast of Mersin province and the mountainous areas of Mut-Gülnar emerge as areas with high wind energy potential and where WPP can be established considering other criteria.

The dominant wind direction in Mersin is northwest in winter, and southwest in summer. Considering the arrival directions, generally cold / cool winds in the winter season; It is seen that the winds in the summer is high due to humidity and temperature when the arrival directions, generally cold / cool winds in the winter season are considered (Fig. 14).

3. Conclusions

Today, deterioration of the ecological balance increases the importance of wind energy. In this respect, the share of wind turbines in electricity generation should be increased more. The rapid advancement of technology in the world has increased the need of countries for energy consumption. Orientation to alternative energy sources and investments have increased rapidly in recent years in order to use scarce resources such as water, oil and underground resources more efficiently and to reduce the environmental pollution that increases due to fossil fuel use. Wind Energy is an energy source that, due to its nature, causes little harm to the environment and therefore has low external costs. Technology that converts wind energy into electrical energy does not require large capital. This is an important advantage which causes a lower operating cost. Wind power is one of the renewable energy sources that stands out with its advantages such as low cost, less area of turbines compared to solar panels, low maintenance and repair costs and reduced dependency on foreign countries. Similar projects need to be supported in order to use wind energy systems more widely and put the existing potential into use. Supporting wind energy by local administrations is also important for the future of wind energy. In the study, the annual power generation values obtained with wind power plant capacity factors were compared. It is noteworthy that wind power plant capacity factors are almost the same. Wind speeds were investigated for potential wind turbines to be installed in the region by using wind speeds measured in the year of 2018 in Mersin Region. The following results can be derived from this work.

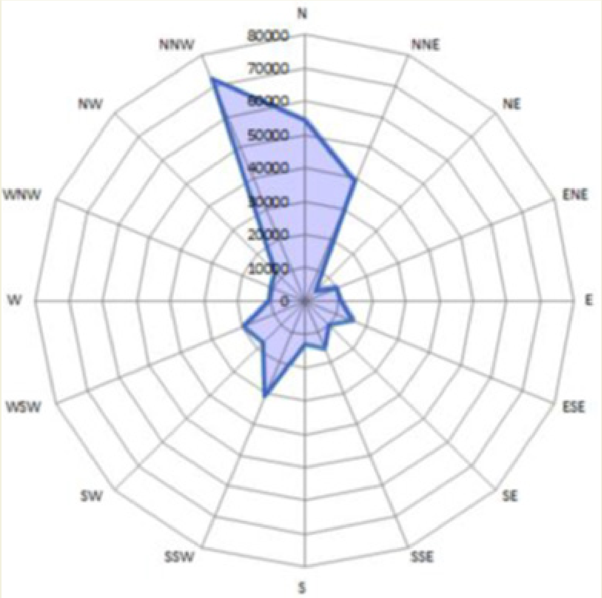

Fig. 14 Dominant wind direction in Mersin province

It has been observed that wind speeds in the range of 2 - 3 m . s^{-1} gives better results when the real values are considered.

As a result of the measurements and analyses made in this study, wind energy analysis was estimated for the Mersin region. When the wind data of Mersin is analysed, it is seen that the potential exists and that there are suitable investment areas especially in Mut district. Therefore, wind farm applications started intensely in this region. These systems can be used as a priority in energy production due to their advantages such as positive contributions to the environment and not harming the agricultural areas and changing according to the purpose of use.

The study shows that Mersin province is very suitable for wind power investment. Since the Mersin region is also an area where agricultural activities are intensive, integrating the electricity produced from turbines into agricultural activities will also provide an advantage. Turkey’s current energy sources are not sufficient and the energy needs of the growing population and developing industry increasing rapidly. Therefore, the gap between energy production and consumption is growing rapidly. Considering the rapid depletion of energy resources, the use of renewable energy resources should be encouraged and the private sector should be supported in this area.

The wind power plants are far from the consumption centres and the regional energy supply security is not provided. This is one of the main problems faced by investors in wind energy in Turkey; This problem should be overcome with incentives and appropriate planning.

Considering the increasing and changing needs of the wind energy sector at the national and international level, support should be provided to companies in the region to become suppliers to both the domestic and export-oriented wind energy sector. It should also be aimed to increase the new investments to be made in this sector.

20% of the land use of Çukurova Region consists of agricultural areas and much more forest areas, it can be said that most of the region is rural. In this context, the use of small-scale wind turbines should be expanded in the countryside.

The evaluation of the wind energy potential with the intensive studies and supports made to the investors help to increase the use of wind energy in Mersin province.

It is also possible to say that Hatay, Mersin and Osmaniye will be pioneers in the increase of installed power due to available potential if the required attention is given.

4. Acknowledgements

The authors would like to thank the General Directorate of State Meteorology Affairs for providing meteorological data for Mersin province, the anonymous reviewers, managing editor, and editor in chief for their valuable help in improving the manuscript.

Conflict of interest M Dağtekin and B Yelmen declare that they have no competing interests.

5. References

[1] Akın, S., Kara, Y.A. (2016). A wind power plant feasibility study for Bursa Gemlik region, Turkey. European Journal of Sustainable Development 1: 44-52.

[2] Yılmaz, M. (2012). Turkey's energy potential of renewable energy and electric power generation the importance of source. Ankara University Journal of Environmental Sciences 4(2):33-54.

[3] Sestoa, E., Casale, C. (1998). Exploitation of wind and energy source to meet the world's electricity demand. Journal of Wind Engineering and Industrial Aerodynamics 74:375-387.

[4] Dereli, S. (2001). Wind energy. Publication of Tübitak, Ankara, Turkey.

[5] Yılmaz, İ., İlbaş, M., Su, Ş. (2003). Evaluation of wind energy potential in Turkey. Proceedings 2. New and Renewable Energy Resource Symposium, Tmmob, Kayseri, Turkey 399-401.

[6] Özgener, O. (2002). Wind energy usage in Turkey and the World. D.E. University Faculty of Engineering, Journal of Science and Engineering 3(4):159-173.

[7] Özkaya, S. Y. (2004). Renewable energy sources, international, journal of economic issues. Ministry of Foreign Affairs Publications 14:8.

[8] REN (2019). Republic of Turkey general directorate of renewable energy. www.yegm.gov.tr. Accessed 21 Feb 2020.

[9] Altuntaşoğlu, Z. (2011). Wind energy in Turkey, current status and problems. Engineer and Machine 617:56-63.

[10] Kapluhan, E. A. (2013). Geography study to increase energy: wind energy use status in the world and in Turkey. International Journal of Social Research 31(7):813-825.

[11] Çivi, C., Köksal, N.S. (2011). Investigation of damages occurred in wind turbines. CBU Soma Vocational School Journal of Technical Sciences 2(6):45-56.

[12] Kaplan, Y.A. (2015) Overview of wind energy in the world and assessment of current wind energy policies in Turkey. Renewable and Sustainable Energy Reviews 43:562-568.

[13] GWS (2011). Global wind statistics. www.gwec.net/fileadmin/documents/Publications/ GWEC_PRstats_02-02-2011_final.pdf. Accessed 11 March 2020.

[14] TWEA (2019). Turkish wind energy association. http://www.tureb.com.tr/eng. Accessed 27 Feb 2020.

[15] TSMS (2007). Wind atlas of Turkey. Turkish state meteorological service. http://www.meteoroloji.gov.tr. Accessed 27 Feb 2020.

[16] SPO (2019). Electrical energy specialization commission report, 8. five-year development plan (special commission on electricity energy state planning organization) 256:585 https://www.sbb.gov.tr/wpcontent/uploads/2018/11/08_ElektrikEnerjisi.pdf. Accessed 22 Feb 2020.

[17] EIE (2007). The wind projects of EIE, electrical power resources surveying administration. http://www.eie.gov.tr/turkce/ruzgar/RGI_AYLIK_HIZLAR.xls. Accessed 16 Jan 2020.

[18] Yağlı, M.I. (2009). Wind energy a renewable energy source. International journal of economic issues. Publications of the Ministry of Foreign Affairs 34:35-37.

[19] EIE (1984). Turkey wind energy potential natural, Electrical power resources surveying administration, Ankara, Turkey 85:1.

[20] Şenel, M.C., Koç, E. (2015). In Turkey and the world wind energy status general evaluation. Engineering and Machinery 56(3):46-56.

[21] Köksal, N.S. (2019). Investigation of Manisa-Kırkagac wind potential. https://docplayer.biz.tr/8362412-Manisa-kirkagac-ruzgar-potansiyelinin-incelenmesi-n-sinan-koksal.html. Accessed 30 March 2020.

[22] TURSAT (2012). Turkey wind energy statistics report. Accessed 17 March 2020.

[23] Gülersoy, T., Çetin, N. (1990). Using rayleigh and weibull distributions for wind turbines in Menemen Region. Journal of Polytechnic 13(3):209-213.

[24] Arslan, O.P., Arıkan, Y, Erten, M. (2014). Energy and cost analysis for wind turbine to be established at Kırıkkale University. International Journal of Engineering Research and Development 6(2):1-5.

[25] Yıldırım, U., Gazibey, Y., Güngör, A. (2012). Wind energy potential of Niğde province. Niğde University Journal of Engineering Sciences 1(1):37-47.

[26] Akkaş, V.C. (2016). Çukurova region wind energy report. Energy Panorama, Journal 42-47.

[27] Kaplan, Y.A., Agalar, S. (2013). Wind energy status and Policies in Turkey and in the World. UTES, Konya, Turkey 762-765.

[28] Anonymous (2020). Mersin Province Map. http://cografyaharita.com/turkiye_mulki_idare_haritalari3.html. Accessed 22 Feb 2020

[29] Anonymous (2021). Mersin Province WPP Investments. https://www.yatirimlar.com/haberPolat_Enerjinin_Mersin%20RES_Projesi%20icin%20On%20Lisans%20Verildi-261720.htm%20Accessed%2029%20March%202021.

EUROPEAN
MECHANICAL
SCIENCE

e-ISSN: 2587-1110

RESEARCH ARTICLE

Role of sintering conditions on structural and mechanical properties of carbon fiber fabric reinforced ZrB_2-Sic composites

Asli Asiye Agil[1*], **Erhan Ayas**[1]

[1]Department of Materials Science and Engineering, Eskişehir Technical University, Eskişehir, 26555, Turkey

Orcid: A.A.Agil (0000-0002-0683-2954), E. Ayas (0000-0003-0592-3990)

Abstract: In this study, the effects of sintering conditions on the structural and mechanical properties of spark plasma sintered ZrB2-based composites were investigated in detail. In addition, to observe the impact of the binder, the binder was used in some materials. Thus, the effects of binder on the properties of composites while preparing ceramic slurry were tested. The effects of the sintering conditions of the materials prepared at different temperatures and stages on the composites were examined in detail. The densities, phase developments, microstructure analyses and mechanical properties of the composites were determined by the Archimedes principle, X-Ray Diffraction, Scanning Electron Microscopy, and three-point bending test, respectively. It was found that the samples sintered in double-stage and containing binder exhibited a denser microstructure. Similarly, it was observed that the mechanical properties were improved by using both double-stage sintering and binder.

Keywords: Ceramic matrix composites, Carbon fiber, Spark plasma sintering, Microstructure, Three-point bending test.

1. Introduction

Zirconium diboride (ZrB_2) is a preferred material for use on the sharp surfaces of hypersonic aircraft. Due to its high melting point, ZrB_2 is used in parts such as engine hood inlets, wing front edges, and nose cavities that must withstand temperatures of 1900-2500°C. SiC is a promising material in engineering applications requiring high temperatures due to its excellent mechanical properties at high temperatures, high thermal conductivity, high corrosion, and wear resistance. However, application fields of SiC remain limited due to its low fracture toughness. To overcome the low fracture toughness of SiC ceramics, fiber is added to the SiC matrix [1]. It has been proven that adding SiC to ZrB_2 increases its oxidation resistance and limits diboride grain growth [2].

Although the ZrB_2–SiC material has been developed, its use has many problems in large-scale applications. First, parts with complex shapes and high density are difficult to shape, fabricate and sinter due to their strong covalent bonds. Carbon is used as an additive to improve the thermal tensile strength of the ZrB_2-SiC system. However, the low fracture toughness and low thermal shock resistance properties still need to be improved. Therefore, the use of a fiber reinforcement phase can be exploited to increase the fracture toughness of the ZrB_2-SiC material, allow it to reach an acceptable level of thermal stress, and reduce its density. Carbon fiber is an exciting candidate for this role because of its thermodynamic compatibility, high specific strength and hardness with ZrB_2-SiC below 3000 K, and high-temperature resistance above 2000 K [2].

Compared to conventional methods, the Spark Plasma Sintering (SPS) technique makes it possible to sinter ZrB_2-SiC composites at lower temperatures and in shorter times. In the SPS technique, while a direct current is applied to the powder-filled graphite die, a uniaxial pressure is applied to the die simultaneously. Thus, grain growth can be prevented thanks to the fast heating rate, and a denser microstructure can be achieved. In addition, the microstructure can be kept under control with the help of faster heating rates and shorter processing times [3].

Hu et al. reported the mechanical properties of carbon fiber reinforced SiC-ZrB_2 composites produced by infiltration, pre-infiltration and pyrolysis (PIP) methods using slurry prepared from polycarbosilane (PCS)/ZrB_2/divinyl benzene (DVB) [4]. This study found that carbon fiber increased fracture toughness and ZrB_2 matrix improved flexural strength above 1800°C.

Asl investigated the effects of sintering conditions of SiC particles and chopped carbon fibers on the microstruc-

---

[*] Corresponding author.
Email: aaagil@eskisehir.edu.tr

European Mechanical Science (2022), 6(4): 278-284
https://doi.org/10.26701/ems.1178561
Received: September 12, 2022 — Accepted: November 14, 2022

Table 1. Materials used in ceramic slurry

Sample	Liquid Medium	Ceramic Powders	Dispersant	Binder
Set 1	Ethanol	Alpha-SiC and ZrB_2	PEI (~0,2 g)	PVB (0,1 g)

Table 2. Sintering parameters of the composites

Sample	Pressure (P_1)	Temperature (T_1)	Dwell Time (t_1)	Pressure (P_2)	Temperature (T_2)	Dwell Time (t_2)
Set1-1900-10min	50 MPa	1900 °C	10 min	-	-	-
Set1-1950-10min	50 MPa	1950 °C	10 min	-	-	-
Set1-2000-10min	50 MPa	2000 °C	10 min	-	-	-
Set1-1900-double-10min	30 MPa	1600 °C	5 min	50 MPa	1900 °C	10 min
Set1-1900-double-10min-PVB	30 MPa	1600 °C	5 min	50 MPa	1900 °C	10 min

ture and mechanical properties of ZrB_2-based composites. Asl reported that the sintering temperature was the most influential factor in hardness. In addition, the optimum production conditions were determined as 1850°C temperature, 6 minutes waiting time and 30 MPa pressure [5].

Balak et al. used Taguchi L_{32} experimental design to optimize the flexural strength of ZrB2-based composites prepared with SPS. As a result of this study concluded that the most critical effect on flexural strength was related to temperature, SiC and carbon fiber, respectively [6].

Karimirad et al. investigated the effects of short carbon fibers on the sinterability, flexural strength, fracture toughness and thermal shock resistance of spark plasma sintered ZrB_2-SiC composites. They found that the addition of short carbon fibers to the ZrB_2 – 30 vol.% SiC composite results in lower hardness, lower relative density, poor sinterability and increased volume percentage of open porosity [7].

This study focused on investigating the effects of sintering temperature, sintering step and binder use on the structural and mechanical properties of carbon fiber reinforced ZrB_2-SiC ceramic matrix composites. As far as we know, there is no other study in the literature investigating these three parameters simultaneously. In addition, the way the prepared slurry is applied to the carbon fiber fabric is one of the original values of the study.

2. Materials and Method

2.1. Preparation of ceramic slurry

The first step for the fabrication of composite materials is the preparation of ceramic slurries. In this study, ceramic slurries with 20 wt.% solids were prepared. The precursor powders used while preparing the slurry are alpha-SiC (Alpha Aesar, 2 microns, 99.8% purity) and ZrB_2 (H.C. Starck, Grade A). In addition, polyethyleneimine (PEI) was used as a dispersant and polyvinyl butyral (PVB) was used as a binder. Ethanol was used as the liquid medium. The SiC ratio in these powders was 20%wt. Moreover, the effects of binders were examined while preparing some materials. These materials are from now on referred to as Set 1.

Ceramic slurries were prepared using separate plastic bottles for each sample. Starting materials were added to the plastic bottles indicated in Table 1. Si_3N_4 balls were placed in each bottle to obtain a more homogeneous mixture and the slurries were mixed for 24 hours in a ball mill. The amount of slurry prepared for each composite is approximately 50 ml.

After the ceramic slurry was prepared, this slurry was impregnated with carbon fiber fabrics. Firstly, carbon fiber fabrics were cut in a circular shape, arranged in a single layer, and pour the slurry on them. Circular fabrics had a diameter of 4 cm. 24 layers of carbon fiber fabrics were used for each sample. Circular fabrics were left in an oven for 24 hours to evaporate the alcohol and dried completely.

2.2. Sintering of materials with the spark plasma method (SPS)

Graphite dies with a diameter of 40 mm were used in Spark Plasma Sintering (SPS). First, the graphite die's lateral, upper and lower surfaces were covered with graphite foil. Then, the fabrics were placed in a graphite die. In this study, some samples were subjected to single-stage and double-stage sintering processes, and these processes' effects were discussed. The applied pressure, maximum temperature and dwell time in the single-stage sintering process were expressed as P_1, T_1 and t_1, respectively. In

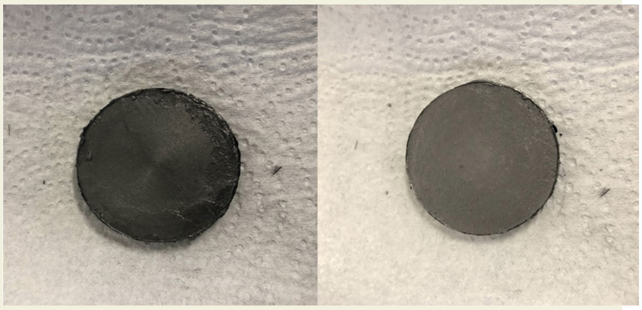

Figure 1. Images of composite materials obtained after the sintering process.

https://doi.org/10.26701/ems.1178561

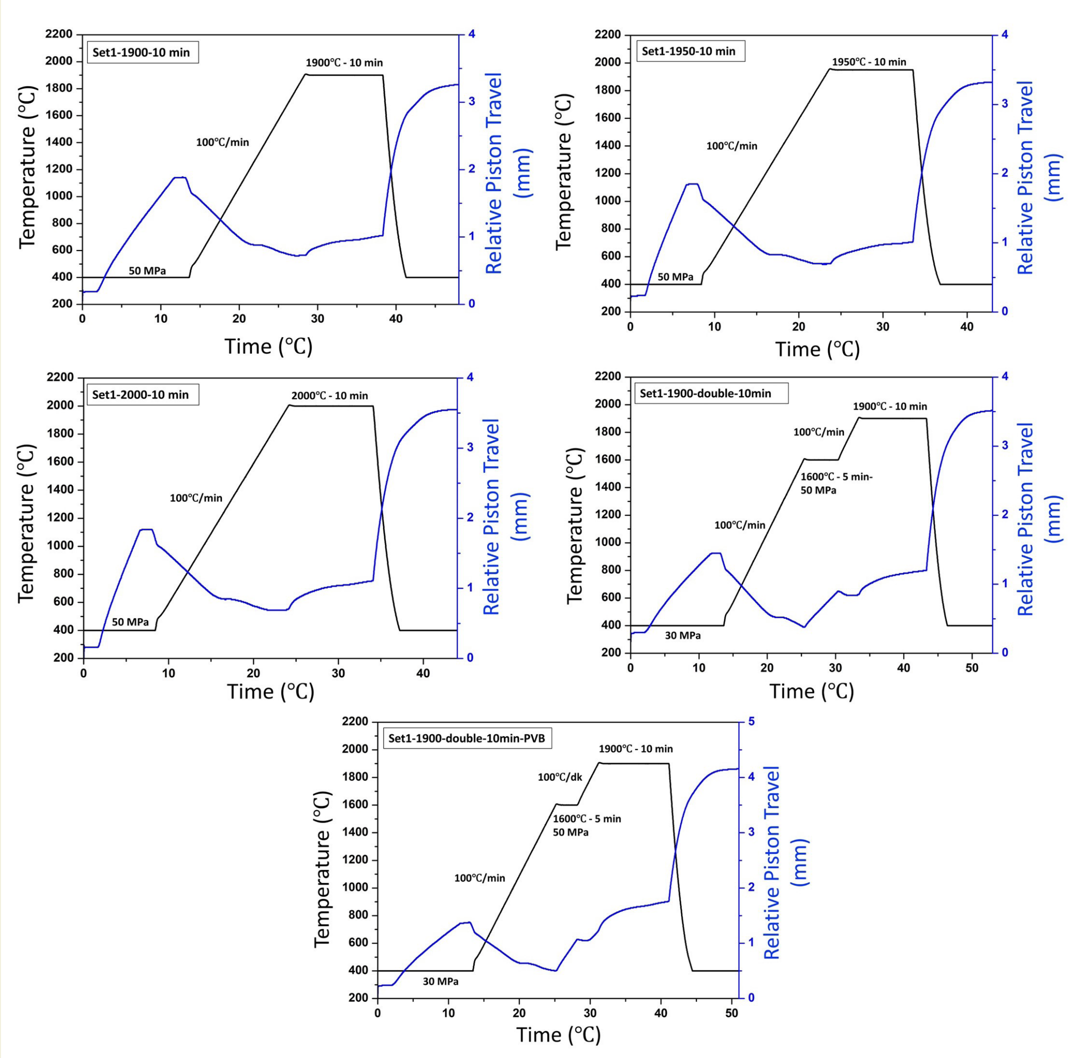

Figure 2. SPS curves of Set-1 samples.

double-stage sintering, the first pressure, temperature and dwell time are P_1, T_1 and t_1, respectively, and then the applied pressure, maximum temperature and dwell time in the second stage are indicated as P_2, T_2 and t_2, respectively. Table 2 shows the sintering parameters of samples with different compositions. Some of the samples obtained after sintering are shown in Figure 1. The diameter of the samples obtained after the sintering process was 4 cm and their thickness was approximately 3.5 mm.

Figure 2 shows the SPS curves of the composites. Set-1 samples were subjected to two different sintering processes as single-stage and double-stage sintering. In single-stage sintering, the applied pressure was chosen as 50 MPa, the heating rate was 100 °C/min, and the dwell time was 10 minutes. To determine the most suitable sintering temperature of the samples with the same composition, experiments were carried out at three different temperatures, 1900 °C, 1950 °C and 2000 °C. As seen from the sintering curves, sintering could not be fully realized at all three temperatures. Due to the incomplete sintering, sintering was carried out for two samples with and without binder additives having the same composition. This time, double-stage sintering was applied instead of single-stage sintering. When the single stage sintering graphs were examined, it was decided to perform double-stage sintering by waiting at 1600 °C due to the change in the relative piston travel observed at approximately this tempetature. The reason for this is to observe whether there will be an increase in density with double-stage sintering compared to single-stage sintering.

When the sintering graphs of these samples were examined, it was seen that the sample had started to sinter but a fully sintered structure could not be obtained because the temperature and/or time were insufficient.

After the sintering process, the surface of the samples was removed from the graphite foil. Samples were kept in the oven for a while and the moisture in the samples was removed. Dry weights of the moisture-removed samples were measured and recorded. Then, for density measurements, the samples were taken into separate beakers and boiled in distilled water for 120 minutes, and wet and air weights were measured using the Archimedes kit. Density calculations were made according to these values. Then the samples were cut into suitable sizes for mechanical tests, microstructure and phase analysis.

3. Results and Discussions

3.1. Density analysis

The Archimedes method calculated the produced composites' densities and open porosity values with the following equations [8].

$$d = \frac{W_3}{W_2 - W_1} \quad (1)$$

$$O.P(\%) = \frac{W_2 - W_3}{W_2 - W_1} * 100 \quad (2)$$

Here, d is the composite density, W_1, W_2 and W_3 are air, wet and dry weights, respectively. The results obtained from the density calculations are given in Table 3.

When the results of the density analyzes of Set-1 samples were examined, it was observed that the density values of the samples increased as the sintering temperature increased in the samples with single-stage sintering, as expected. When the single and double-stage sintered samples were compared, it was seen that the density values of the samples sintered in single and double stages at the same time were quite close to each other. When the samples with and without binder added were compared with each other, it was seen that the highest density value belonged to the sample subjected to a double-stage sintering process at 1900 °C and to which binder (PVB) was added.

3.2. Phase development

The X-Ray Diffraction (XRD) method was performed for phase analysis of the composites. Rigaku Miniflex XRD machine was used for these analyses. Firstly, XRD analyses were performed to determine any impurities in the starting powders: alpha-SiC and ZrB_2. Figure 3 shows the XRD patterns of these powders. No secondary phase was found in the XRD patterns of the starting powders.

XRD patterns of Set-1 samples were given in Figure 4. The sample content is carbon fiber fabric, ZrB_2 and SiC powders. These phases were found in the structure. Due to the carbon fiber fabric and the graphite die used during sintering, it was seen that carbon and graphite phases were also included in the structure. Finally, in addition to these phases, the ZrC phase was also found in the structure. This ZrC phase was also encountered in another study [9], and it was reported that this was due to the reaction between covering the ZrB_2 particles ZrO_2 and C, according to the following reaction:

$$ZrO_2 + 3C = ZrC + 2CO \quad (3)$$

The formation of these phases has also been revealed in previously reported studies [10-13].

3.3. Microstructure analysis

Scanning electron microscopy (SEM) images of Set-1 samples are shown in Figure 5.

When the microstructures of Set-1 samples were examined, it was seen that the composite (Set1-1900-double-

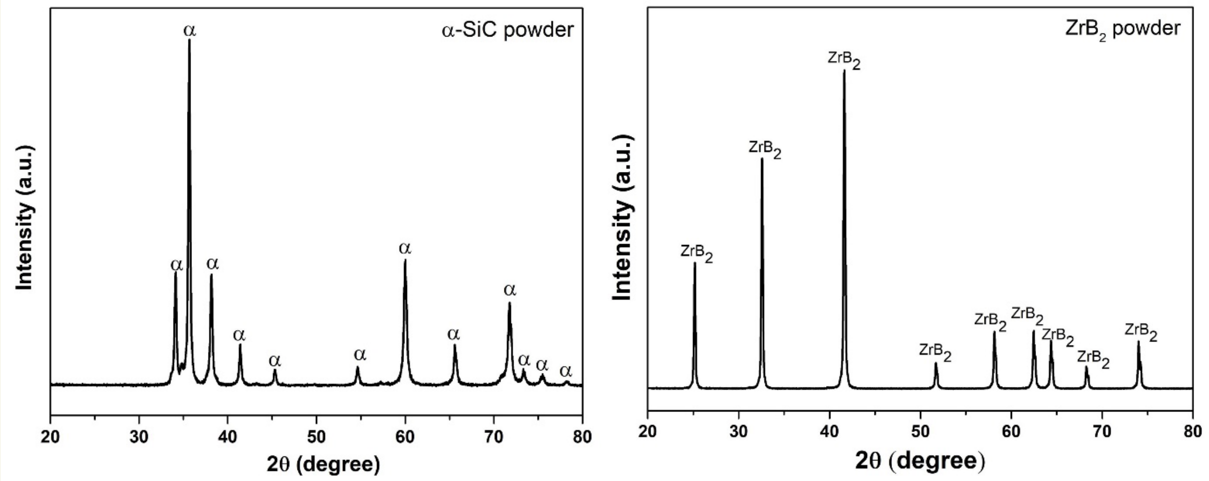

Figure 3. XRD patterns of (a) alpha-SiC and (b) ZrB_2 powders,respectively.

Table 3. Density and open porosity values

Sample	W_1 (g)	W_2 (g)	W_3 (g)	Density (g/cm³)	O.P (%)
Set1-1900-10min	3,408	7,0286	6,4951	1,7939	14,74
Set1-1950-10min	3,126	6,321	5,9605	1,8656	11,28
Set1-2000-10min	3,2953	6,5375	6,0898	1,8783	13,81
Set1-1900-double-10min	3,1518	6,5679	6,1335	1,7955	12,72
Set1-1900-double-10min-PVB	5,2399	9,0005	8,6905	2,3109	8,24

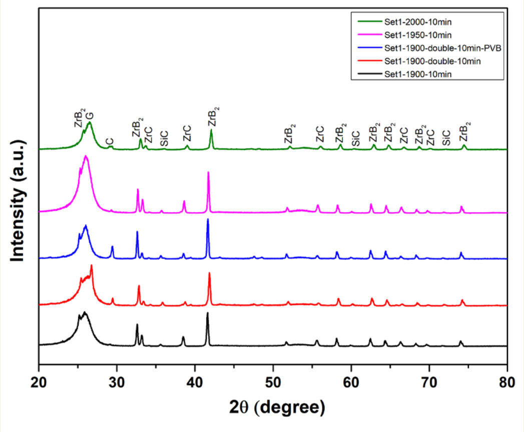

Figure 4. XRD patterns of Set1-samples.

10min-PVB) produced with a slurry-containing binder had the densest structure. This result is also consistent with the density analyses determined by Archimedes' principle, as mentioned in the previous section. It is thought that the reason is that the binder (PVB) stabilized the viscosity of the slurry [14].

As can be seen from the microstructures of composites, it is seen that the densification is higher in composites containing binder (PVB). However, as can be seen from the images, it was also observed that a homogeneous density could not be obtained throughout the entire structure and the ceramic particles were not fully homogeneously distributed between the fibers. Moreover, despite dense regions in places, there is still regional porosity between the fibers.

3.4. Mechanical properties

The mechanical properties of the composites were investigated using the three-point bending test. Instron 5581 device was used for this test. Measurements were carried out at room temperature. The dimensions of the test specimen were approximately 3 mm x 4 mm x 25 mm. The applied force was 2 kN with a span of 20 mm and a cross-head speed of 0.5 mm/min. Three-point bending test results of Set-1 composites are shown in Table 4.

Compared to similar studies, the mechanical results of our samples were found to be approximately two to one-third lower than the results reported in the literature [15-16]. It is thought that this is due to the inability to obtain a dense structure throughout the entire composite, as clearly determined from both density analyses and microstructure images, due to insufficient sintering temperature or time.

Hu et al. reported a decrease in flexural strength and

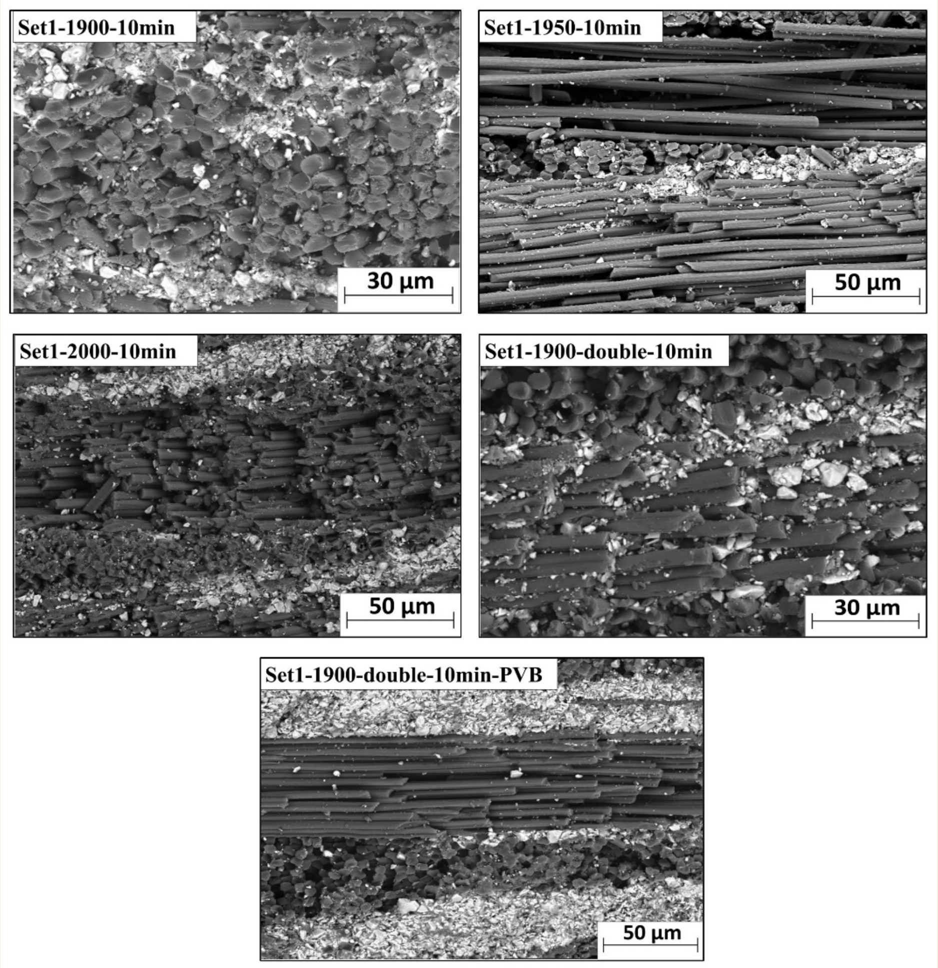

Figure 5. SEM images of Set-1 samples.

Table 4. Mechanical test results of Set-1 composites.

Sample	Maximum Flexure load (kN)	Flexure stress at Maximum Flexure load (MPa)	Modulus (Automatic) (GPa)	Flexure strain at Break (Standard) (mm/mm)	Flexure extension at Maximum Flexure load (mm)	Flexure stress at Break (Standard) (MPa)
Set1-1900-10min	0.039	30.244	4.87	0.17697	0.34032	8.37630
Set1-1950-10min	0.050	36.134	5.97	0.08409	0.34214	10.15255
Set1-2000-10min	0.039	22.196	1.96	0.12573	1.62585	7.05098
Set1-1900-double-10min	0.029	19.101	2.46	0.10869	0.31020	6.15574
Set1-1900-double-10min-PVB	0.071	54.954	11.93	0.15320	1.54052	11.25895

modulus with increasing the amount of ZrB_2 in the structure. In the same study, it is stated that the presence of carbon fiber contributes to both flexural strength and elastic modulus. Carbon fiber significantly increases flexural strength, which provides excellent thermal shock resistance under ultra-high temperature conditions, while increasing the reliability ratio of composite materials, enabling the production of thicker and more complex materials [4].

4. Conclusions

In this study, composites were fabricated under different sintering conditions using alpha-SiC, ZrB_2 starting powders and carbon fiber fabric, and the effects of these conditions on density, microstructure, phase analysis and mechanical properties were investigated. In addition, the impact of using binders in producing some materials was characterized. If the results obtained are summarized;

- The highest density was reached in Set1-1900-double-10min-PVB composite, which was sintered in double stages and contained a binder. It is thought that the double-stage sintering process has a positive effect on the densification mechanism.
- Consistent with the results obtained from the density analyses, it was also found that the samples sintered in double-stage and containing binder exhibited a denser microstructure.
- It was determined that the material with the best mechanical properties was Set1-1900-double-10min-PVB. It is thought that using PVB as a binder in this material improves mechanical properties.

5. Acknowledgement

This work was supported by the Research Fund of Eskişehir Technical University, Eskişehir, Turkey, under Grant Contract No: 20DRP021.

6. References

[1] Ding, Y., Dong, S., Huang, Z., Jiang, D. (2007). Fabrication of short C fiber-reinforced SiC composites by spark plasma sintering. Ceramics International, 33, 1, 101–105, DOI: 10.1016/j.ceramint.2005.08.004.

[2] Tang, S., Deng, J., Wang, S., Liu, W. (2007). Fabrication and characterization of an ultrahigh-temperature carbon fiber-reinforced ZrB2-SiC matrix composite. Journal of American Ceramic Society, 90, 10, 3320–3322, DOI: 10.1111/j.1551-2916.2007.01876.x.

[3] Akin, I., Hotta, M., Sahin, F.C., Yucel, O., Goller, G., Goto, T. (2009). Microstructure and densification of ZrB2-SiC composites prepared by spark plasma sintering. Journal European Ceramic Society, 29, 11, 2379–2385, DOI: 10.1016/j.jeurceramsoc.2009.01.011.

[4] Hu, H., Wang, Q., Chen, Z., Zhang, C., Zhang, Y., Wang, J. (2010). Preparation and characterization of C/SiC-ZrB2 composites by precursor infiltration and pyrolysis process. Ceramics International, 36, 1011–1016, DOI: 10.1016/j.ceramint.2009.11.015.

[5] Shahedi Asl, M. (2017). Microstructure, hardness and fracture toughness of spark plasma sintered ZrB2–SiC–Cf composites. Ceramics International, 43, 17, 15047–15052, DOI: 10.1016/j.ceramint.2017.08.030.

[6] Balak, Z., Zakeri, M. (2016). Application of Taguchi L32 orthogonal design to optimize flexural strength of ZrB2-based composites prepared by spark plasma sintering. International Journal of Refractory Metals and Hard Materials, 55, 58-67, DOI: 10.1016/j.ijrmhm.2015.11.009.

[7] Karimirad, S., Balak, Z. (2019). Characteristics of spark plasma sintered ZrB2-SiC-SCFs composites. Ceramics International, 45, 5, 6275-6281, DOI: 10.1016/j.ceramint.2018.12.109.

[8] ASTM C 373-88: Standard Test Method for Water Absorption, Bulk Density, Apparent Porosity, and Apparent Specific Gravity of Fired Whiteware Products, 2006.

[9] Zoli, L., Vinci, A., Silvestroni, L., Sciti, D., Reece, M., Grasso, S. (2017). Rapid spark plasma sintering to produce dense UHTCs reinforced with undamaged carbon fibres. Materials & Design, 130, 1–7, DOI:10.1016/j.matdes.2017.05.029.

[10] Monteverde, F., Guicciardi, S., Bellosi, A. (2003). Advances in microstructure and mechanical properties of zirconium diboride based ceramics, Materials Science and Engineering: A, 346, 310–319, DOI: 10.1016/S0921-5093(02)00520-8.

[11] Silvestroni, L., Dalle Fabbriche, D., Melandri, C., Sciti, D. (2016). Relationships between carbon fiber type and interfacial domain in ZrB2-based ceramics, Journal of the European Ceramic Society, 36, 17–24, DOI: 10.1016/j.jeurceramsoc.2015.09.026.

[12] Sciti, D., Silvestroni, L., Medri, V., Monteverde, F. (2014). Sintering and densification of ultrahigh temperature ceramics, in: W. Fahrenholtz, E. Wuchina, W. Lee, Y. Zhou (Eds.), Ultra-high Temperature Ceramics: Materials for Extreme

Environment Applications, Wiley, Inc., 112–143 ISBN 0-471-9781118700785, DOI: 10.1002/9781118700853.ch6.

[13] Silvestroni, L., Fabbriche, D.D., Sciti, D. (2015). Tyranno SA3 fiber–ZrB2 composites. Part I: microstructure and densification, Materials & Design, 65, 1253–1263, DOI:10.1016/j.matdes.2014.08.068.

[14] Zhao, P., Zhao, X., Wang, H. (2019). Processing and Properties of Laminated ZrB2-Mo5SiB2 Ceramic Composites Fabricated by Tape casting and Hot Pressing Sintering. IOP Conf. Series: Materials Science and Engineering, 678, 012072, DOI: 10.1088/1757-899X/678/1/012072.

[15] Zhang, D., Hu, P., Feng, J., Xie, M., Zhao, H., Zhang, X. (2019). Characterization and mechanical properties of Cf/ZrB2-SiC composites fabricated by a hybrid technique based on slurry impregnation, polymer infiltration and pyrolysis and low-temperature hot pressing. Ceramics International, 45, 5467–5474, DOI: 10.1016/j.ceramint.2018.12.001.

[16] Bakera, B., Rubiob, V., Ramanujamc, P., Binnera, J., Hussaind, A., Ackermand, T., Browne, P., Dautremontf, I. (2019). Development of a slurry injection technique for continuous fibre ultra-high temperature ceramic matrix composites. Journal of the European Ceramic Society, 39, 3927–3937, DOI: 10.1016/j.jeurceramsoc.2019.05.070.

EUROPEAN MECHANICAL SCIENCE
e-ISSN: 2587-1110

RESEARCH ARTICLE

Statistical characteristics, probability distribution, and power potential of sea water velocity in Turkey

Alper Yildirim[1*]

[1]Department of Machinery and Metal Technology, Osmaniye Vocational School of Higher Education, Osmaniye Korkut Ata University, 80000, Osmaniye, Turkey

Orcid: A. Yildirim (0000-0003-2626-1666)

Abstract: Sea currents have the potential to supply electricity from a renewable energy source to coastal regions. The assessment of the potential energy that could be generated is the first step toward developing this resource. In this study, the data was collected at 5 m and 35 m depths below the sea surface level, including sea current velocity and direction. A detailed field measurement, of the probability of sea water velocity at three stations (Antalya, Silivri, Istanbul) for 5 months is carried out. The sea current power density values in these stations were 10.41, 4.92, and 7.91 W/m^2 at 5 m depth, respectively. Besides, average sea current power density values were seen to be closely arranged with 11.44, 4.07, and 9.06 W/m^2 at 35 depths, respectively. In addition, statistical analysis applying Weibull and Rayleigh models is also presented. It is shown that the use of a Weibull probability distribution facilitates the analysis of sea velocity conditions and is also able to predict the power density with a high degree of accuracy. The results of this study are useful for the understanding of the marine hydrokinetic energy of these areas, where sea current power projects may be started in Turkey.

Keywords: Marine hydrokinetic, Ocean power, Sea current velocity, Turkish seas, Weibull, and Rayleigh probability function.

1. Introduction

In the last decade or so, renewable energy resources (RES) have become a necessity and sought after all over the world, with their uptake rapidly increasing in most developing and/or developed countries. [1]. Especially in terms of generating electricity, the RES has been thought to play a central role. The power generation from the RESs is considered to be sustainable, cleaner, environmentally friendly, and cost-effective, compared to the power from traditional power resources. Moreover, they are much more cost-effective as well. The Increasing deployment of the RESs for the future power grid is an indication of the appropriateness of sustainable energy generation [2]. Although the main forms of renewable energy such as biomass, hydroelectricity, wind, solar, and geothermal energy still predominate the entire energy landscape, other sources such as various forms of ocean energy have also proved promising and extensive discussions about the feasibility of them have taken place during the last decades [3]. It has been estimated that the share of RES in the total primary energy supply will see a dramatic increase from 14% in 2015 to 63% in 2050. This increase corresponds to an annual average growth rate of 1.4%. Simultaneously, the share of fossil fuels would drop from 86% to 37%. Though energy consumption from 2015 to 2050 is expected to be almost constant, economic activity is predicted to triple. The growth of the RES together with the spectacular increase in energy efficiency could provide a 94% reduction that would enable it to stay within the limits of the Paris Climate Agreement. All these have repercussions and consequences not simply related to the energy sector, but also to the way societies are organized in their entire ecosystem [4].

Ocean energy technologies are typically classified according to the source of energy they use. The most widely used technologies across geographies are tidal stream and wave energy converters. Other types of ocean energy technologies, such as those that harness energy from differences in salinity or temperature, or those that use ocean currents, could become more relevant over the long run. The current total installed capacity for all ocean energy technologies is 534.7 MW. Tidal barrage technology accounts for more than 98% of the total combined capacity currently operational, or 521.5 MW. Thus, ocean energy resources have the potential to be a significant source of RES, with estimates indicating that up to 337 GW of installed capacity could be available globally by 2050 [6].

---

[*] Corresponding author.
Email: alperyildirim@osmaniye.edu.tr

European Mechanical Science (2022), 6(4): 285-297
https://doi.org/10.26701/ems.1195271
Received: October 27, 2022 — Accepted: November 24, 2022

Ocean currents are streams formed by the vertical and horizontal components of the ocean's circulation system which are produced by wind friction, gravity, and variations in water density in different parts of the ocean. These currents, like winds in the atmosphere, transfer large amounts of heat from the equator to the poles and thus play an important role in determining the climates of coastal areas. Moreover, atmospheric circulation and ocean currents influence one another [8]. The relatively constant flow of ocean currents carries large amounts of water across the earth's oceans. Technologies are being developed so that this energy can be extracted from ocean currents and converted to usable power Ocean currents have a wide range of effects on marine life, moving not only plants and animals around the ocean but also redistributing nutrients and heat [9]. However, they also cause erosion, accretion, and change the coastal morphodynamics of beaches and ocean water intake structures [10].

Long-term and oceanographic monitoring in the open sea is a well-recognized key topic for scientists studying the oceans, atmosphere, and their interactions. Long-term open-sea data are important for the possible climate changes, weather phenomena, and analysis of air-sea exchange processes. The use of real-time data for regional forecasts and nowcasts is to be used by various user groups dealing with the marine environment for operational activities such as fishing, natural hazards warnings, recreational boating, and rescue operations [11]. In general, databases can result from numerical oceanographic reanalysis or satellite altimetry campaigns. In situ, ship, buoy, or high-frequency radar (HFR) can also be sources of basin-scale long-time series of ocean current data [12]. Examples of these data are given in the following literature study.

HFR measures surface currents in coastal oceans using high-frequency radio waves. HFR has working ranges of up to 200 km and spatial resolutions ranging from 300 to 1000 m. HFR datasets have been heavily used in the last two decades to supplement the understanding of basin scale and circulation in the Atlantic and the Pacific oceans [13]. For example, mesoscale surface current features were studied in the Gulf Stream region [13], in the Monterey Bay [14], in the Monterey Bay [15], in the Long Island [16], in the Kuroshio region [17], in the Gulf of the Farallones [18], for Mid-Atlantic Bight [19], etc. HFR surface current measurements provide insight into the fine structure of nearshore tidal and residual circulations [14,16,20]

The use of satellite products provides data with global coverage but is discontinuous in time, particularly for single-point instruments like altimeters. Furthermore, satellite data must be validated in order to determine the overall precision of the derived dataset [21,22] Ships are a valid support for proper data collection, but they are expensive, prone to problems due to bad weather, and in any case, limited by time and space. When attention is centered on a particular zone, the problem can be successfully solved, at least in terms of time continuity, by using permanent custom-made facilities such as drifting – for example, moored buoys [23] – and ARGO network [23]. These systems, if properly designed, may be able to collect data series in situ for long periods, even in rough seas [11].

The key point is to provide data in an inner sea, where both satellites detected numerical model and physical parameters outputs may show a lack of reliability and accuracy, to complement with open sea ones, the data taken on land. As a result, in the 1970s, the buoy was used to test instruments and components that would later be used on buoys, such as radio transmission systems and electronic acquisition systems. Over the years, the buoy has also been available to outside users. So many research organizations have used the buoy extensively, for specific measurement campaigns as well as the data collected on board regularly. Simultaneously, partnerships with a few small and medium-sized businesses were formed to equip the buoy with data acquisition and updated measurement systems. Wave buoy-based current velocity estimation will also supply a separate current velocity dataset for a variety of global regions where data is currently unavailable. This can be utilized to calibrate and validate numerical models as well as utilized directly for offshore designs [11]. An example of the work done on buoys took place between 2007 and 2009 by the Icelandic Meteorological Office (IMO) which conducted meteorological buoy measurements in the central Iceland Sea [25]. Oliveira et al. observed the current surface circulation and energetics of Brazil with buoys [26].

Various mathematical models for long-term ocean current speed distributions can be considered. The two-parameter Weibull and Rayleigh models are among them. These models are thought to be the current speed distribution in stochastic processes. Given that the two-parameter Weibull distribution and Rayleigh are appropriate for ocean current speed, it is practical to consider and investigate the effect of reflecting ocean current speed in the three-parameter Weibull distribution. Acceptable statistical estimates of the distribution parameters are required for the probability density function to be used successfully [27]. The parameters of the Weibull distribution over the global ocean were estimated based on geostrophic altimetry-based velocities [28]. For example, Chu [29] discussed the Weibull parameters of the upper equatorial Pacific current speed estimated using six stations' hourly ADCP data. Kim et al. [30] applied a statistical model for actual sea current data. They showed that the suggested model can be considered a dependable method that is very simple and has satisfactory results. Kabir et al. [6] analyzed ocean current statistics from the Gulf Stream (North Carolina shore) and found that the Weibull distribution properly fits the current speed PDF. Ashkenazy and Gildor [31] determined the probability density function of sea surface currents obtained with HF radar. They showed that the density of sea surface current velocities can be estimated by the Weibull function model. Ocean energy and offshore wind will have similar development constraints. However, the statistics of sea currents, in contrast to wind speed, have attracted much less attention.

The main aims of the present study are as follows:

a) Measuring hourly sea current velocities at Antalya, Silivri, Istanbul (Istanbul strait) stations, which are located in the Mediterranean sea, a sea of Marmara, and the Black sea of Turkey at 5 and 35 m depths below the sea surface for five months.

b) To model frequency distributions of hourly sea current velocities by utilizing the Weibull and Rayleigh probability density functions.

c) To determine and compare for three stations the sea current velocity probability distributions, frequency distributions of sea current directions, sea current velocity, sea current hydrokinetic power potential, and standard deviations.

d) To shed light on the specificity of Turkey which is surrounded by a sea on three sides including also an importdíant internal sea, the Sea of Marmara, located between the straits of the Bosphorus and the Dardanelles. Turkey has experienced impressive growth in renewables in the past decade (especially wind, solar and geothermal). However, little research has been made about the amount of energy possessed by the sea in Turkey. In addition, there are no marine power plants installed in its seas. Hence a study based on the field measurement of sea water velocity in Turkey is particularly important. In this sense, this study may also provide the necessary information for the potential investors on the costs and economical aspects of planning the sea energy project. Therefore, in addition to other alternative energy sources, we propose to use sea energy resources as a way to expand Turkey's energy matrix in the coming decades.

2. Method

2.1. Statistical Variables and Probability Density

Mean sea current velocity (μ) is simply a numerical average, and is calculated as;

$$\mu = \left(\frac{1}{n}\right)\sum_{i=1}^{n} v_i \tag{1}$$

Standard deviation is expressed as;

$$\sigma = \left(\frac{1}{n-1}\sum_{i=1}^{n}(v_i-\mu)^2\right)^{1/2} \tag{2}$$

It seems easier and more comprehensible to make statistical analysis by converting the sea current velocity (v) data prepared in time-series format into a probability distribution format. In this way, the sea current velocity probability distributions can be used as the primary tools for marine current energy analyses. For each velocity class, the probability density is defined as;

$$f(v_i) = f_i \,/ \sum_{i=1}^{n} f_i \tag{3}$$

Here, N indicates the time during the defined period, and repeatability of the same magnitude sea current velocity or frequency is symbolized by f_i.

If a random variable is discrete, the mean or expected value and variance of this variable with probability distribution $f(v)$ are respectively calculated as follows:

$$\mu = E(V) = \sum_{v} v f(v) \tag{4}$$

$$\sigma^2 = E[(V-\mu)^2] = \sum_{v}(v-\mu)^2 f(v) \tag{5}$$

Several methods can be used to get the distribution of sea current velocity frequency to generate an adequate statistical model that can predict marine current power capacity. Weibull distribution and Rayleigh distribution are among the most used methods in the literature.

2.2. Weibull Distribution

Weibull distribution can be used as a way of defining sea current velocity density. The Weibull probability distribution is defined as [32,33];

$$f_W(v) = \left(\frac{k}{c}\right)\left(\frac{v}{c}\right)^{k-1} exp\left[-\left(\frac{v}{c}\right)^{k}\right] \tag{6}$$

The cumulative Weibull probability distribution is expressed as;

$$F_W(v) = 1 - exp\left[-\left(\frac{v}{c}\right)^{k}\right] \tag{7}$$

where v is the sea current velocity. The c and k parameters are called scale and shape coefficients, and they are obtained from the sea current velocity data arranged in time-series format. The shape factor is calculated as:

$$k = \left(\frac{\sigma}{v_m}\right)^{-1.086} \quad (1 \leq \mathrm{k} \leq 10) \tag{8}$$

Later, the scale parameter equation is given as follows:

$$c = \left(\frac{v_m}{\Gamma(1+\frac{1}{k})}\right) \tag{9}$$

2.3. Rayleigh Distribution

A special case of the Weibull model is called the Rayleigh function. Assuming that the shape factor c of the Weibull function is equal to 2, the Rayleigh function is obtained. The Rayleigh probability density function and the cumulative density function can be calculated as follows:

$$f_R(v) = \frac{\pi v}{2\mu^2} exp\left[-\left(\frac{\pi}{4}\right)\left(\frac{v}{\mu}\right)^2\right] \tag{10}$$

$$F_R(v) = 1 - exp\left[-\left(\frac{\pi}{4}\right)\left(\frac{v}{\mu}\right)^2\right] \tag{11}$$

2.4. Power Potential of Sea Current Velocity

The power of the sea current that flows at velocity v through a turbine-swept area A increases as the cube of its velocity, and it is calculated as follows [34,35]:

$$P(v) = \frac{1}{2}\rho A v^3 \tag{12}$$

On the other hand, the current power density of the turbine per unit area considered based on any probability density function can be calculated as follows:

$$P(v) = \sum_{v} \frac{1}{2}\rho v^3 f(v) \tag{13}$$

3. Results and Discussion

3.1. Study Areas

The country is located at the crossroads of the three continents that make up the old world: Europe, Asia, and Africa. The Turkish peninsula is bathed by four seas: the Black Sea to the north, the Sea of Marmara to the northwest, the Aegean to the west, and, the Mediterranean to the south. The Sea of Marmara between the Asian and European land masses includes the Bosphorus and Dardanelles Straits. The entire coastline is over 8,000 kilometers long.

As presented in Figure 1, sea currents velocities and directions were measured by the buoy for 3 stations in Turkish seas by the Turkish State Meteorological Service. Information about the device feature is given in Table 1 and for measurement stations in Table 2. The current measurements, which yield a time series of hourly sea current velocities and directions, were performed with an ensemble interval of 1 hour. The measurements obtained from 5 and 35 m depths below the sea surface level were carried out from May 1, 2019, to September 30, 2019, covering 5 months period The sea water data consists of hourly sea current velocities and their corresponding current directions. The variations of hourly measured sea current velocity values for two depths over 5 months are shown in Figure 2.

Table 1. Information about device feature

Measuring station and device feature	Information and properties
Measuring instrument	ODAS04TR(MAS)
Height	4.51 m
Tower type	1.80 m
Power supply	Solar energy
Connection	GSM / GPRS

Table 2. Information about measurement stations

Station Names	Station numbers	Station areas	Station latitude	Station longitude
Antalya (Antalya gulf)	1	Mediterranean Sea	36°43'00" N	31°01'00" E
Silivri	2	Marmara Sea	41°04'23" N	28°14'22" E
Istanbul (Istanbul strait black sea exit)	3	Black sea	40°55'58" N	28°56'56" E

3.2. Current Flow Direction Structure of the Sea

It is very important to find out the prevailing current sea directions and velocities so that the optimal position of the current turbine can be determined in future studies. Figure 4 summarizes the current sea characteristics for a specific time at three stations, at 5 m and 35 m depth. Throughout the five months for Silivri and Antalya, with approximately similar tendencies observed for both locations, the dominant current flow directions level is mainly towards the 270° at 5 m depths, and the prevailing current sea is a primarily 240° direction at 35 m sea surface below. The most common dominant current directions are 90° to 150°, approximately 42% of the time and the least common current directions are 210° to 240° at both depths in Istanbul.

Figure 1. Study areas, location of the measurement stations, and map of the region

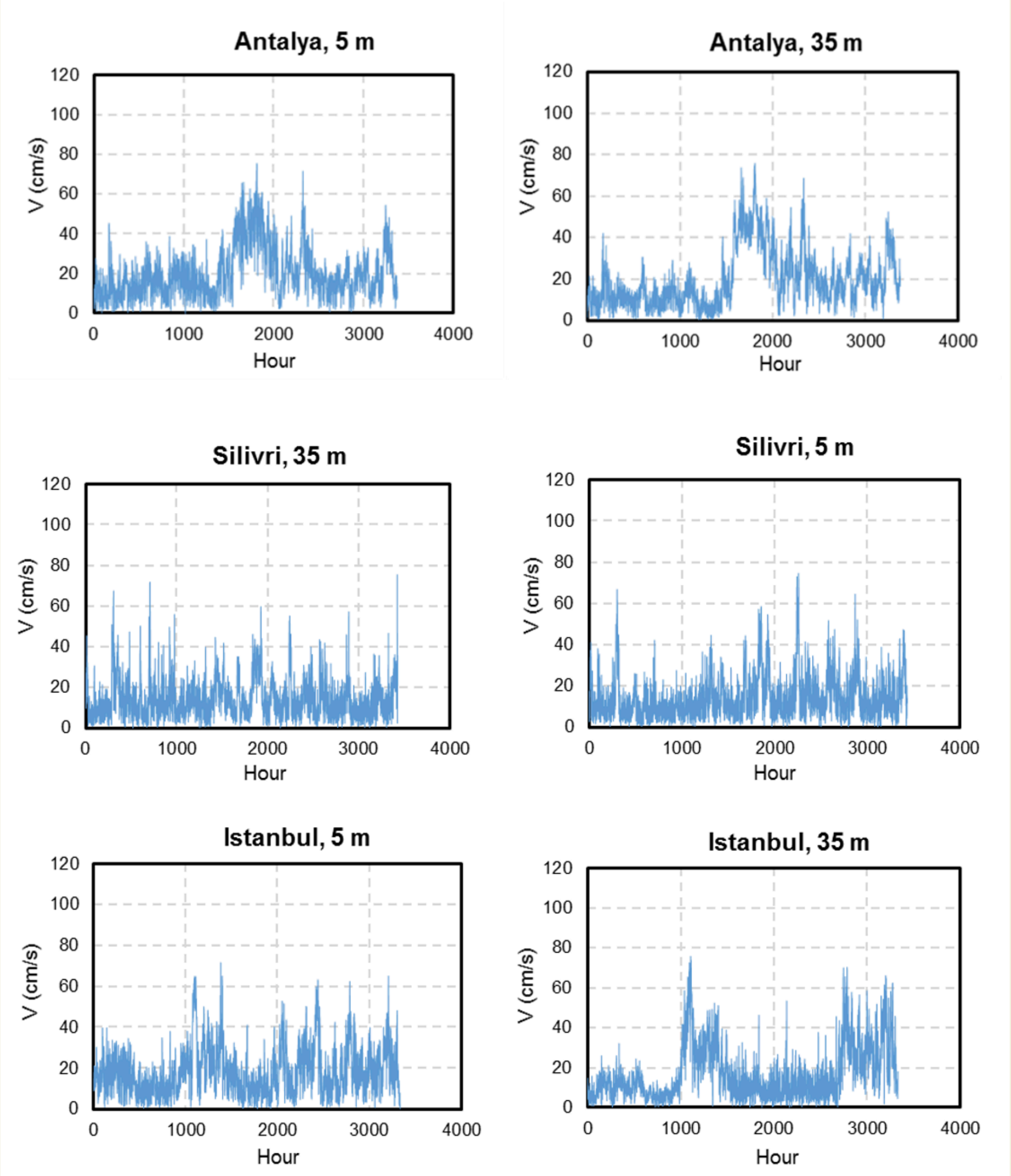

Figure 2. Hourly sea current velocity values of stations at 5 and 35 m below the sea surface level throughout five months

A complete assessment of the potential for hydrokinetic energy in areas of interest benefits from the evaluation of the changes in current velocity. According to the measurement results, the mean sea current speed is given in Figure 4a. As can be seen from the Figure, the mean sea current speeds of stations varied between 14.28 cm/s and 20.18 cm/s at 5 and 35 m below the sea surface level. The lowest value of the mean current speed is 14.28 cm/s at Silivri station at 5 m depth, while the highest value is 20.18 cm/s at Antalya station, at 5 m below the sea surface level. It is another significant point that Antalya presents a higher value of sea current speed than the other stations. There is currently no turbine installation for electricity generation in these stations. It is important to emphasize that these sea current velocities are ideal for the use of sea current energy conversion systems.

In Figure 4b, the average sea current power density values of Antalya, Silivri, and Istanbul stations are 10.42, 4.92, and 7.91 W/m2 calculated at depths of 5 m below the sea surface level, respectively. Besides, average sea current power density values are seen to be arranged with 11.44, 4.08, and 9.06 W/m2 in Antalya, Silivri, and Istanbul stations at 35 m depths below the sea surface level, respectively. Especially, Antalya is the most promising and convenient site to produce electricity from sea current power.

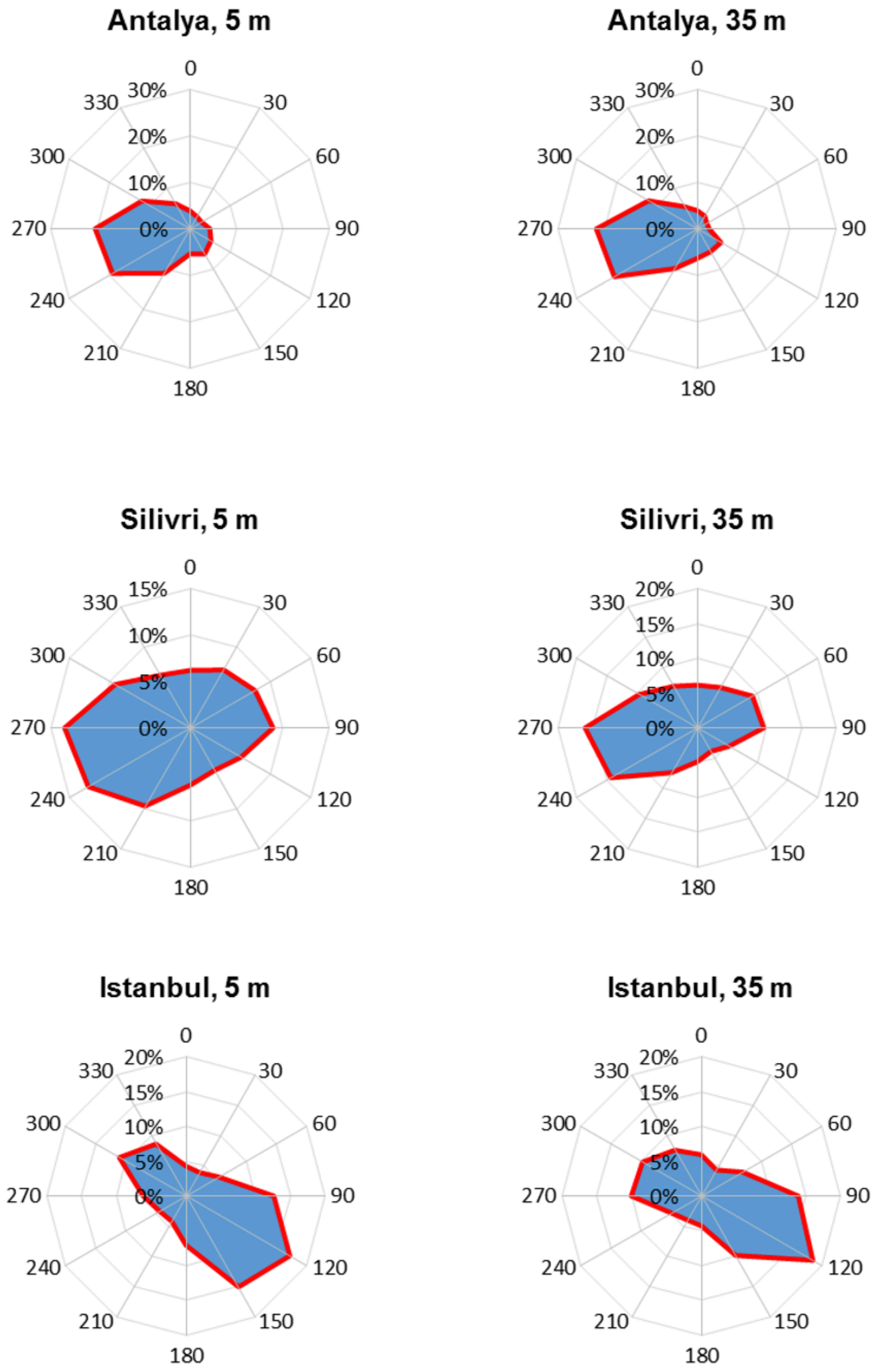

Figure 3. Sea current direction frequency distributions of stations at 5 and 35 m below the sea surface level

It is clear from Figure 4c that at Antalya, Silivri, and Istanbul stations, the dominant sea current flow direction was obtained as 270, 240, and 120° at 5 m depths below the sea surface level, respectively. Besides, the dominant sea current flow direction is seen to be closely arranged with 270, 240, and 120° in Antalya, Silivri, and Istanbul stations at 35 m depths below the sea surface level, respectively. Dominant and average sea current flow directions are mostly similar at all stations for both depths. Istanbul station's dominant current flow direction is 120° for both depths.

3.3. Statistical Modelling of Sea Current Velocity

The frequency distribution and probability density of the sea current speeds help in answering the following questions: (1) how long a sea current power plant is out of production in the case of lack of sea current; (2) what the range of the most frequent sea current speeds is; and (3) how often the sea current power plant achieves its rated output. In this part of the study, the probability densities and statistical analysis of the measured sea current velocities at three stations in the Turkey Seas are presented and discussed.

Table 3. The correlation coefficient (R) values for theoretical distribution models as an accuracy criterion

City	Depth (m)	Weibull model	Rayleigh model
Antalya	5	0.9790	0.9742
	35	0.9791	0.9295
Silivri	5	0.9940	0.9589
	35	0.9955	0.9781
Istanbul	5	0.9973	0.9782
	35	0.9892	0.9963

To do so, first, the measured probability distribution density of the sea current velocities for all stations and depths are presented. Then, sea current velocity frequency distributions for all stations and depths were obtained by using the Weibull and Rayleigh probability density functions. To choose the best theoretical probability density model, the theoretical and measured probability distributions

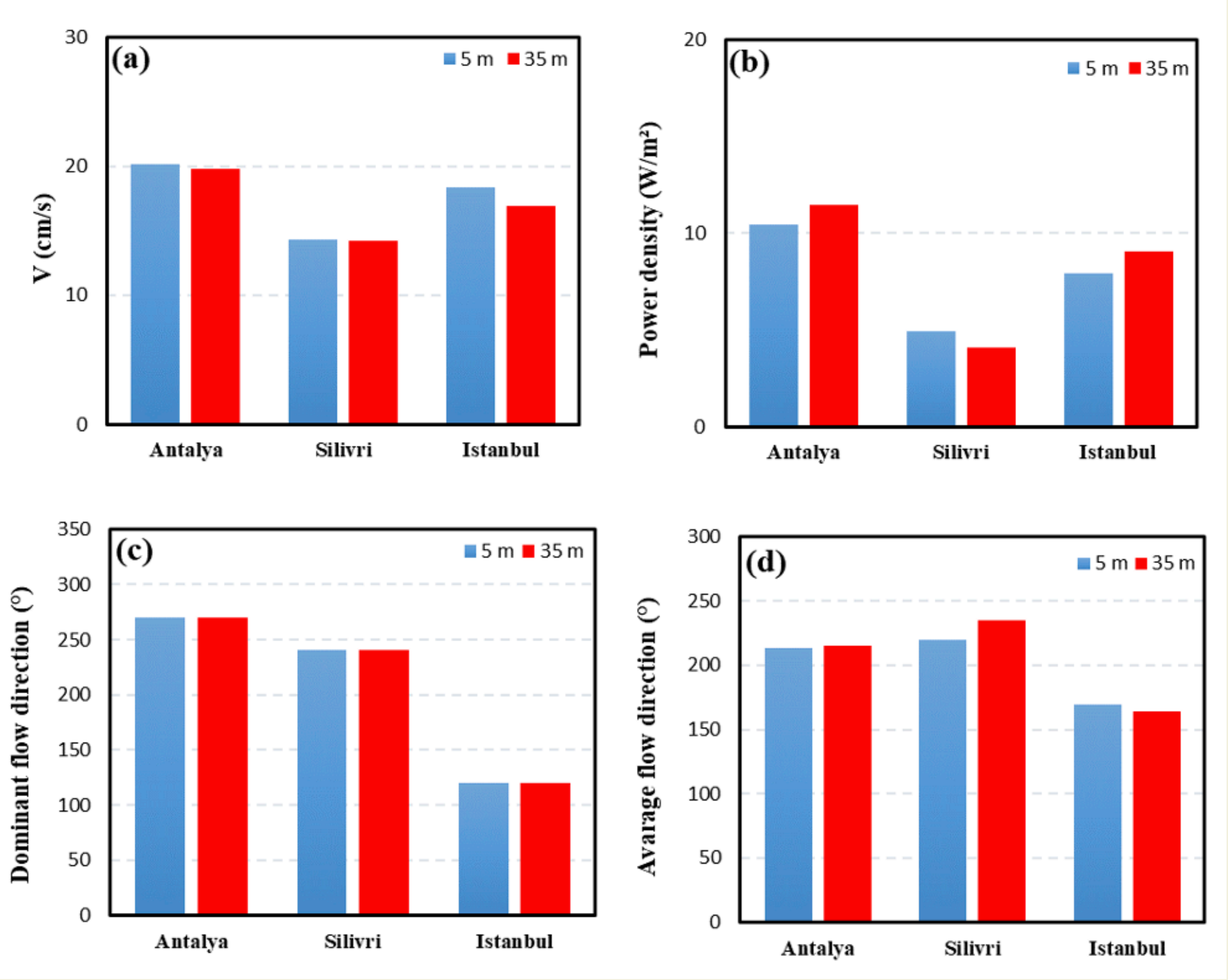

Figure 4. Sea current characteristics of stations a) Average mean velocity b) Power density c) Dominant flow direction (°) d) Average flow direction (°)

were compared, and the closeness and accuracy measures of the comparison were assessed in Table 3. The results showed that the Weibull probability function model provided better results than the Rayleigh probability density functions. Furthermore, the best performance was obtained from the 5 m depth below the sea surface level with a value of 0.9973 R at İstanbul station.

To perform both Weibull and Rayleigh we required shape and scale parameters (k and c). The shape parameter value decides the type of distribution whether it should be Weibull or Rayleigh. In this study, Figure 5 shows the comparison between sea current speed frequency distribution for Weibull or Rayleigh models and the measured distribution. In addition, Figure 5 revealed that histogram of the actual frequency distribution for five months with the Weibull and Rayleigh function for fitting a sea

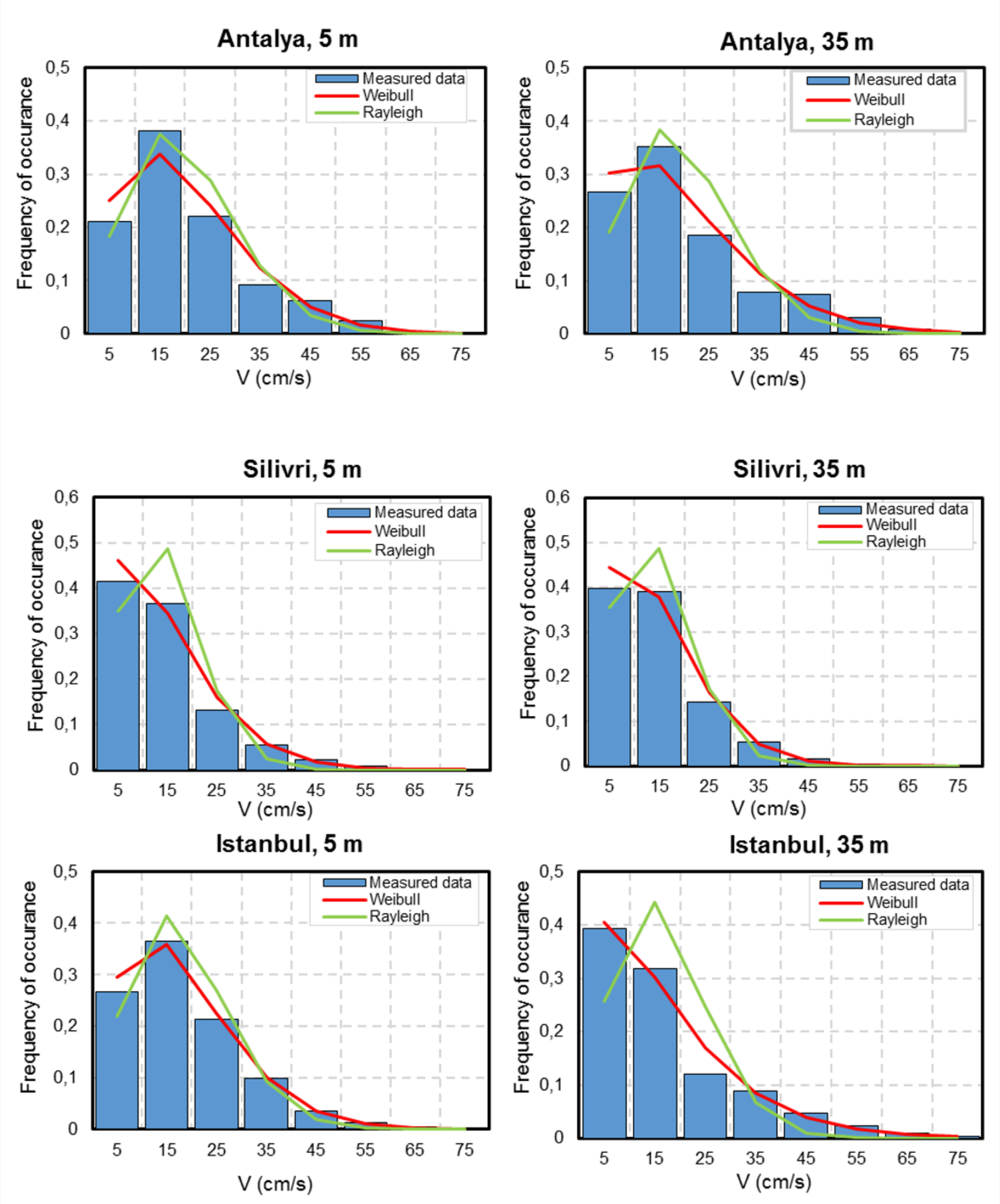

Figure 5. Comparison of observed and predicted sea current speed frequencies of all stations at 5 and 35 m below the sea surface level

current data probability distribution. As shown in the figure, in contrast to the Rayleigh distribution, the Weibull distribution perfectly fits the time series data.

The regression plots of actual and Weibull model (theoretical) values for probability density data of the sea current velocities are shown in Figure 6. The coefficient of determination, R2, indicates how much variance occurs between actual and theoretical values, which can be derived using a linear regression analysis method. It can provide a measure of the discrepancy between them. It is apparent from Figure 6 that Silivri presents a higher val-

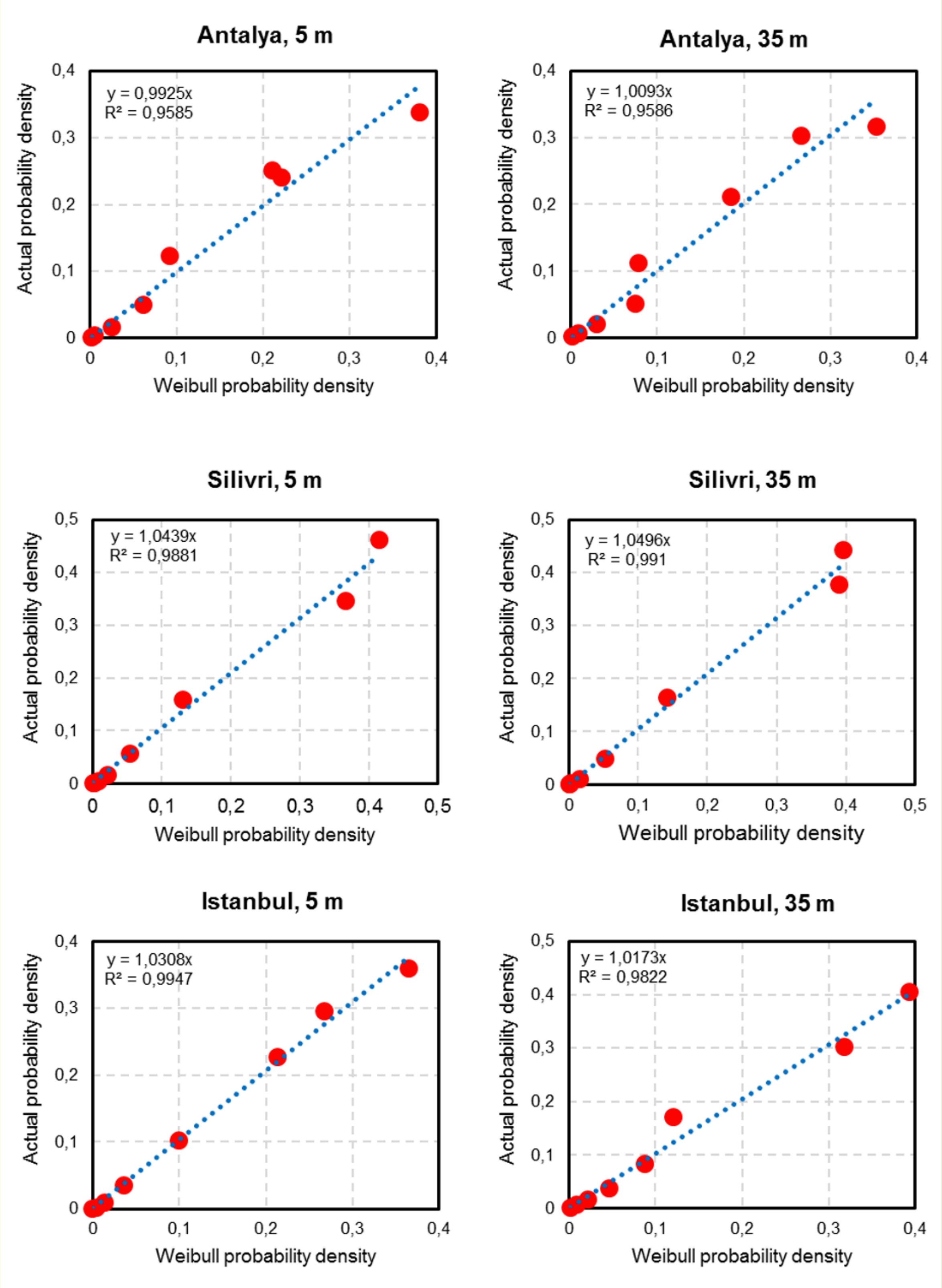

Figure 6. Relation between the Weibull probability density and the actual probability density for sea current velocities of all stations at 5 and 35 m below the sea surface level

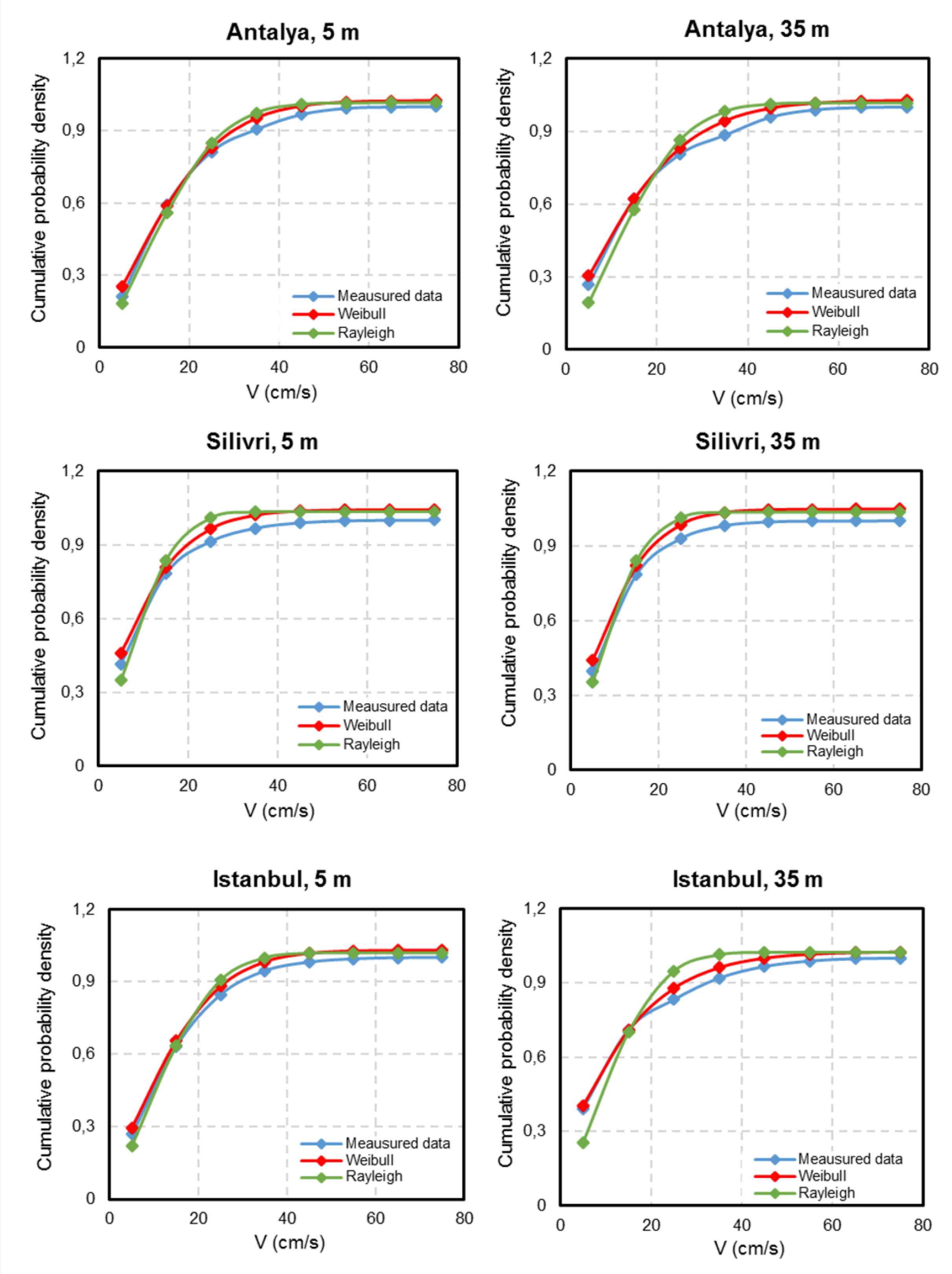

Figure 7. Cumulative probability distributions of sea current velocities for all stations at 5 and 35 m below the sea surface level

ue of R2 than the other stations. For example, the lowest value of R2 such as 95.85 occurs at Antalya station at 5 m depth, while on the other hand, a high level of R2 such as 99.47 occurs at Istanbul station at 5 m depth below the sea surface level.

In addition to the Weibull probability distribution model, the measured probability density values were compared with another probability function, that is, the Rayleigh distribution. For this aim, the measured and theoretical cumulative distribution functions of the velocity for all stations and depths were determined. The cumulative probability distributions of sea current velocities for all theoretical models are presented in Figure 7. Based on the results obtained here, the Weibull distribution model fitted the best to actual sea current velocity in the selected stations. In this regard, the probability density and cumulative probability density analysis for the Weibull model were carried out.

Mean sea current velocity and standard deviation of sea current velocity in Antalya, Silivri, and Istanbul stations were determined for all depths from measured data. The measured period, mean sea current velocity, and standard deviations for all stations and depths are presented in Table 4. According to this Table, Weibull probability distribution, very good results have been obtained. There is a significant difference in the mean sea current velocity among stations at different heights. The highest value of the mean sea current speed is 2.021 m/s at Antalya station at 5 m depth, while the lowest value is 0.981 m/s at Silivri station at 35 m depth below the sea surface level. It is apparent from the table that the sea current velocity of Antalya and Istanbul have a similar value during measurement times.

Table 4. The mean or expected value and standard deviation of the sea current velocities for all stations at different heights

Parameter	City	Depth (m)	Measured data	Weibull model	Rayleigh model
μ (m/s)	Antalya	5	2.021	2.021	2.019
		35	1.982	1.972	1.973
	Silivri	5	1.436	1.446	1.428
		35	1.416	1.432	1.418
	Istanbul	5	1.832	1.839	1.834
		35	1.691	1.697	1.692
σ (m/s)	Antalya	5	1.360	1.276	1.085
		35	1.417	1.375	1.488
	Silivri	5	1.078	1.040	0.788
		35	0.981	0.964	0.783
	Istanbul	5	1.199	1.182	0.991
		35	1.382	1.321	0.920

Table 5. The sea current power potential values for all stations at different heights

Station	Depth (m)	Measured data	Weibull model	Rayleigh model
Antalya	5	10.42	9.63	7.85
	35	11.44	10.43	7.34
Silivri	5	4.92	4.33	2.78
	35	4.08	3.71	2.72
Istanbul	5	7.91	7.41	5.89
	35	9.06	8.17	4.63

The last part of this study is a detailed assessment of sea current power potential values for all stations at different depths as given in Table 5. It is seen from the table that the Weibull model provides better power density estimations than the Rayleigh model for all stations and depths. The highest mean sea current power values of 5 m and 35 m are determined as 10.42 and 11.44 W/m^2, respectively at Antalya station. The lowest mean sea current power value is found to be 4.08 W/m^2 at Silivri station.

4. Conclusion

Turkey is heavily relying on imported fuels, and it is confronted with worldwide challenges such as increasing fuel prices, climate change, the threat of supply disruptions, and depleting indigenous energy resources. Turkey's energy demand is expected to rise by 4–6 percent per year until 2023, so Turkey intends to increase RES energy capacity to 30% by 2023. Among the RES, the untapped potential for energy supply from the seas, which currently seems to be difficult to estimate, seems to be quite promising as well. This is all the more ironic given the fact that a considerable portion of the Turkish population lives near the coastal areas since, except for a handful of studies, there has been almost no in-depth survey on the utility of sea energy and its conversion into electricity. The sea renewable energy potential for the Turkish seas seems to stand out.

The objective of the present study was to quantify the sea current potential in the seas of Turkey at 5 and 35 m depths below the sea surface level by using the Weibull and Rayleigh probability density functions. We can argue that the Weibull model provides better power density predictions than the Rayleigh model for all stations. In addition, our research has demonstrated that statistical models previously used in wind energy can be applied to the assessment of sea currents. Because many potential sites lack reliable, continuous data on current speed and conditions, the use of these statistical models has important practical consequences for the future development of sea current energy. As a result, statistical models capable of assessing potential power generation from ocean currents will be especially useful in the development of sea renewable energy.

Furthermore, in this study, we were also able to determine several fundamental properties such as sea current continuity, availability, behavior, and probability at three stations for both depths. We believe that our findings in this sense can pave the way to estimate the optimum position and power of the turbines to be implemented in the future.

The average sea current power density values of Antalya, Silivri, and Istanbul stations are 10.41, 4.92, and 7.91 W/m^2 calculated at depths of 5 m below the sea surface level, respectively. Besides, average sea current power density values are seen to be closely arranged with 11.44, 4.08, and 9.06 W/m^2 in Antalya, Silivri, and Istanbul stations at 35 m depths below the sea surface level, respectively. Average sea current power density values differ between stations. The highest value was calculated at the Antalya measurement station, and the lowest value was calculated at the Silivri station. Antalya is the most promising and convenient site at both depths to produce electricity from sea current power.

This is a feasibility study for determining sea current before investing in sea current energy for one region. Besides, the present study is a pre-research conducted for estimating the sea current energy analysis of selected regions. This work is expected to make a significant contribution to possible future sea current energy projects in Turkey.

5. Acknowledgments

The authors wish to thank the Turkish State Meteorological Service for supplying data.

6. References

[1] Yıldızhan, Ş., Çalık, A., Özcanlı, M., Serin, H., (2018). Bio-composite materials: a short review of recent trends, mechanical and chemical properties, and applications. European Mechanical Science. 2(3): 83–91. doi: 10.26701/ems.369005.

[2] Mbungu, N.T., Naidoo, R.M., Bansal, R.C., Siti, M.W., Tungadio, D.H., (2020). An overview of renewable energy resources and grid integration for commercial building applications. Journal of Energy Storage. 29(December 2019): 101385. doi: 10.1016/j.est.2020.101385.

[3] Moriarty, P., Honnery, D., (2018). Global renewable energy resources and use in 2050. Managing Global Warming: An Interface of Technology and Human Issues. (November): 221–35. doi: 10.1016/B978-0-12-814104-5.00006-5.

[4] Gielen, D., Boshell, F., Saygin, D., Bazilian, M.D., Wagner, N., Gorini, R., (2019). The role of renewable energy in the global energy transformation. Energy Strategy Reviews. 24(January): 38–50. doi: 10.1016/j.esr.2019.01.006.

[5] Minesto., (2020). Ocean energy. https://minesto.com/about-us. [accessed December 12, 2020].

[6] Kabir, A., Lemongo-Tchamba, I., Fernandez, A., (2015). An assessment of available ocean current hydrokinetic energy near the North Carolina shore. Renewable Energy. 80: 301–7. doi: 10.1016/j.renene.2015.02.011.

[7] Bento, P.M.R., Pombo, J.A.N., Mendes, R.P.G., Calado, M.R.A., Mariano, S.J.P.S., (2021). Ocean wave energy forecasting using optimized deep learning neural networks. Ocean Engineering. 219(December 2019): 108372. doi: 10.1016/j.oceaneng.2020.108372.

[8] Cenedese, C., n.d. Ocean current. https://www.britannica.com/science/ocean-current#ref301646. [accessed February 26, 2021].

[9] Hays, G.C., (2017). Ocean currents and marine life. Current Biology. 27(11): R470–3. doi: 10.1016/j.cub.2017.01.044.

[10] Neelamani, S., Al-Osairi, Y., (2019). Probability distribution, statistical characteristics, and power potential of seawater velocity around boubyan island in Kuwait. Journal of Engineering Research (Kuwait). 7(2): 143–66.

[11] Canepa, E., Pensieri, S., Bozzano, R., Faimali, M., Traverso, P., Cavaleri, L., (2015). The ODAS Italia 1 buoy: More than forty years of activity in the Ligurian Sea. Progress in Oceanography. 135(January 2019): 48–63. doi: 10.1016/j.pocean.2015.04.005.

[12] Chiri, H., Abascal, A.J., Castanedo, S., Antolínez, J.A.A., Liu, Y., Weisberg, R.H., et al., (2019). Statistical simulation of ocean current patterns using autoregressive logistic regression models: A case study in the Gulf of Mexico. Ocean Modelling. 136(January): 1–12. doi: 10.1016/j.ocemod.2019.02.010.

[13] Mandal, S., Sil, S., Gangopadhyay, A., Murty, T., Swain, D., (2018). On extracting high-frequency tidal variability from HF radar data in the northwestern Bay of Bengal. Journal of Operational Oceanography. 11(2): 65–81. doi: 10.1080/1755876X.2018.1479571.

[14] Shay, L.K., C.Graber, H., B.Ross, D., Rickey, D.C., (1995). Mesoscale Ocean Surface Current Structure Detected by High-Frequency Radar. Journal of Atmospheric and Oceanic Technology. 12(4): 881–900. doi: https://doi.org/10.1175/1520-0426(1995)012<0881:MOSCSD>2.0.CO;2.

[15] Paduan, J.D., Rosenfeld, L.K., (1996). Remotely sensed surface currents in Monterey Bay from shore-based HF radar (Coastal Ocean Dynamics Application Radar). Journal of Geophysical Research C: Oceans. 101(C9): 20669–86. doi: 10.1029/96JC01663.

[16] Ullman, D.S., Codiga, D.L., (2004). Seasonal variation of a coastal jet in the Long Island Sound outflow region based on HF radar and Doppler current observations. Journal of Geophysical Research C: Oceans. 109(7): 1–15. doi: 10.1029/2002JC001660.

[17] Ramp, S.R., Barrick, D.E., Ito, T., Cook, M.S., (2008). Variability of the Kuroshio current south Sagami Bay as observed using long-range coastal HF radars. Journal of Geophysical Research: Oceans. 113(6): 1–15. doi: 10.1029/2007JC004132.

[18] Gough, M.K., Garfield, N., Shaw, E.M., (2010). An analysis of HF radar measured surface currents to determine tidally, wind - forced , and seasonal circulation in the Gulf of the Farallones , California , United States 115: 1–19. doi: 10.1029/2009JC005644.

[19] Roarty, H., Glenn, S., Kohut, J., Gong, D., Handel, E., Rivera, E., et al., (2010). Operation and application of a regional high-frequency radar network in the Mid-Atlantic Bight. Marine Technology Society Journal. 44(6): 133–45. doi: 10.4031/MTSJ.44.6.5.

[20] Shay, L.K., Martinez-Pedraja, J., Cook, T.M., Haus, B.K., Weisberg, R.H., (2007). High-frequency radar mapping of surface

currents using WERA. Journal of Atmospheric and Oceanic Technology. 24(3): 484–503. doi: 10.1175/JTECH1985.1.

[21] Freilich, M.H., Dunbar, R.S., (1999). The accuracy of the NSCAT 1 vector winds: Comparisons with National Data Buoy Center buoys. Journal of Geophysical Research: Oceans. 104(C5): 11231–46. doi: 10.1029/1998jc900091.

[22] Mears, C.A., Smith, D.K., Wentz, F.J., (2001). Comparison of Special Sensor Microwave Imager and buoy-measured wind speeds from 1987 to 1997. Journal of Geophysical Research: Oceans. 106(C6): 11719–29. doi: 10.1029/1999jc000097.

[23] Le Traon, P.Y., (2013). From satellite altimetry to Argo and operational oceanography: Three revolutions in oceanography. Ocean Science. 9(5): 901–15. doi: 10.5194/os-9-901-2013.

[24] Wagner, V., Hageberg, A.A., Michelsen, C., (2003). EGOS-European Group on Ocean Stations providing real time buoy observations from data sparse areas of the North Atlantic Ocean and adjacent seas. Elsevier Oceanography Series. 69(C): 340–4. doi: 10.1016/S0422-9894(03)80054-5.

[25] Petersen, G.N., (2017). Meteorological buoy measurements in the Iceland Sea, 2007-2009. Earth System Science Data. 9(2): 779–89. doi: 10.5194/essd-9-779-2017.

[26] Oliveira, L.R., Piola, A.R., Mata, M.M., Soares, I.D., (2009). Brazil Current surface circulation and energetics observed from drifting buoys. Journal of Geophysical Research: Oceans. 114(10): 1–12. doi: 10.1029/2008JC004900.

[27] Albani, A., Ibrahim, M.Z., (2020). The Probability Density Distribution for Ocean Current Speed at Selected Sites THE PROBABILITY DENSITY DISTRIBUTION FOR OCEAN CURRENT SPEED AT SELECTED SITES IN (October). doi: 10.31838/jcr.07.19.607.

[28] Chu, P.C., (2008). Weibull distribution for the global surface current speeds obtained from satellite altimetry. International Geoscience and Remote Sensing Symposium (IGARSS). 3(1): 11–5. doi: 10.1109/IGARSS.2008.4779282.

[29] Chu, P.C., (2008). Probability distribution function of the upper equatorial Pacific current speeds. Geophysical Research Letters. 35(12). doi: 10.1029/2008GL033669.

[30] Kim, D.K., Wong, E.W.C., Lee, E.B., Yu, S.Y., Kim, Y.T., (2019). A method for the empirical formulation of current profile. Ships and Offshore Structures. 14(2): 176–92. doi: 10.1080/17445302.2018.1488340.

[31] Ashkenazy, Y., Gildor, H., (2011). On the probability and spatial distribution of ocean surface currents. Journal of Physical Oceanography. 41(12): 2295–306. doi: 10.1175/JPO-D-11-04.1.

[32] Bilgili, M., Sahin, B., (2009). Investigation of Wind Energy Density in the Southern and Southwestern Region of Turkey. Journal of Energy Engineering. 135(1): 12–20. doi: 10.1061/(asce)0733-9402(2009)135:1(12).

[33] Kaplan, Y.A., (2017). Determination of Weibull parameters by different numerical methods and analysis of wind power density in Osmaniye, Turkey. Scientia Iranica. 24(6): 3204–12. doi: 10.24200/sci.2017.4354.

[34] Akpinar, E.K., Akpinar, S., (2004). An Analysis of the Wind Energy Potential of Elazig, Turkey. International Journal of Green Energy. 1(2): 193–207. doi: 10.1081/ge-120038752.

[35] Kaplan, Y.A., (2020). Determination of Weibull parameters using the standard deviation method and performance comparison at different locations. Scientia Iranica. 27(6 D): 3075–83. doi: 10.24200/SCI.2019.50323.1632.